Experimental Microporomechanics

Franz-Josef Ulm,* Antoine Delafargue, Georgios Constantinides
Massachusetts Institute of Technology, Cambridge MA, U.S.A.

Abstract Is it possible to break down natural porous material systems down to a scale where materials no longer change from one material to another, and upscale ('nanoengineer') the behavior from the nanoscale to the macroscale of engineering applications? – This is the challenging question we address in these lecture notes through a review of tools and methods of experimental microporomechanics. The combination of advanced experimental indentation techniques and microporomechanics theory provides a unique opportunity to understand and assess nanoproperties and microstructure, as a new basis for the engineering prediction of macroscopic poromechanical properties of natural composites. This is illustrated for cement-based materials and shales.

1 Introduction

Inarguably, natural composite materials (concrete, soils, rocks, bones, etc.) are multiphase and multiscale material systems. The multiphase composition of such materials is permanently evolving over various scales of time and length, creating in the course of this process the most heterogeneous classes of materials in existence, with heterogeneities that manifest themselves from the nanoscale to the macroscale. The most prominent heterogeneity of such natural composite materials is the porosity which is the space left in between the different solid phases at various scales, ranging from interlayer spaces in between minerals filled by a few water molecules, to the macropore space in between microstructural units of the material in the micrometer to millimeter range; and which are all detrimental to the mechanical behavior of natural composite materials.

Recent advances in both experimental and theoretical microporomechanics provides a rational means to quantitatively address multiphase and multiscale material systems. The underlying idea of continuum micro(poro)mechanics is that it is possible to separate a heterogeneous material into phases with on-average constant material properties (Suquet, 1997; Zaoui, 2002). A phase, in the sense of continuum micromechanics, is not necessarily a material phase such as a specific mineral as used in physical chemistry, but

*In Collaboration with Prof. Y. Abousleiman (Oklahoma University at Norman); Dr. Paul Acker and Jean-Francois Batoz (Lafarge Corp.), Drs. R. Ewy, L. Duranti, D. K. McCarty (Chevron Texaco); and the support of Nanolab@MIT team, A. Schwartzman and Prof. K. Van Vliet. Financial support by the Lafarge Corporation and Chevron Texaco is gratefully acknowledged.

a material domain that can be identified, at a given scale, with on-average constant material properties, so that a continuum mechanics analysis can be performed, with some confidence and accuracy, at the considered material scale. Such phases are referred to as microhomogeneous phases. Provided the existence of such microhomogeneous phases, a combination of novel nanomechanical testing of materials and upscaling methods is a powerful tool to 'break the code' of natural composites: identify material invariant properties and explain, by upscaling, the macroscopic diversity of natural composite materials systems.

The first part of these lecture notes provides an introduction to theory of instrumented indentation, and the application to heterogeneous material systems. By way of application, two case studies are presented in a second and third part, dealing with two natural material systems: cement-based materials and shales.

2 Nanoindentation

Indentation tests go a long way back, as early as 1722 (Réaumur, 1722), and started out with hardness measurements (for a review see Borodich and Keer (2004) and references cited herein). More recently, thanks to progress in hardware and software control, depth sensing techniques were introduced that allow a continuous monitoring of the displacement of the indenter into the specimen surface for both loading and unloading. The idea of depth sensing techniques and its implementation down to the nanoscale appears to have developed first in the former Soviet Union from the mid 1950ies on throughout the 1970ies, and received considerable attention world-wide, ever since Doerner and Nix (1986) and Oliver and Pharr (1992) in the late 1980ies and early 1990ies, also identified this technique for analysis and estimation of mechanical properties of materials. While the chronology of events of discovery may still be in debate[1], there is little doubt, at least as far as the elastic behavior is concerned, that it is the Hertz type contact problem that forms much of the theoretical background of modern indentation analysis. An indentation test provides a continuous record of the variation of the indentation load, P, as a function of the depth of indentation, h, into the indented specimen, and the extraction of material properties, from the $P-h$ curve, is achieved by inverse analysis.

2.1 Hardness

To motivate the forthcoming developments, we consider a three-dimensional, rigid, conical indenter of a given half-angle α, indenting normally into a homogeneous elastic perfectly plastic cohesive-frictional material half-space, $x_i \geq 0$. The origin (O) of the Cartesian system is put at the point of the initial contact between the conical indenter and the half-space (Fig. 1). The indentation test consists of (at least) two phases, a loading phase and an unloading phase, during which either the force, P, or the rigid displacement of the indenter, h, is prescribed. Conical indentation leads to geometrically self-similar indentation states. That is, for a given half-angle, the average pressure below

[1] The chronology of events of discovery of depth-sensing indentation and indentation anlaysis has only recently been revealed by Borodich in several remarkable publications (Borodich and Keer, 2004).

the indenter is independent of the indentation load and the true contact area. Using the projected current contact area, which is proportional to the true contact area for geometrically self-similar indenters (*ie.* $A_M = A/\sin\alpha$ for conical indenters), yields the classical definition of hardness H, which can be determined at any point along the $P-h$ curve for which the contact area is known:

$$H \stackrel{def}{=} \frac{P_1}{A_1} = \frac{P_2}{A_2} = ... = \frac{P}{A} \tag{2.1}$$

where $A = \pi a^2$ is the projected contact area, and $a = h_c \tan\alpha$ is the contact radius.

The main problem in the analysis is that the contact surface A (respectively the contact depth h_c) is not known *a priori*, but is a solution of a boundary value problem. In fact, the rigid displacement h of the indenter is generally not the contact depth, h_c (Fig. 1), corresponding to the maximum projected contact surface of the indenter with the deformed half-space surface: $h_c/h < 1$ corresponds to what is referred to, in the indentation literature, as sinking-in; and $h_c/h > 1$ as piling-up (Fig. 1). Hence, there are *a priori* two independent measurements to be carried out: the force P and the projected contact surface A. It is instructive to perform a dimensional analysis (Chen and Chen, 2004): The two dependent quantities of interest that define the hardness, force P and contact area A (respectively the contact depth h_c), depend on the material properties (stiffness C_{ijkl}, cohesion c, friction angle φ), the indenter geometry (which in the case of conical indentation reduces to the half-apex angle α), and the indentation depth h:

$$P = f(C_{ijkl}, c, \varphi, \alpha, h) \tag{2.2a}$$

$$A = g(C_{ijkl}, c, \varphi, \alpha, h) \tag{2.2b}$$

From a straightforward application of dimensional analysis (or more precisely the Pi-Theorem) to relations (2.2), it is readily found that the two dimensionless relations,

$$\frac{P}{ch^2} = \Pi_\alpha\left(\frac{C_{ijkl}}{c}, \varphi, \alpha\right) \tag{2.3a}$$

$$\frac{A}{h^2} = \Pi_\beta\left(\frac{C_{ijkl}}{c}, \varphi, \alpha\right) \tag{2.3b}$$

define a unique third dimensionless relation, the hardness-to-cohesion ratio as a unique function of the stiffness-to-cohesion ratio, the friction angle and the half-apex angle:

$$\frac{H}{c} = \frac{\Pi_\alpha}{\Pi_\beta} = \mathcal{H}\left(\frac{C_{ijkl}}{c}, \varphi, \alpha\right) \tag{2.4}$$

The dimensionless relations have two limits:

For conical indentation into a perfectly elastic material ($C_{ijkl}/c \to 0, \varphi = 0$), it is readily recognized that the dimensionless relation (2.3b) is independent of the elasticity constants, and that the contact depth to indentation depth ratio is a constant (Swadener and Pharr, 2001):

$$\lim_{C_{ijkl}/c \to 0} \frac{h_c}{h} = \frac{2}{\pi} \tag{2.5}$$

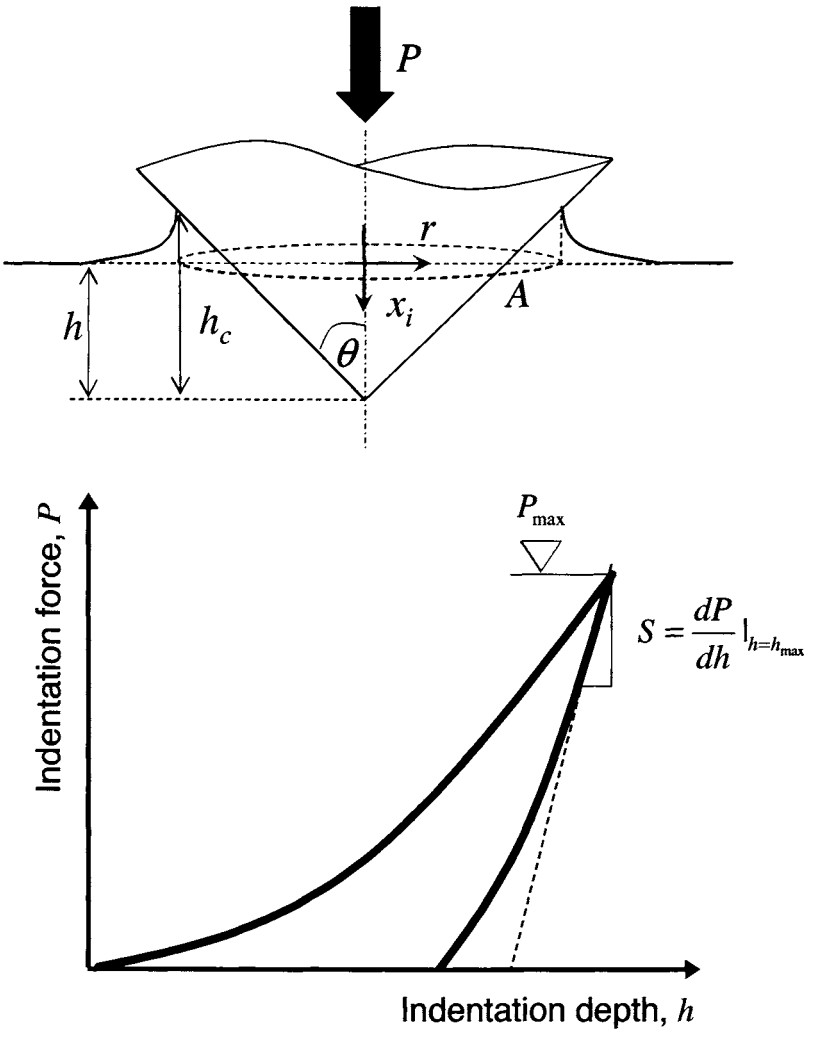

Figure 1. Principle of Indentation Test.

Relation (2.5), which is a general property of the Hertz contact problem into a perfectly elastic material (whether isotropic or anisotropic), states that perfect elasticity always produces sink-in, $h_c/h < 1$.

For conical indentation into a rigid plastic material ($c/C_{ijkl} \to 0$), yield design approaches are suitably employed to determine the H/c ratio for specific strength criteria. Yield design is based on the assumption, that plastic failure occurs when the material system has exhausted its capacity to store the externally supplied work rate, *ie.* $P\dot{h}$ into recoverable elastic energy, so that the supplied work rate is entirely dissipated within the material bulk and along surfaces of discontinuity through kinematically admissible velocity fields $\underline{U}$ (see e.g. Salençon (1983), Ulm and Coussy (2003) Chapter 9); *ie.* for the indentation test:

$$P\mathring{h} = \int_\Omega \pi(\mathbf{d})\, d\Omega + \int_\Gamma \pi([[\underline{U}]])\, d\Gamma \tag{2.6}$$

where $\pi(\mathbf{d}) = \sup \boldsymbol{\sigma} : \mathbf{d}$ and $\pi([[\underline{U}]]) = \sup \underline{T} \cdot [[\underline{U}]]$ is the maximum dissipation capacity the material can develop in the material bulk Ω and along surfaces of discontinuity Γ; $\boldsymbol{\sigma}$ is the statically and plastically admissible stress field, and $\underline{T} = \boldsymbol{\sigma} \cdot \underline{n}$ is the stress vector, satisfying:

$$\boldsymbol{\sigma} = {}^t\boldsymbol{\sigma};\ \operatorname{div} \boldsymbol{\sigma} = 0;\ [[\underline{T}]] = [[\boldsymbol{\sigma} \cdot \underline{n}]] = 0 \tag{2.7a}$$

$$f(\boldsymbol{\sigma}) \leq 0;\ f(\underline{T}) \leq 0 \tag{2.7b}$$

where superscript t stands for transpose; and $f(\boldsymbol{\sigma})$ and $f(\underline{T})$ are the yield function defining the strength domain of the material system respectively in continuous material sub-domains and on surfaces of discontinuity; while $\mathbf{d}$ is the solution strain rate field in continuous material sub-domains, and $[[\underline{U}]]$ is the velocity jump over surfaces of discontinuity Γ, which are kinematically compatible with the velocity field $\underline{U}$, and compatible with the plastic flow rule of the material:

$$\mathbf{d} = \frac{1}{2}\left(\operatorname{grad} \underline{U} + {}^t \operatorname{grad} \underline{U}\right) = \mathring{\lambda} \frac{\partial f}{\partial \boldsymbol{\sigma}} \tag{2.8a}$$

$$[[\underline{U}]] = \underline{U}^+ - \underline{U}^- = \mathring{\lambda} \frac{\partial f}{\partial \underline{T}} \tag{2.8b}$$

For a cohesive-frictional material of the Mohr-Coulomb type, the problem to be solved reads (Ganneau et al., 2004):

$$P\mathring{h} = \frac{c}{\tan\varphi} \int_{\partial\Omega} \underline{U} \cdot \underline{n} da \tag{2.9}$$

where $\underline{U} \cdot \underline{n}$ is the normal component of the velocity field at the surface $\partial\Omega$ of the half-space, which includes the cone mantel $A_M = A/\sin\alpha$, and the stress-free surface outside the contact radius $r \geq a = \sqrt{A/\pi}$. The previous relation can be recast in the form of (2.4):

$$\lim_{c/C_{ijkl} \to 0} \frac{H}{c} = \mathcal{H}(\varphi, \theta) = \frac{1}{A \tan\varphi} \int_{\partial\Omega} \overline{\underline{U}}' \cdot \underline{n} da \tag{2.10}$$

with $\overline{\underline{U}}' = \underline{U}'/\mathring{h}$ the normalized surface velocity field. Exact axi-symmetric yield design solutions for indentation in Mohr-Coulomb materials are scarce: Hopkins et al. (1961)

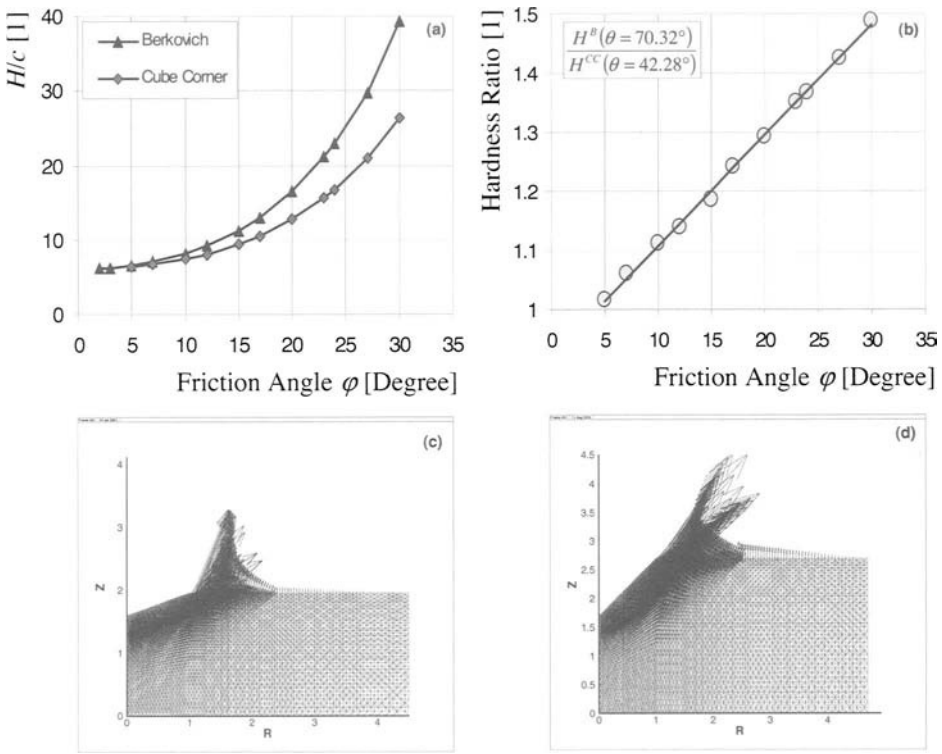

Figure 2. Upper-Bound Yield Design Approach (compiled from Ganneau et al., 2004): Hardness-Cohesion ratio as a function of friction angle for different semi-apex angles: $\alpha = 70.32°$ is representative of a Berkovich indenter; and $\alpha = 42.28°$ is representative of a Cube Corner indenter, when assimilating the three-sided pyramidal indenters to cones of same projected contact area.

provided a yield design solution for the smooth punch and Matar and Salençon (1982) provided a heuristic solution for the perfectly rough punch. Not surprisingly, as one reduces the cone angle, the amount of energy that is dissipated at plastic failure decreases (Figure 2). Making use of this property, it is possible to determine from two indentation tests with different apex angles the two strength properties of rigid-plastic cohesive frictionless materials. Figure 2 displays the hardness-to-cohesion ratio as a function of the friction angle for two apex angles ($\alpha = 70.32°$ and $\alpha = 42.28°$) obtained from a computational implementation of the upper bound limit theorem (Ganneau and Ulm, 2004; Ganneau et al., 2004). The figure also displays the hardness ratio vs. the friction angle, displaying an almost linear relation.

Finally, in between these two limit cases (purely elastic – rigid plastic), the con-

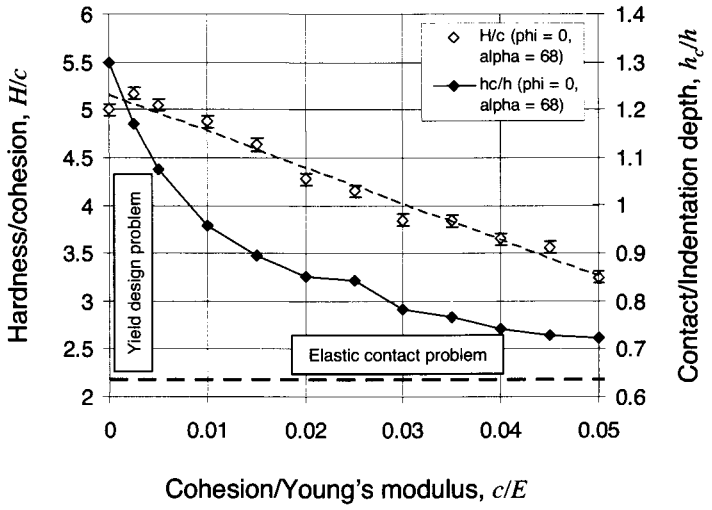

Figure 3. Hardness-to-cohesion ratio vs. strength-to-stiffness ratio for pure cohesive materials, $\varphi = 0$ (generated from Cheng and Cheng (1999)).

tact depth – to indentation depth ratio needs to be solved for any particular material behavior. Closed form solutions are generally not available, so that use of numerical methods to solve the nonlinear elastoplastic contact problem becomes necessary. For elastoplastic non-frictional materials ($\varphi = 0$) with and without strain hardening, Chen and Chen (1999,2004) showed, by means of finite element simulations, that h_c/h is insensitive to the Poisson's ratio, but dependent on the strength-to-stiffness ratio c/E and on the power-strain coefficient. For this class of materials, the dependence of h_c/h on the material properties translates into the dependence of the hardness-to-strength ratio on the strength-to-stiffness ratio (Figure 3). A similar dependence is expected to characterize cohesive-frictional materials, but to our knowledge, the dependence of h_c/h on the strength properties of frictional materials has not been studied.

For geomaterials, for which typically $c/E \sim 10^{-3} - 10^{-6}$ it is most likely that yield design solutions of the form $H/c = \mathcal{H}(\varphi, \alpha)$ are highly relevant. In return, it requires an independent measurement of the projected contact surface, in order to determine –with high accuracy– the exact value of the hardness, and hence the strength parameters, c and φ.

2.2 Indentation Stiffness Measurements

The quantity that is measured upon unloading is the slope S that is fitted to the $P-h$ curve at the maximum indentation depth $h_{\max}$ (Fig. 1), and the mechanical property that is extracted is the indentation modulus M, from the so-called Bulychev–Alekhin–

Shoroshorov equation, in short BASh-equation (see e.g. Borodich and Keer, 2004):

$$S = \frac{dP}{dh}|_{h_{\max}} \overset{def}{=} \frac{2}{\sqrt{\pi}} M\sqrt{A} \tag{2.11}$$

Again, it is instructive to perform a dimensional analysis. Provided a pure elastic behavior upon unloading, slope S depends on the elastic constants, as well as on the force $P_{\max}$, the maximum indentation depth $h_{\max}$, and the half-cone angle α. Dimensional analysis yields:

$$\frac{Sh_{\max}}{P_{\max}} = \Pi_\gamma \left(\frac{C_{ijkl} h_{\max}^2}{P_{\max}}, \alpha \right) \tag{2.12}$$

or equivalently, using definition (2.11) and the invariants (2.4) that characterize the loading indentation response right upon unloading:

$$\frac{S}{H\sqrt{A}} = \frac{2}{\sqrt{\pi}} \frac{M}{H} = \sqrt{\Pi_\beta} \times \Pi_\gamma \left(\frac{C_{ijkl}}{H} \Pi_\beta^{-1}, \alpha \right) \tag{2.13}$$

where H is the hardness during loading. The r.h.s. of (2.13) is readily found to be independent of indentation depth $h_{\max}$, at which unloading takes place; as is the M/H ratio, which depends on the stiffness-to-cohesion ratio, the friction angle and the half-apex angle. For instance, in the case of a perfect elastic behavior, the elastic Hertz contact solution yields:

$$\lim_{C_{ijkl}/c \to 0} \left(\frac{M}{H} \right) = 2 \tan \alpha \tag{2.14}$$

In this case, $\lim_{C_{ijkl}/c \to 0} \Pi_\beta = \frac{4}{\pi} \tan^2 \alpha$ and $\lim_{C_{ijkl}/c \to 0} \Pi_\gamma = 2$. In general, however, M/H is a dimensionless number that characterizes, for a given cone angle, the stiffness-to-strength ratio of the intended (homogeneous) material.

Similar to the extraction of strength properties from hardness measurements, the key to a successful determination of the elastic properties from indentation relies on the determination of the correct projected contact area. This is not an easy task. Traditionally, the contact area has been determined by direct optical measurement of the size of the residual hardness impression after a complete unloading. For practical reasons, however, some means other than direct observation of the hardness impressions is needed to measure contact areas, since imaging very small indentations is both time-consuming and difficult (Fig. 4). Making use of the BASh relation (2.11), the contact surface can be scaled, for a given material (same M), from two unloading slopes:

$$\frac{A}{A_1} = \left(\frac{S}{S_1} \right)^2 \tag{2.15}$$

For instance, if the contact area for a specific indentation depth or indentation geometry (half-apex angle α) is measured, it is possible to either determine the contact area or contact depth for another indentation depth for the same indenter (same α), or scale the contact area from one indenter geometry to another. In the latter case, use of (2.15) allows one to determine e.g. the hardness ratio from:

$$\frac{H}{H_1} = \frac{P}{P_1} \left(\frac{S}{S_1} \right)^{-2} \tag{2.16}$$

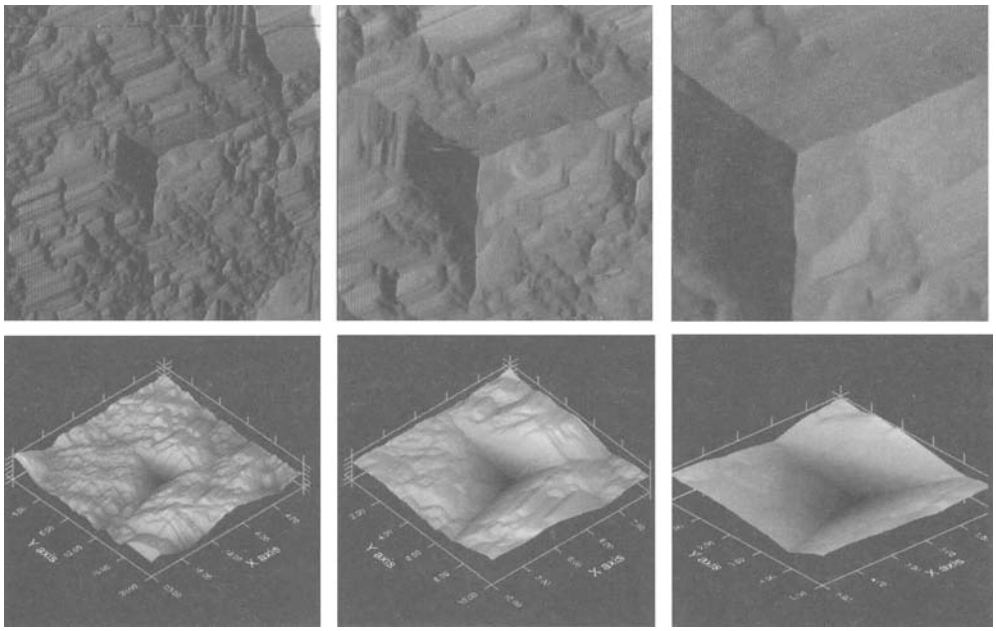

Figure 4. Gradient Images (Top) and AFM Images (Bottom) of residual impressions after microindentation in a shale material.

An original method for conical indentation that circumvents the necessity to measure the contact area, was suggested by Oliver and Pharr (1992), by applying relation (2.5) to the pure elastic recovery during unloading:

$$h_c - h_f = \frac{2}{\pi}\left(h_{\max} - h_f\right) \tag{2.17}$$

where h_f is the residual indentation depth. Since $h_{\max}$ is measured, the key to the analysis becomes the determination of the residual displacement h_f. This is achieved by considering that the elastic unloading is scaled, for conical indentation, by a power-two function:

$$P = c\left(h - h_f\right)^2;\ h - h_f = 2\frac{P}{S} \tag{2.18}$$

Finally, a combination of (2.17) and (2.18) yields:

$$\frac{h_c}{h_{\max}} = 1 - \epsilon\frac{P}{Sh_{\max}} \tag{2.19}$$

where $\epsilon = 2\left(1 - 2/\pi\right) = 0.73$. Relation (2.19) is also valid for other indenter shapes: $\epsilon = 1$ for a flat punch ($P \propto h$), and $\epsilon = 0.75$ for a parabola of revolution ($P \propto h^{3/2}$; Sneddon, 1977).

The main problem of the Oliver and Pharr method is that is assumes the shape of the deformed solid outside the area of contact to be elastic. This is not true when plastic deformations occur around the indenter to form pile-ups, $h_c/h > 1$, which cannot be predicted by (2.19). Several modifications have been proposed to the original method (Pharr, 2002; Chen and Chen, 2004, Oliver and Pharr, 2004), and the topic continues to be focus of intensive research in the indentation mechanics community.

2.3 Indenter Geometries

An essential feature of indentation analysis is the self-similarity of Hertz-type contact problems. The conditions under which frictionless Hertz type contact problems possess classical self-similarity were stated by Borodich (1988 according to Borodich et al., 2003); and include:

1. The shape of the indenter is described by a homogeneous function whose degree is greater or equal to unity. Using a Cartesian coordinate system $Ox_1x_2x_3$ whose origin O is at the indenter tip and x_3 is the orientation of the indentation, the shape of the indenter (height) is defined by:

$$f(\lambda x_1, \lambda x_2) = \lambda^d f(x_1, x_2) \tag{2.20}$$

for arbitrary positive λ. Here d is the degree of the homogenous function f; in particular $d = 1$ for a cone and $d = 2$ for the elliptic paraboloid considered by Hertz. Such axi-symmetric indenters can be described by monomial functions of the form (first introduced by Galin, 1946 according to Borodich and Keer, 2004):

$$f = f(x_1 = r\cos\theta, x_2 = r\sin\theta) = Br^d \tag{2.21}$$

where B is the shape function of the indenter at unit radius, and d is the degree of the homogeneous function. For a conical indenter ($d = 1$), having a semi-vertical angle α; $B = \cot\alpha$. For a spherical indenter of radius R, $d = 2$ and $B = 1/(2R)$. The previous expression was recently extended to indenters of non-axi-symmetric shape, such as pyramidal indenters that are frequently employed in depth-sensing indentation tests (Borodich et al., 2003):

$$f = B(\theta)\, r^d \tag{2.22}$$

where $B(\theta)$ describes the height of the indenter at a point $(\theta, r = 1)$. For a three-sided pyramid, $d = 1$, and making use of the triple symmetry:

$$B(\theta) = \cot\alpha_0 \sin(\pi/6 + \theta) \tag{2.23}$$

where α_0 is the angle in vertical cross-sections. For a Berkovich indenter, having a face angle of 115.13°, $\alpha_0 = 65.3°$; and for a cube corner indenter of 90° face angle, $\alpha_0 = 35.26°$.

2. The operators of constitutive relations F for the indented material is a homogeneous functions of degree κ with respect to the components of the strain tensor:

$$F(\lambda\boldsymbol{\varepsilon}) = \lambda^\kappa F(\boldsymbol{\varepsilon}) \tag{2.24}$$

Evidently, a linear elastic law satisfies this relation since $\kappa = 1$; as does any nonlinear secant elastic formulation of the form $\boldsymbol{\sigma} = \mathbb{C}(\boldsymbol{\varepsilon}) : \boldsymbol{\varepsilon}$ for which the secant elastic stiffness tensor satisfies:

$$\mathbb{C}(\lambda\boldsymbol{\varepsilon}) = \lambda^{\kappa-1}\mathbb{C}(\boldsymbol{\varepsilon}) \tag{2.25}$$

A similar reasoning applies to the dissipation function $\pi(\lambda\mathbf{d}) = \lambda^{\kappa}\pi(\mathbf{d})$ for yield design solutions based on expression (2.6).

Then provided the homogeneity of material properties and that the stress-strain relation remains the same for any depth of indentation, the whole load-displacement curve in a depth-sensing test can be scaled by (Borodich et al., 2003):

$$\frac{P}{P_1} = \left(\frac{h}{h_1}\right)^{\frac{2+\kappa(d-1)}{d}} ; \frac{h}{h_1} = \left(\frac{A}{A_1}\right)^{d/2} \tag{2.26}$$

where A is the projected contact area, which appears to be not affected by the constitutive relation. In return, the hardness is scaled with the indentation depth by:

$$\frac{H}{H_1} = \left(\frac{h}{h_1}\right)^{\frac{\kappa(d-1)}{d}} \tag{2.27}$$

We verify that the load-displacement relation is scaled by $P \propto h^2$ for conical and ideal (sharp) pyramidal indentation, for which $d = 1$, irrespective of the constitutive relation (2.24). As a consequence, the hardness is a constant over the loading process, as defined by (2.1). On the other hand, the constitutive relation power κ significantly affects the load-displacement relation for spherical or elliptic paraboloid indenter geometries, for which $d = 2$, and must be known in advance in order to analyze the load-displacement curve. For instance, for an elastic behavior, $P \propto h$ (which corresponds to $d \to \infty$) is indicative of flat indentation, and is described by Boussinesq's solution; $P \propto h^{1.5}$ is indicative of linear elastic spherical or paraboloids of revolution.

Finally, given the same $d = 1$ degree of the homogeneous shape function of three-sided pyramidal (Berkovich, corner cube) and conical indentation, it is common practice to consider, instead of the original three-dimensional pyramidal shape, an equivalent cone of revolution in sharp indentation analysis, such that the projected contact area with respect to indentation depth of the cone is the same as that for the real indenter, *ie.* from (2.26):

$$A(h) = C_0 h^2 = \pi (h \tan\alpha_{eq})^2 \Longrightarrow \tan\alpha_{eq} = \sqrt{\frac{C_0}{\pi}} \tag{2.28}$$

where C_0 is a constant characterizing the specific pyramidal indenter, and α_{eq} is the equivalent half-apex cone angle. Using (2.28), the flat Berkovich indenter ($\alpha_0 = 65.3°$), for which $C_0 = 24.56$, can be assimilated to an equivalent cone of semi-apex angle $\alpha_{eq}^{B} = 70.32°$; and a Corner Cube Corner indenter ($\alpha_0 = 35.26°; C_0 = 2.598$) to one with $\alpha_{eq}^{CC} = 42.28°$. The hardness-to-cohesion ratio vs. friction angle relation displayed in Figure 2, are the equivalent conical indentation results for a Berkovich and a Corner Cube indenter.

2.4 Link between Indentation Modulus and Elastic Properties of Transverse Isotropic Materials

Provided the contact area is known (as a function of the indentation depth), the hardness H and the indentation modulus M can be determined. As we have seen above, except for very specific behaviors, these two quantities are not material properties, but provide rather a snapshot of some strength behavior (H) and elasticity behavior (M), that needs to be linked to actual material properties: cohesion c, friction angle φ, elastic stiffness tensor $\mathbb{C}$, etc.

We restrict ourselves to linear elastic indentation analysis, for which the measured initial unloading slope S and the measured (or estimated) contact surface give access to the indentation modulus through the BASh equation (2.11). The analytical link between the indentation modulus and the elastic constants is provided through elastic solutions of the Hertz-type contact problem for specific indenter geometries. For rigid indenter, a convenient way of solving this problem consists of two steps: (1) determination of the Green's surface function, that is the displacement field corresponding to a concentrated unit load; and (2) integration of the Green's function to find the displacement field resulting from an assumed pressure distribution under the indenter, and verifying that the result matches with the boundary conditions of a rigid indenter. These boundary conditions are defined by the shape of the rigid indenter.

To illustrate the procedure, we consider first the conical indentation into a linear elastic isotropic half-space. The Green's surface function reads:

$$\eta(r) = \frac{\mathcal{H}}{r} \tag{2.29}$$

The contact area is a circle of radius a, and the pressure distribution is of the form:

$$p(r) = p_0 \cosh^{-1}\left(\frac{a}{r}\right) \tag{2.30}$$

where $p_0 = P/\left(\pi a^2\right)$ is the average pressure w.r.t. the projected contact area. The displacement at any point $Q(r_1, \theta)$ situated on the projected contact surface is:

$$u_1(r_1, \theta) = \int\int_S p(r)\ \eta(|r_1 - r|)\ r dr d\theta \tag{2.31}$$

The indentation depth h is equal to the displacement u_1 at the cone tip. Evaluating (2.31) for $r = 0$ gives:

$$h = u_1(r_1 = 0) = 2\pi\mathcal{H}p_0 \int_0^a \cosh^{-1}(a/r)\, dr = \pi\mathcal{H}\frac{P}{a} \tag{2.32}$$

or equivalently, after rearrangement:

$$P = \frac{2}{\pi}\frac{h^2 \tan\alpha}{\pi\mathcal{H}};\ S = \frac{2}{\sqrt{\pi}}\sqrt{A}\frac{1}{\pi\mathcal{H}} \tag{2.33}$$

A comparison of the expression (2.33) with the BASh equation (2.11) allows us to identify:

$$M = \frac{1}{\pi\mathcal{H}} \tag{2.34}$$

The simple example shows that the key to the establishment of the link between the indentation modulus M and the elastic constants of the indented half-space is the Green's surface function expression (2.29). In the general case, the Green's surface function reads (Vlassak and Nix, 1993, 1994):

$$\eta(\underline{y}) = \frac{1}{8\,\pi^2\,|\underline{y}|}\left[\alpha_k\; B^{-1}_{km}\left(\frac{\underline{y}}{|\underline{y}|}\right)\;\alpha_m\right] = \eta(r,\theta) = \frac{\mathcal{H}(\theta)}{r} \tag{2.35}$$

where $\underline{y}$ is the position vector of Q relative to the load point P; (r,θ) are polar coordinates of Q on the surface; $\alpha_1, \alpha_2, \alpha_3$ are the cosines of the direction normal to the indented surface; $\mathbf{B}$ is a second order tensor defined by (Barnett and Lothe, 1975):

$$B_{js}(\underline{t}) = B_{sj}(\underline{t}) = \frac{1}{8\pi^2}\int_0^{2\pi}((\mathbf{mm})_{js} - (\mathbf{mn})_{jk}\;(\mathbf{nn})^{-1}_{kr}\;(\mathbf{nm})_{rs})d\phi \tag{2.36}$$

where $(\mathbf{ab})_{jk} = a_i C_{ijkl} b_l$ (with the summation of repeated indices); $\underline{t} = \underline{y}/\,|\underline{y}|$ is the normalized form of $\underline{y}$; $(\underline{m}, \underline{n}, \underline{t})$ forms a right hand cartesian system, and ϕ is the angle between vector $\underline{m}$ and the unit normal outward to the surface (Figure 5a). And finally, $\eta(r,\theta)$ is the surface Green's function, homogenous in r^{-1}. For isotropic materials, it is convenient to employ the following form of the elastic stiffness tensor:

$$\mathbb{C} = (C_{11} + 2C_{12})\,\mathbb{J} + (C_{11} - C_{12})\,\mathbb{K} \tag{2.37}$$

where $\mathbb{J} = \frac{1}{3}\boldsymbol{\delta}\otimes\boldsymbol{\delta}$ and $\mathbb{K} = \mathbb{I} - \mathbb{J}$ are the spherical and the deviator tensor projection of the 4th order unit tensor, and $C_{11} = C_{1111}$ and $C_{12} = C_{1122}$ are the elasticity constants, related to the bulk and shear modulus by:

$$3K = C_{11} + 2C_{12};\; 2G = C_{11} - C_{12} \tag{2.38}$$

Use of (2.37) in (2.36) and (2.35) yields after some transformations,

$$\mathcal{H} = \frac{1}{\pi}\,\frac{C_{11}}{C_{11}^2 - C_{12}^2} \Rightarrow M = \frac{C_{11}^2 - C_{12}^2}{C_{11}} = \frac{E}{1-\nu^2} \tag{2.39}$$

Things are more complicated when it comes to anisotropic materials. Much of the recent contributions to the analysis of the Hertzian contact for anisotropic solids can be traced back to the 1966 work of Willis, who reduced the problem to the evaluation of contour integrals for parabolic indenters. Vlassak and Nix (1993, 1994) simplified the solution using the surface Green's function expression (2.35), and provided implicit solution schemes for other indenter shapes. To our knowledge, the most refined (recent) solution schemes for general anisotropic materials are those proposed by Swadener and Pharr (2001) for conical and parabolic indenters and by Vlassak *et al.* (2003) for conical and spherical indenters. Both solution schemes involve computational demanding operations even in their approximated versions. For orthotropic materials indented in the axes of symmetry, some easy implementable explicit expressions can be given, based on some approximations of the Green's function (Delafargue and Ulm, 2004). The principle is briefly evoked below for transversely isotropic materials.

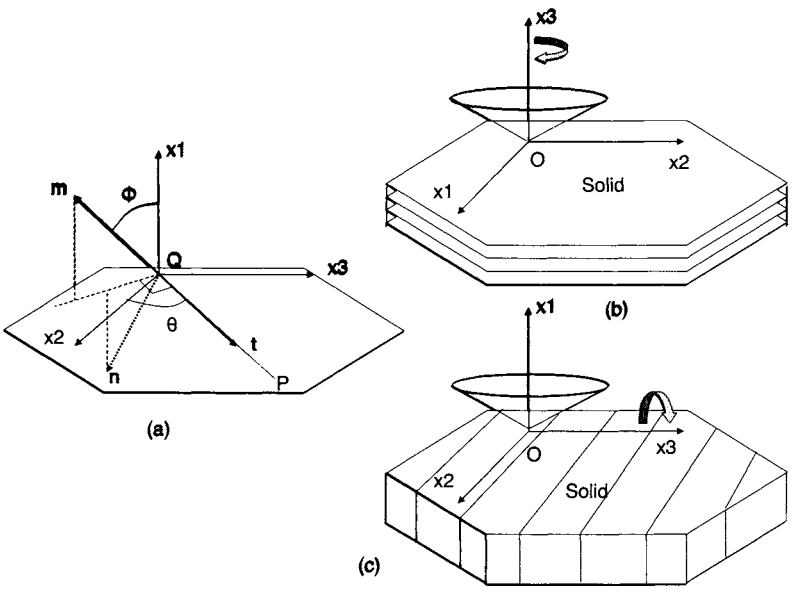

Figure 5. (a) Coordinate system; Indentation into (b) the axis of symmetry, and (c) into the plane of symmetry of a transversely isotropic material.

Let direction $x3$ be normal to the planes of isotropy of a transversely isotropic material; and directions $x1$ and $x2$ be parallel to the planes of isotropy so that the resulting coordinate system is a right-hand cartesian one, with the first indented point as origin O (Figure 5b). In this coordinate system, the elastic stiffness tensor is written in the form:

$$C_{ijkl} = \begin{bmatrix} C_{11} & C_{12} & C_{13} & 0 & 0 & 0 \\ & C_{11} & C_{13} & 0 & 0 & 0 \\ & & C_{33} & 0 & 0 & 0 \\ & & & 2C_{44} & 0 & 0 \\ & & & & 2C_{44} & 0 \\ sym & & & & & C_{11} - C_{12} \end{bmatrix} \tag{2.40}$$

where we use the reduced notations:[2]

$$\begin{aligned} C_{11} &= C_{1111} \\ C_{12} &= C_{1122} = C_{2211} \\ C_{13} &= C_{1133} = C_{3311} \\ C_{11} - C_{12} &= 2C_{1212} \\ C_{44} &= C_{2323} = C_{1313} \\ C_{31} &= \sqrt{C_{11}\, C_{33}} > C_{13};\ \text{with } C_{33} = C_{3333} \end{aligned} \tag{2.41}$$

[2]The last condition in (2.41), $C_{31} = \sqrt{C_{11}\, C_{33}} > C_{13}$, ensures that the stiffness tensor is symmetric positive definite.

We are first interested in an indentation in direction $x3$, *ie.* normal to the planes of isotropy. For this case, an analytical solution of the Hertz contact problem for conical indentation is available. The Elliot-Hanson solution reads (Elliot, 1949; Hanson, 1992):

$$P = \frac{2}{\pi^2 \mathcal{H}} \, h^2 \, \tan(\alpha) \tag{2.42}$$

where $\mathcal{H}$ is the constant:

$$\mathcal{H} = \frac{1}{2\,\pi} \sqrt{\frac{C_{11}}{C_{31}^2 - C_{13}^2} \left(\frac{1}{C_{44}} + \frac{2}{C_{31} + C_{13}} \right)} \tag{2.43}$$

A derivation of (2.42) w.r.t. to h yields the BASh equation (2.11), together with the indentation modulus in the axis of symmetry $x3$:

$$M_3 = \frac{1}{\pi \mathcal{H}} = 2 \sqrt{\frac{C_{31}^2 - C_{13}^2}{C_{11}} \left(\frac{1}{C_{44}} + \frac{2}{C_{31} + C_{13}} \right)^{-1}} \tag{2.44}$$

It is interesting to note that the solution does only depend on four of the five elastic constants of a transversely isotropic material $(C_{11}, C_{33}, C_{44}, C_{13})$. The fifth independent constant $C_{12} = C_{1122} = C_{1111} - 2\,C_{1212}$ does not appear in the expression of $\mathcal{H}$.

When the half-space surface is orthogonal to the material's planes of isotropy, the problem is no longer axi-symmetric and the projected contact area is no more circular. We consider an indentation into axis $x1$ of the half-space. The indentation axis $(x1)$ belongs to two planes of symmetry (Fig. 5c): $(x1, x3)$ is orthogonal to the planes of isotropy, and $(x1, x2)$ is parallel to them. In this case, an evaluation of (2.35) for $(\alpha_1, \alpha_2, \alpha_3) = (1, 0, 0)$ yields the exact values of the the Green's function η in the $x2-$direction $(\theta = 0)$, and in the $x3-$direction $(\theta = \pi/2)$:

$$\mathcal{H}_2 = \mathcal{H}(\theta = 0) = \frac{1}{2\,\pi} \sqrt{\frac{C_{33}}{C_{31}^2 - C_{13}^2} \left(\frac{1}{C_{44}} + \frac{2}{C_{31} + C_{13}} \right)} \tag{2.45}$$

$$\mathcal{H}_3 = \mathcal{H}(\theta = \frac{\pi}{2}) = \frac{1}{\pi} \, \frac{C_{11}}{C_{11}^2 - C_{12}^2} \tag{2.46}$$

It is interesting to note, from a comparison of (2.43) and (2.45), that $\mathcal{H}_2 = \sqrt{C_{33}/C_{11}}\,\mathcal{H}$; while $\mathcal{H}_3$ turns out to be the Green's function constant for an isotropic material with stiffness constants $C_{11} = C_{1111}$ and $C_{12} = C_{1122}$, as defined by (2.39). Furthermore, since the Green's function is π-periodic by definition and even by symmetry, $\mathcal{H}_2$ and $\mathcal{H}_3$ are extreme values of $\mathcal{H}(\theta)$. Restricted to indentation in principal material axes, it seems appropriate to consider a first order approximation $\widetilde{\mathcal{H}}(\theta)$ that interpolates the Green's function $\eta(r, \theta) \simeq \widetilde{\mathcal{H}}(\theta)/r$ so that $\widetilde{\mathcal{H}}(\theta = 0) = \mathcal{H}_2$ and $\widetilde{\mathcal{H}}(\theta = \frac{\pi}{2}) = \mathcal{H}_3$:

$$\widetilde{\mathcal{H}}(\theta) = \frac{\mathcal{H}_2 + \mathcal{H}_3}{2} + \frac{\mathcal{H}_2 - \mathcal{H}_3}{2} \cos(2\theta) \tag{2.47}$$

Finally, to complete the determination, we need to specify the shape of the contact area and the pressure distribution. It is generally assumed that the projected contact area

is elliptical for conical indentation of general anisotropic materials. By symmetry, the axes of the elliptical contact area must coincide with $x2$ and $x3$. If a_2 and a_3 are the ellipse dimensions in the respective directions $x2$ and $x3$, then the ellipse eccentricity is $e = \sqrt{1 - \left(\frac{a_2}{a_3}\right)^2}$ if $a_2 < a_3$, and $e = \sqrt{1 - \left(\frac{a_3}{a_2}\right)^2}$ otherwise. We assume that the pressure field $p(y_2, y_3)$ at point P of coordinates (y_2, y_3) has the form (Swadener and Pharr, 2001):

$$p(y_2, y_3) = p_0 \ \cosh^{-1}\left(\frac{y_2^2}{a_2^2} + \frac{y_3^2}{a_3^2}\right)^{-1/2} \tag{2.48}$$

The displacement in any point $Q(z_2, z_3)$ situated on the projected contact surface is:

$$u_1(z_2, z_3) = \int\int_S p(y_2, y_3)\ \eta(z_2 - y_2, z_3 - y_3)\ dy_2 dy_3 \tag{2.49}$$

Substituting in η the Green's function approximation (2.47), and proceeding as in the isotropic case, we evaluate the indentation depth h from the displacement u_1 at the cone tip, and express it as a function of the load $P = \pi a_2 a_3 p_0$. Deriving this expression yields together with the BASh equation (2.11) the following expression of the indentation modulus M_1:

$$M_1 = \Psi(e)\frac{1}{\pi\sqrt{\mathcal{H}_2\,\mathcal{H}_3}};\ \Psi(e) = \pi\frac{(1-e^2)^{1/4}}{2\ \mathcal{E}(e)} \tag{2.50}$$

where $\mathcal{E}(e)$ is the complete elliptic integral of the second kind, and e the eccentricity, which for the Green's function approximation (2.47) reads:

$$e = \left\{ \sqrt{1 - \frac{\mathcal{H}_2}{\mathcal{H}_3}},\ \text{if } \mathcal{H}_2 < \mathcal{H}_3\ ,\ \sqrt{1 - \frac{\mathcal{H}_3}{\mathcal{H}_2}},\ \text{else} \right\} \tag{2.51}$$

We note that $0.99 \leq \Psi(e) \leq 1$ if $e \leq 0.6$, which corresponds to an ellipse axis ratio smaller that 1.25. Hence, using $\Psi(e) \approx 1$ in (2.50) simplifies the expression of the indentation modulus normal to the axis of symmetry:

$$M_1 \simeq \frac{1}{\pi\sqrt{\mathcal{H}_2\mathcal{H}_3}} = \sqrt{\sqrt{\frac{C_{11}}{C_{33}}}\frac{C_{11}^2 - C_{12}^2}{C_{11}}M_3} \tag{2.52}$$

where M_3 is the indentation modulus in the axis of symmetry.

In summary, relations (2.44) and (2.52) highlight that indentation moduli provide an intriguing snapshot of the elasticity activated in an indentation test. They also highlight the difficulty to directly determine for non-isotropic materials the elastic constants from indentation tests, as it would require five tests in different directions in order to determine five 'snapshots' of the transversely isotropic elasticity. The feasibility of such an endeavour can be checked using the two indentation moduli, M_1 and M_3, in the principal material axes, as they are expected to provide the highest contrast in elastic behavior of the material.

2.5 Indentation on Natural Composites

Is it possible to apply continuum indentation analysis to heterogeneous materials, and if – how?

Continuum indentation analysis is generally based on the assumption of homogeneity of material properties and that the stress-strain relation remains the same for any depth of indentation. Like all continuum analysis, continuum indentation analysis is based on the concept of a representative elementary volume (r.e.v.) of characteristic size $\mathcal{L}$ that needs to obey to the scale separability condition:

$$d \ll \mathcal{L} \ll \max(h, a) \tag{2.53}$$

where (h, a) is the indentation depth and the indentation radius that define the order of magnitude of the variation of the position vector $\underline{x}$; and d is the characteristic size of the (largest) heterogeneity contained in the r.e.v. Provided that (2.53) is satisfied, an indentation test operated to a penetration depth h gives access to the material properties that are characteristic of a materials system at a length scale of $\mathcal{L}$. On the other hand, since most indentation solutions are based on the similarity approach, and derived from the infinite half-space model (which by definition has no length scale), and from the assumption of uniform material properties, the properties extracted –by means of an inverse analysis– from indentation tests are averaged quantities characteristic of a material length scale defined by the indentation depth or the indentation radius. A good estimate is that the characteristic size of the material domain sensed by an indentation is on the order of $\max(h, a)$; roughly $3h$ for Berkovich indentation and h for the corner cube. Given the self-similarity of the indentation test, choosing the indentation depth, therefore, comes to choose the length scale of material investigation.

The heterogeneity of most natural composite materials down to very fine scales calls for a statistical analysis of indentation results. This requires that a large number of indentation tests be performed on a surface. A convenient way is to employ a grid indentation technique, defined by a grid size ℓ that should be larger than the characteristic size of the indentation impression, so to avoid interference in between individual indentation tests (Fig. 6).

Thought Experiment *Consider a material to be composed of two individual phases of characteristic size D_1 and D_2, and different material properties. If the indentation depth is much smaller than the characteristic size of the phases, $h \ll (D_1, D_2)$, then a single indentation test gives access to the material properties of either phase 1 or phase 2. If, in addition, a large number of tests is carried out on a grid size that is much larger than the characteristic size of the two phases, so that the locus of indentation has no statistical bias w.r.t. the spatial distribution of the two phases, the probability of encountering one or the other phase is equal to the surface fraction occupied by the two phases on the indentation surface. Provided that a similar distribution is found equally on other surfaces, the surface fraction can be assimilated with the volume fraction of the two phases present in the material.*

Consider next an indentation test performed to a maximum indentation depth that is much larger than the characteristic size of the individual phases, $h \gg (D_1, D_2)$. It

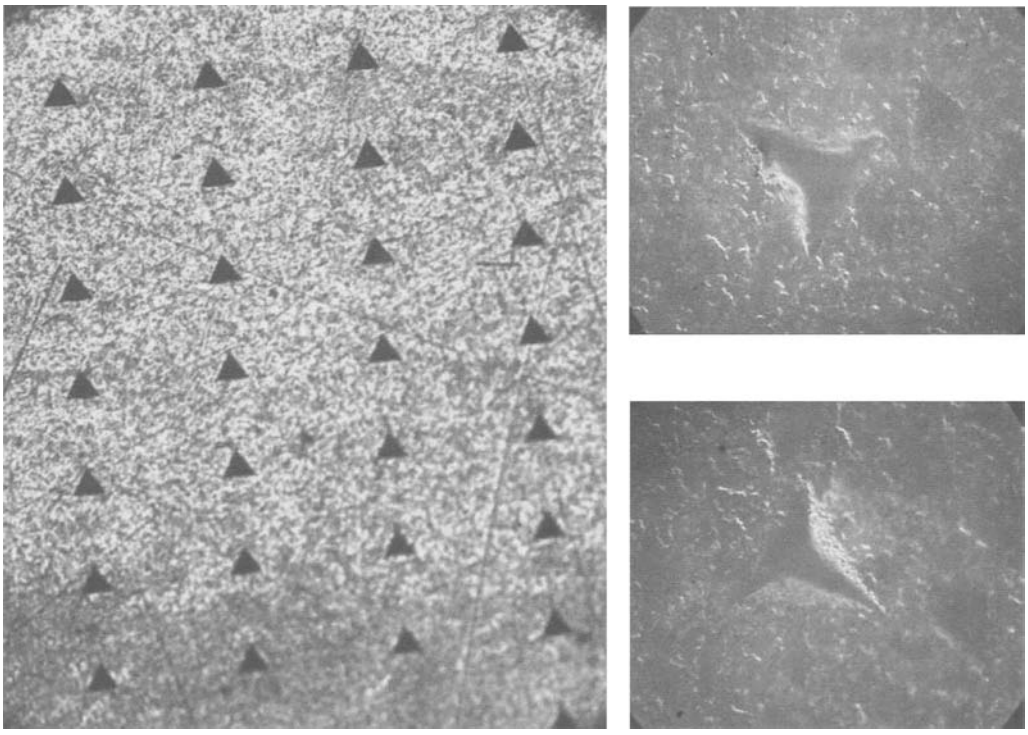

Figure 6. Optical microscope images of indentation grid: (left) example of microindentation grid on a cement paste; (right) residual impression after unloading (magnification x100).

is readily understood, from the scale separability condition (2.53), that the properties extracted from such an indentation test are representative in a statistical sense of the average properties of the composite material.

The simple thought-experiment has all the ingredients of statistical indentation analysis that need to be performed when it comes to natural composite materials. The key results of such analysis are distributions and their derivatives (*ie.* histograms or frequency plots) of mechanical properties determined by a large number of indentation tests at a specific scale of material observation defined by the indentation depth. Generally speaking, small indentation depths give access to mechanical phase properties, and potentially to volume fractions, from (Constantinides et al., 2003):

$$f_i = \frac{N_i}{N}; \quad \sum_{i=1}^{n} N_i = N \tag{2.54}$$

where N_i is the number of indentations on material phase i, that can be identified by

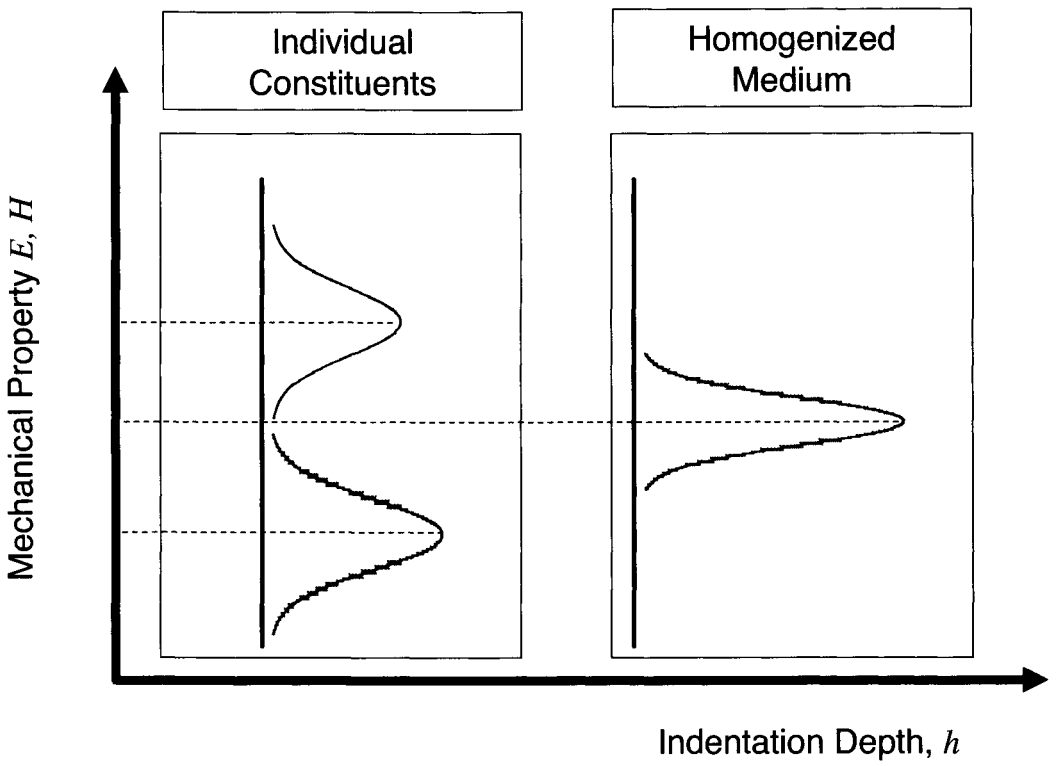

Figure 7. Principle of statistical indentation analysis of natural composites: small indentation depths give access to properties of individual phases; large indentation depths yield a homogenized response of the material.

the difference in material properties; that is f_i is the volume fraction of a 'mechanically' identifiable material phase. In turn, greater indentation depths give access to homogenized material properties of the composite (Fig. 7). Finally, a mapping of mechanical properties allows one to identify (if any) characteristic morphologies within the resolution defined by the grid size. These are all inputs required for microporomechanics analysis.

3 Experimental Microporomechanics of Cement-Based Materials

A nanoindentation investigation starts with an understanding of the microstructure of the investigated material, and *vice versa*, nanoindentation provides a means to identify the microstructure and the link between microstructure and material properties; and ultimately material invariant material properties. This is illustrated here for cement-based materials.[3]

3.1 Multiscale Microstructural Think-Model of Cement-Based Materials

Cement-based materials, like many geomaterials, are highly heterogeneous materials, with heterogeneities that manifest themselves from the nanoscale to the macroscale. For purpose of a poromechanics analysis, it is convenient to break this highly heterogeneous material system down into different scales defined by characteristic sizes of heterogeneities which are often the porosity. Figure 8 displays a four-level microstructural think-model of cement-based materials, which is detailed below.

Level '0': Nanoscale The lowest level of a mechanical representation of the complex microstructure of cement-based materials is the largest scale at which the material properties do not change from one cement-based material to another. It is the scale, where physical chemistry meets mechanics; that is the material properties are solely defined by the physical chemistry of the formation process of the material. This scale is typically situated above the atomic scale. In the case of cement-based materials, it is the scale of the C-S-H solid that forms at early ages by the hydration of C_3S and C_2S.[4] We refer to this scale as level '0', since this scale is currently not accessible to mechanical testing. This scale has been the focus of many theoretical and experimental cement chemistry investigations, starting with the groundbreaking works of Powers and his colleagues at the Portland Cement Association (Powers and Brownyard, 1948) recognizing the colloidal and gel-like properties of the C-S-H component. Powers attributed a porosity of roughly 28% to this solid phase. Ever since, many models have been devised to characterize the microstructure with an emphasis on a layered structure of C-S-H. To cite a few, the well known Feldman-Sereda model postulated the existence of 'interlayer spaces' in the C-S-H gel, containing strongly adsorbed water (Feldman and Sereda, 1970). Wittmann's Munich model is based on some concepts of colloidal science, relying particularly on the idea of a disjoining pressure that develops in the interlayer space as a consequence of hindered adsorption (Wittmann, 1974, 1988). Similar conclusions were arrived at by other authors as well (see e.g. Bažant (1972)): given the characteristic size of the interlayer space of

[3]The investigation of the fundamental properties of cement-based materials was carried out in a collaborative research project with the Lafarge Corp., with Dr. Paul Acker as Scientific Advisor and Jean-Francois Batoz as manager. The financial support of this study by the Lafarge Corporation is gratefully acknowledged. The investigated heat-cured specimen were provided by the Northwestern University team of Profs. Hamlin Jennings and Jeffrey Thomas (Civil Engineering and Materials Science), whose collaboration, comments and suggestions is gratefully acknowledged.

[4]The cement's chemistry abbreviation will be used in this paper (C_3S = 3·CaO·SiO_2, C_2S = 2·CaO·SiO_2, C_3A = 3·CaO·Al_2O_3, C_4AF = 4·CaO·Al_2O_3·Fe_2O_3).

LEVEL	Density $[kg/m^3]$		Porosity [%]	Source
0: C-S-H solid	ρ_{sat}	ρ_{dry}	φ_0, ϕ_0	
Basic Building Block	2,800		–	Jennings, 2004[a]
Globules	2,480	2,300	18[b]	Jennings, 2004[a]
I: C-S-H matrix				
C-S-H_{LD}	1,930	1,440	37.3 ± 0.1[c]	Jennings, 2004[a]
C-S-H_{HD}	2,130	1,750	23.7 ± 0.1[c]	Jennings, 2004[a]
II: Cement paste				
C_3S-Clinker	$\rho_c \frac{m_{C_3S}}{\sum_X m_X}$ [d]		–	
C_2S-Clinker	$\rho_c \frac{m_{C_2S}}{\sum_X m_X}$ [d]		–	
C_3A-Clinker	$\rho_c \frac{m_{C_3A}}{\sum_X m_X}$ [d]		–	
C_4AF-Clinker	$\rho_c \frac{m_{C_4AF}}{\sum_X m_X}$ [d]		–	
CH	2,240		–	
III: Mortar				
Sand	2,650		–	Heukamp and Ulm, 2002

Table 1. Intrinsic properties of cement paste and mortar constituents:
[a] Density values of C-S-H as predicted from the quantitative colloidal model of C-S-H by Jennings (2000, 2004).
[b] Nanoporosity (intra-globules porosity) filled by structural water;
[c] Gelporosity (inter-globules porosity) of low density and high density C-S-H (excludes nanoporosity);
[d] p = total porosity = change in mass content due to drying at 105° C; includes structural water in nanoporosity and bulk water in gelporosity;
[e] Clinker density determined from cement density $\rho_c = 3,150$ kg/m^3, and the mass proportions m_X of the four clinker phases ($X = C_3S, C_2S, C_3A, C_4AF$) in the cement which are provided by the cement producer.

less than ten water molecules in size (elementary dimension of water is distance between O-atoms 0.284×10^{-9} m), it was quickly recognized that the water in this space cannot be considered to be a bulk water phase, to which e.g. Stokes equations apply. Instead, the mechanical response at this scale is dominated by the surface properties of the C-S-H gel, and the water present at this scale is structural water. Very recently, Jennings in a number of papers (Jennings, 2000; Tennis and Jennings, 2000; Jennings, 2004), provided qualitative and quantitative evidence of an amorphous colloidal structure of the C-S-H, organized in 'globules' (see Fig. 9), composed of basic building blocks and an intra-globules porosity. The way by which the porosity can be assessed, at this scale, is from mass density measurements (see Table 1). This porosity which manifests itself at a scale smaller than the characteristic solid dimension of 2.2×10^{-9} m, is $\varphi_0 = 18\%$ irrespective of the type of C-S-H. Instead, it is intrinsic to the C-S-H solid phase, and can be associated with the nanoporosity filled by structural water (and not bulk wa-

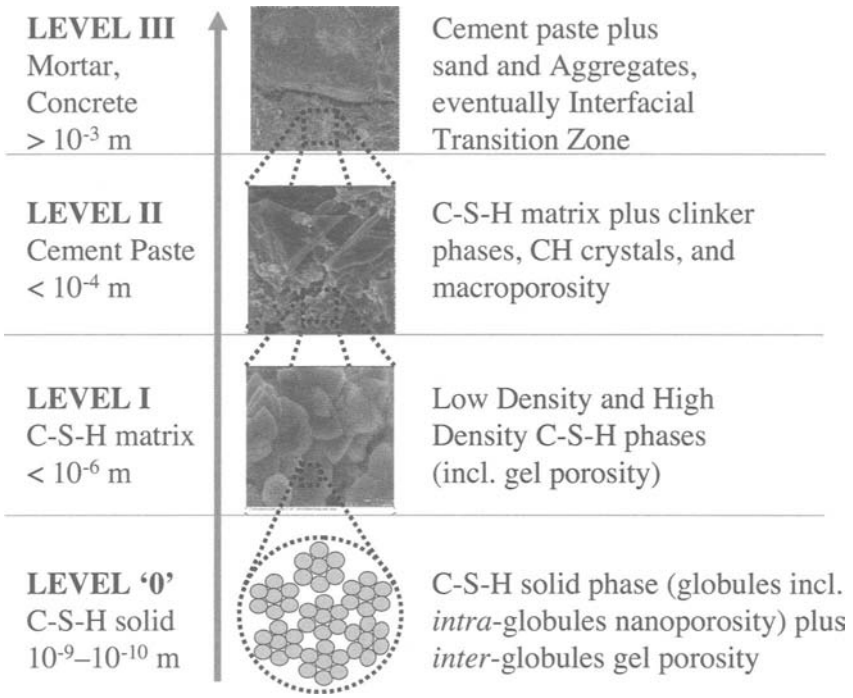

Figure 8. Four-level microstructural think-model of cement-based materials.

ter). Above this scale, there is a second type of porosity, the gel porosity, but which was found to differ from one type of C-S-H to another, as detailed below. Hence, from a poromechanics point of view, it is appropriate to consider this solid phase ('globules' in Jennings terminology) which includes a 18% intra-solid porosity filled by structural water, as the elementary solid phase of a poromechanics representation of cement-based materials. This solid phase has been found to be of a characteristic size of 5.6×10^{-9} m.

Level 'I': C-S-H phases – Gel Porosity – C-S-H matrix The solid phase of level '0' together with gel-porosity forms different types of C-S-H phases. These phases manifest themselves in units roughly larger than 16.6×10^{-9} m (Jennings, 2004), as sketched in Figure 9. We refer to this level as level I, as it represents the smallest material length scale that is presently accessible by mechanical testing, *ie.* nanoindentation (Constantinides et al., 2003; Constantinides and Ulm, 2004). At level I, the C-S-H exists in at least two different forms, a low density (LD) and a high density (HD) form (Fig. 9). The difference between the two types of C-S-H relates to the gel porosity of roughly 24% for HD–C-S-H, and 37% for LD–C-S-H (Jennings, 2000), due to the different packing density of the C-S-H solid of the two types of C-S-H; in addition to the 18% nanoporosity within the C-S-H solid phase (at level '0'); see Figure 9. In contrast to the nanoporosity, the gel

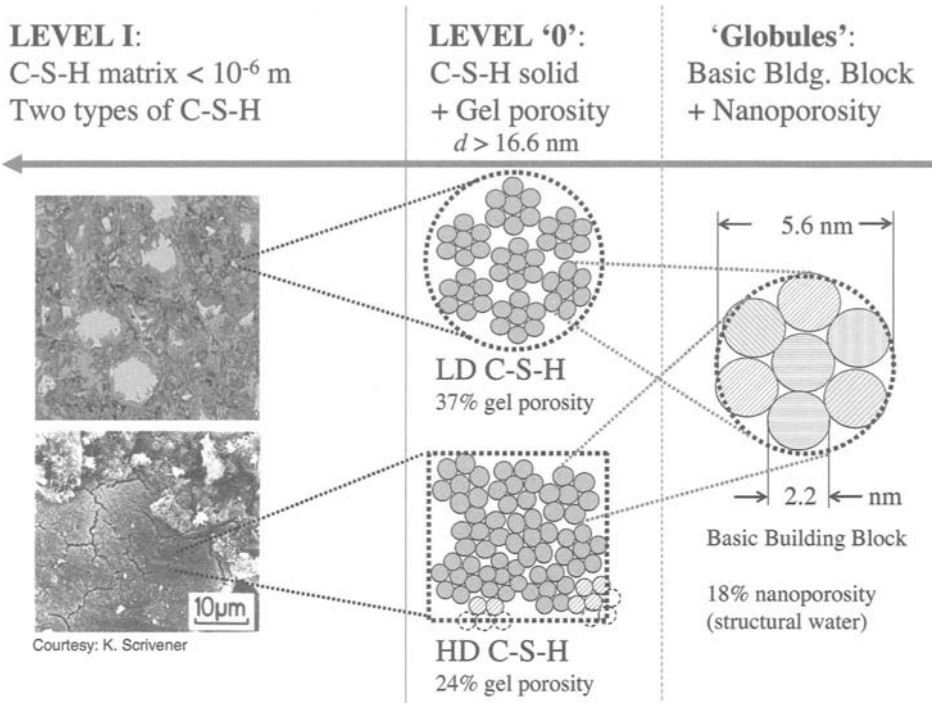

Figure 9. The Jennings colloid model of the two-types of C-S-H (Jennings, 2000; Tennis and Jennings, 2000; Jennings, 2004).

porosity has a characteristic dimension of the solid phase, *ie.* on the order of 5.6×10^{-9} m, in which the water present can be considered as a bulk water phase – in the sense of poromechanics theory. The gel porosity can be defined in a standard manner:

$$\phi_0^{LD} = \frac{V_{f,LD}}{V_{LD}} = 0.37; \quad \phi_0^{HD} = \frac{V_{f,HD}}{V_{HD}} = 0.24 \tag{3.1}$$

where $V_{f,J}$ is the pore volume, and V_J the reference volume ($J = HD, LD$). The gel porosity values are also intrinsic to all cement-based materials: they are a consequence of the formation process of C-S-H in the course of hydration. That what changes from one cement paste material to the other is the volumetric proportion of HD–C-S-H and LD–C-S-H, within the C-S-H matrix.

It is intriguing to remark that the LD–C-S-H packing density, $1 - \phi_0^{LD} = 0.63$, almost coincides with the random packing density of spheres of 64%, which corresponds to the maximum packing density in the random close-packed limit (known as RCP)[5]. In return,

[5] More recent concepts refer to the RCP as the maximally random jammed state (MRJ), corresponding to the least ordered among all jammed packings, which has been shown to have

the HD–C-S-H packing density, $1 - \phi_0^{HD} = 0.76$ exceeds by little the densest possible spherical packing in three-dimensions of 74% (a problem known as the Kepler problem (Jaeger and Nagel, 1992; Sloane, 1998; Donev et al., 2004), which is the close-packed hexagonal or cubic structure. This is significant as it would confirm the underlying conjecture of the Jennings colloid model, that the two types of C-S-H are manifestations of the same solid, the only difference being an unstructured (random) order of the LD–C-S-H vs. a highly structured order of the HD–C-S-H.

Level 'II': Capillary Porosity – n Solid phases Level II refers to the cement paste, which manifests itself at a characteristic length scale of $10^{-6} - 10^{-4}$ m (Fig. 8). At this scale, the porous C–S–H matrix composed of two types of C-S-H together with the unhydrated cement products (*ie.* the four clinker phases C_3S, C_2S, C_3A, C_4AF), large Portlandite crystals ($CH = Ca(OH)_2$), aluminates and the macro-porosity ϕ_0 (which is often referred to as capillary porosity, and which is generally present only in high w/c–materials) form the cement paste. The total porosity p of a cement paste is the sum of the nanoporosity, the gel-porosity and the capillary porosity (Ulm et al., 2004):

$$p^{II} = [\varphi_0 (1 - \phi_{LD}) + \phi_{LD}] f_{LD} + [\varphi_0 (1 - \phi_{HD}) + \phi_{HD}] f_{HD} + \phi_0 \tag{3.2}$$

where f_{LD} and f_{HD} represent the volume fractions of the LD–C-S-H phase and the HD–C-S-H phase present in the cement paste. The total porosity is the relative change of mass that is measured by means of weighting experiments on a fully saturated and a dried cement paste oven dried at 105°C. By contrast, other techniques such as poromercury intrusion (PMI), do not allow to assess the total porosity, as the technique typically fails for pore throat radii smaller than 7×10^{-9} m. From a poromechanics point of view, the porosity which is filled by a bulk water phase is the total porosity minus the nanoporosity (filled by structural water):

$$\phi_0^{II} = \phi_{LD} f_{LD} + \phi_{HD} f_{HD} + \phi_0 \tag{3.3}$$

The dominating phase, at this scale, is the porous C-S-H matrix, which can occupy up to 90% of the volume of a cement paste.

Level 'III': Mortar and Concrete Level III of a characteristic length scale greater than 10^{-3}m refers to mortar and concrete; that is a composite material composed of a porous cement paste matrix, and sand particle inclusions in the case of mortar, and additional aggregate inclusions in the case of concrete. Some authors consider in addition the Interfacial Transition Zone (ITZ) between inclusions and matrix, which has been focus of many micromechanical modeling attempts (e.g. Garboczi, 1993; Li et al., 1999; Hashin and Monteiro, 2002; Heukamp and Ulm, 2002). From a poromechanics point of view, the cement paste matrix is a porous matrix, while –except for special applications– any porosity contained in the aggregates is rather of occluded nature. The total porosity at level III, that can be assessed by weighting experiments, is:

$$p^{III} = (1 - f_I) p^{II} + \left(\phi_{ITZ} - p^{II}\right) f_{ITZ} \tag{3.4}$$

a density of 63.7%, which is very close the traditional definition of the random close-packed limit; see Donev et al. (2004), and references cited herein.

where f_I and f_{ITZ} represent the volume fractions of the inclusions and of the ITZ, while ϕ_{ITZ} is the porosity of the ITZ, which has been argued to differ (in some cases) from the porosity of the cement paste. A lower bound of the inclusion volume fraction is obtained by letting $\phi_{ITZ} = p^{II}$.

3.2 Indentation Analysis

Indentation tests on cementitious materials have been reported by several authors: Igarashi et al. (1996) used a Vickers indenter (four-sided pyramid) with a maximum penetration depth on the order of $h_{\max} \simeq 10^{-5}$m, which gives access to the bulk properties of cement paste at a sub-millimeter to millimeter material length scale. To our knowledge, the first nanoindentation results of constituents of Portland cement were provided by Velez et al. (2001) and Acker (2001). The first reported nanoindentation results of the elastic modulus and hardness of the major clinker phases (C_2S,C_3S, C_3A, C_4AF), and the second provided values for Portlandite (CH=$Ca(OH)_2$) and the C-S-H gel for different C/S-ratio. These results were obtained on an ultra-high performance cementitious composite material, DUCTAL^{TM}, with a Berkovich indenter with penetration depths of about $h_{\max} \simeq 0.3 - 0.5 \times 10^{-6}$m; corresponding thus to bulk properties of the different phases at a characteristic length scale in the micrometer range. The stiffness value for CH was confirmed by Constantinides and Ulm (2004), who provided stiffness values of the two types of C-S-H of an ordinary Portlandite cement paste prepared at a water-cement ratio of $w/c = 0.5$, in a non-degraded and an asymptotically leached state. The key result obtained by this investigation was that the stiffness property of the two types of C-S-H obtained by nanoindentation at level I are independent of the mix proportions of the material (see also Constantinides et al. (2003)). Ever since, the question has been raised why?

Recently, we performed a series of tests on heat-cured cement paste samples, that provide some hints as to the origin of the invariant nature of the C-S-H properties (Constantinides and Ulm, 2004b). The general interest in the behavior of heat treated cementitious materials stems from the use of high-temperature curing in concrete technology for obtaining both a high early-strength and a significant decrease of time dependent deformation (creep and shrinkage), particularly in the precast concrete industry. However, it was quickly recognized that long-term properties are often negatively influenced by elevated curing temperature, as strength and other mechanical properties are often reduced and permeability increased. Beyond this particular industrial context, what we aim to show is the synergy of nanoindentation and microporomechanics analysis for understanding and assessment of the properties of complex natural composites, such as cementitious materials.

The cement paste samples were prepared using a white portland cement with a low aluminates content (US Gypsum Co., Chicago, IL) at a water/cement ratio of $w/c = 0.5$, to form bars measuring 0.25 m $\times$0.025 m $\times$0.025 m. The paste was hydrated under limewater at room temperature (Control specimen, labeled 'C'), and at a temperature of 60 °C for 28 days (Heat-cured specimen, labeled 'HC-28'). The heat curing was performed using the procedure described by Thomas and Jennings (2002): specimen were placed into a programmable water bath of limewater, and the temperature was controlled

Specimen	Control (C)	HC-28
w/c [1]	0.5	0.5
Heat-curing duration [d]	0	28
Age [mth]	5	5
No. of Micro-Tests	10 (MM*)	30 (MM*)
No. of Nano-Tests	200 (HYS**)	509 (HYS**)

Table 2. Specimen description and experimental program. Control specimen was cured at 20° C. Heat curing temperature was 60° C. After heat-curing specimens were kept at 20° C. Micro-Tests refer to microindentation tests operated with a maximum indentation depth of 10×10^{-6} m, Nano-Tests refer to nanoindentation tests operated with a maximum indentation depth of 300 nm. Machines: (*) MM = MicroMaterials, (**) HYS = Hysitron.

using a thermometer placed next to the specimen. The maximum temperature of 60 °C was chosen to avoid secondary high-temperature reactions, such as the decomposition of ettringite into monosulfate, which would hamper interpretation of the results. After the heat curing, the specimen were cooled to room temperature under sealed conditions, and kept in limewater until testing. The tested specimen, w/c ratio and age at testing are reported in Table 2. For the indentation testing, the square plate specimens were cut into slices of approximate thickness 5 – 10 mm. The surfaces were ground and polished with silicon carbide papers and diamond particles to obtain a very flat and smooth surface finish. This was achieved in 6 stages of decreasing fineness with the last one being in the range of 0.25×10^{-6} m. Such a smooth surface is of critical importance for nanoindentation tests, so to avoid introducing another length scale in the similarity analysis: the surface roughness. Furthermore, special attention was paid to keep the specimens flat and parallel on both sides, since this could influence the angle of indentation and thus the result of the measurements. After polishing, the samples were placed in an ultrasonic bath to remove the dust and diamond particles left on the surface or in the pore structure.

Nanoindentation: Frequency Plots The first investigation focusses on level I and II, *ie.* on the material properties of the two-types of C-S-H. Given that the gel porosity has a characteristic dimension $\leq 10^{-8}$ m (see Fig. 9) an indentation test that captures the composite behavior of the two types of C-S-H must be on the order of $h \geq 10^{-7}$ m. Following previous experience with nanoindentation on cementitious materials (Acker, 2001; Constantinides et al., 2003; Constantinides and Ulm, 2004), a maximum penetration depth of 300 nm was chosen in the nanoindentation campaign carried out with a Berkovich indenter. 100 to 500 nanoindentation tests (see Table 2) were programmed with a grid-size of 10^{-5} m so to avoid interference in between single indents (see Fig. 6). The results are analyzed in terms of histograms of the mechanical properties (frequency plots).

Frequency plots of the nanoindentation stiffness are displayed in Figures 10 for the control specimen ('C') and the 28 day heat cured specimen ('HC-28'). The histograms

display the frequency with which a specific stiffness is encountered in the experiment. The figures display a clear multi-modal distribution of the mechanical properties. Each peak corresponds to the mechanical manifestation of a chemical-morphological unit present in the microstructure. The intensity of each mechanical manifestation is representative of the intrinsic property of the phase. These are the macro-porosity, the LD–C-S-H, the HD–C-S-H, and Portlandite (CH) and residual clinker phases. The clear multi-modal distribution of these phases in Figure 10 makes it easy to graphically determine from a combination of the frequency plot and the cumulative distribution (*ie.* integral of the frequency plot), the intrinsic properties of the different phases and the volume fractions. These values are summarized in Table 3.

The indentation modulus of the LD–C-S-H and HD–C-S-H is in perfect agreement with previous reported results obtained on other cementitious materials: Acker (2001) reported two nanoindentation stiffness values for DUCTAL^{TM}, a thermally treated Ultra-High-Performance Cementitious Composite Material with $w/c < 0.20$, for which $M_{LD} = 20 \pm 2$ GPa and $M_{HD} = 31 \pm 4$ GPa. In a previous nanoindentation test campaign on another $w/c = 0.5$ hardened cement paste (Constantinides et al., 2003; Constantinides and Ulm, 2004), we found $M_{LD} = 23 \pm 2$ GPa and $M_{HD} = 31 \pm 2$ GPa. These indentation moduli are almost not affected by the thermal curing: the LD–C-S-H remains at a value of $M_{LD} = 20$ GPa, and the one of HD–C-S-H shifts only slightly from $M_{HD} = 29$ GPa for the control specimen to $M_{HD} = 31$ GPa for the thermally cured specimens, which is surely smaller than the standard deviation; and hence statistically insignificant. The almost perfect agreement with previous reported values clearly confirms that the stiffness values of the two C-S-H phases are independent not only of the mix proportion, but as well of the thermal curing in the considered temperature range and of thermal treatment (DUCTAL^{TM}). Instead, these properties are intrinsic to the formation process of the C-S-H phases.

That what changes due to thermal curing are the volumetric proportions of the different phases. The heat curing appears to favor the formation of high-density C-S-H. The relative proportion of LD-to-HD C-S-H shifts from $55/30 = 1.8$ in the control specimen to $33/45 = 0.73$ in the 28-day heat cured specimen ('HC-28'). Heat treatment, therefore, appears to be associated with a densification of the C-S-H matrix at Level I. In return, this densification of the matrix appears to occur at the expense of an increase in porosity at the considered scale. Given the indentation depth of 300 nm, this porosity has a characteristic size equal or greater than 300 nm. If we attribute an indentation stiffness ≤ 5 MPa to a nanoindentation into a bulk phase dominated by this macroporosity, the volume fraction obtained from the cumulative distribution in Figure 10 increases from 2% for the control specimen, to 8% for HC-28. What is interesting to note is that the total porosity as defined (3.2) does not change. Indeed, using the volume fractions from Table 3 in (3.2) yields a total porosity for the control specimen of $p^{II}(C) = 40\%$ and for the heat-cured specimen of $p^{II}(C) = 41\%$. The almost perfect agreement of the total porosity of control specimen and heat-cured specimen confirms that the creation of the macroporosity due to heat curing is a consequence of the conversion of LD–C-S-H (having a gelporosity of 37%) into HD–C-S-H (having a gelporosity of 24%). This conversion reduces the mesoporosity, *ie.* the total gelporosity in both LD–C-S-H and HD–C-S-H, but is compensated by the creation of macroporosity, so that the total porosity remains

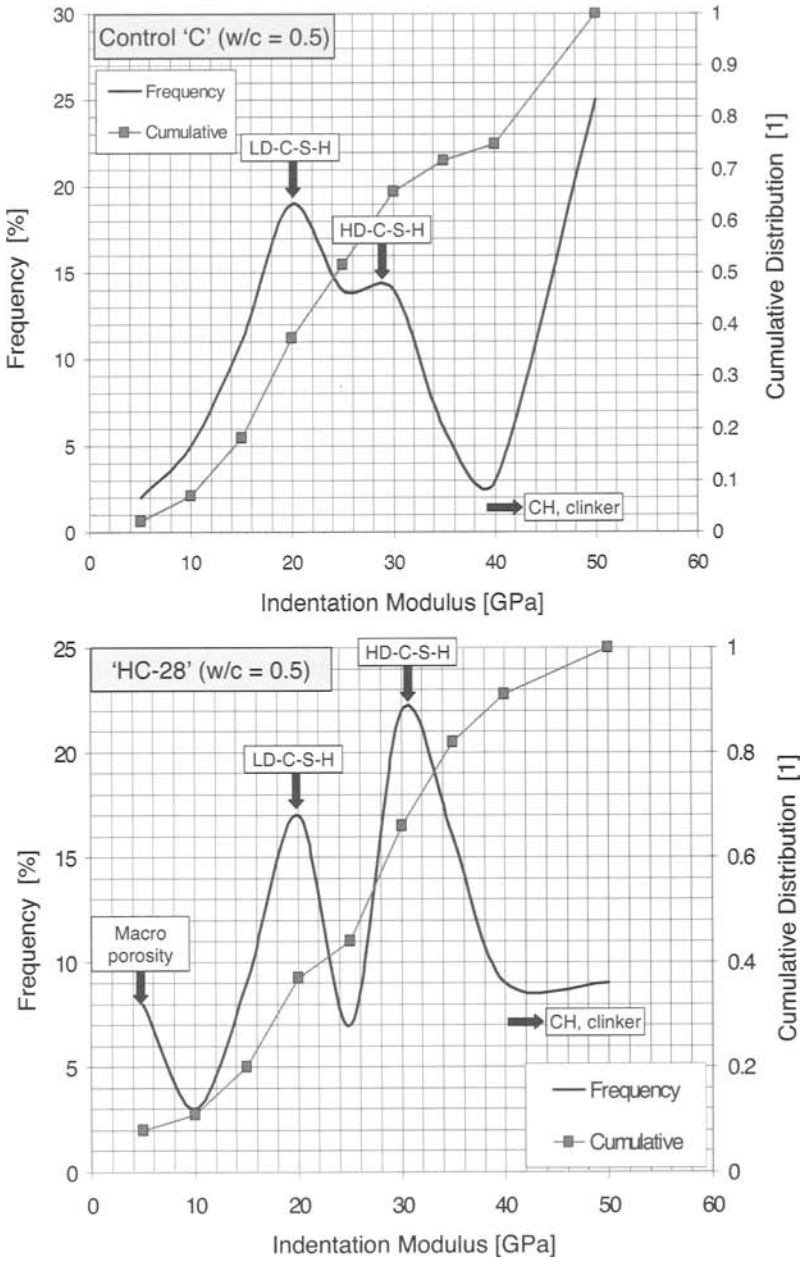

Figure 10. Frequency plot and cumulative distribution of indentation modulus determined by grid-nanoindentation: (top) control specimen (w/c=0.5) (No. of tests = 200); (bottom) heat cured specimen (No. of tests = 508).

		Control ('C')		HC-28	
		M [GPa]	Vol. Fr. [%]	M [GPa]	Vol. Fr. [%]
Level I	Macroporosity	≤ 5	2	≤ 5	8
	LD–C-S-H	20	55	20	33
	HD–C-S-H	29	30	31	45
	CH + Clinker	≥ 40	13	≥ 40	14
		μ [GPa]	σ/μ [%]	μ [GPa]	σ/μ [%]
Level I	LD–C-S-H, H	0.52	68	0.45	47
	HD–C-S-H, H	1.07	63	0.87	40
Level II	M^{II}_{exp}	19.1	9	19.5	25
	H^{II}_{exp}	0.50	2	0.41	4

Table 3. Summary of indentation results. The maximum *nano*indentation depth (level I) was 300nm, and the maximum *micro*indentation depth was 10μm.

almost constant.

Mechanical Mapping of Nanoindentation Results A second way of analyzing the nanoindentation test results consists in mapping the mechanical properties obtained on a grid of indentation tests. Each indentation result is assigned to a point on the grid that corresponds to the center of the indent. The discrete data points are linearly interpolated in between grid points to obtain continuous fields of mechanical properties, with a resolution defined by the grid-size of 10^{-5} m. The results are displayed on the $x-y$ plane in form of contour plots that capture ranges of mechanical properties. Based on the frequency plots and the values summarized in Table 3, we map the nanoindentation stiffness values into four domains:

1. Macroporosity domain $0-13$ GPa: Values situated in this range are associated with regions for which the mechanical response is dominated by high porosity. For purpose of comparison, these areas are indicative of the macroporosity.
2. Low-Density C-S-H domain $13-26$ GPa : Values situated in this range are situated around the first peak in the frequency plots 10, and are associated with regions in which the mechanical response is dominated by the LD–C-S-H (having a characteristic gel porosity at a scale below of 37%).
3. High-Density C-S-H domain $26-39$ GPa: Values situated in this range correspond to the second peak in the frequency plots 10, and are attributed to the dominant mechanical effect of the HD–C-S-H (having a characteristic gel porosity at a scale below of 24%).
4. Unhydrated clinker and CH domain ≥ 40 GPa: The higher stiffness values are indicative of unhydrated clinker phases and Portlandite. While the latter tends to grow in regions of high w/c ratios adjacent to macropores and in between LD–C-S-H, the residual clinker phases are generally rimmed by HD–C-S-H.

Figure 11 displays maps of 100 nanoindentation results for the control specimen and the 28-day heat cured specimen. The contour plots provide evidence of the creation of a new pore class and of a substantial change of percolation of the C-S-H phases as a consequence of the heat curing. Indeed, while almost absent in the control specimen 'C' (a single point in Fig. 11 represents rather a statistical event than a morphological pattern), the macroporosity domain becomes an identifiable morphological pattern in the map of the 28-days heat cured specimen , in which the macropores occupy regions several times the grid size of 10^{-5} m. Furthermore, in the control specimen, the continuous (percolated) solid phase appears to be the LD–C-S-H, which forms a matrix that accommodates residual clinker phase encapsulated into a rim of HD–C-S-H. By contrast, in the heat cured specimen, there is a larger proportion of HD–C-S-H present which tends to percolate throughout the microstructure, while the LD–C-S-H appears to be disconnect and situated around the large macropores. It almost appears as if the HD–C-S-H forms a continuous matrix that accommodates the macroporosity encapsulated into a rim of LD–C-S-H.

Nanohardness Measurements Figure 12 shows a log-log plot of the hardness vs. the stiffness. Besides showing a large scattering of the hardness values for a given indentation stiffness, the general trend is that the hardness increases as the stiffness increases. This correlation, however, should not be seen as a physical link between hardness and stiffness, but should be rather attributed to the fact that both stiffness and strength properties are affected by the microstructure[6]. The high scatter of the $H - M$ relation in Figure 12 highlights the sensitivity of the hardness w.r.t. the microstructure. The figure also displays fitted power functions for the tested specimen. The exponent of the power function is found to decrease as a result of heat curing: it is $H \propto M^{1.49}$ for the control specimen 'C', and $H \propto M^{1.28}$ for the 28-day heat cured specimen 'HC-28'. This power relation cannot be explained by the determination process, since the hardness scales with $H \sim A^{-1}$ and the indentation modulus with $M \sim A^{-1/2}$, so that any bias induced by application of relations (2.1) and (2.11) should be visible in a quadratic power relation, $H \sim M^2$. The hardness-stiffness scaling, therefore, should be rather of microstructural origin. In fact, since H/M is a constant for a homogeneous material (*ie.* relation (2.13)), the scaling $H \propto M^{\delta}$ is an expression of the heterogeneity of the material investigated by nanoindentation. It is higher for the control specimen ($\delta = 1.49$) than for the heat cured specimen ($\delta = 1.28$), which is an indication that heat-curing, on-average, 'homogenizes' the microstructure. This observation is consistent with the contour plots in Figure 11.

Using the stiffness values that characterize the LD–C-S-H domain ($E_{LD} \in [13, 26]$ GPa) and the HD–C-S-H domain ($E_{HD} \in [26, 39]$ GPa), we can determine the corresponding hardness values, representative of the two-types of C-S-H. Mean values and standard deviations are given in Table 3 for the LD–C-S-H phase and the HD–C-S-H

[6] We recall that the stiffness relates to the recovery (in form of deformation) of the elastic energy stored into the microstructure during loading; while the hardness relates to the irreversible dissipation of the external work during loading into heat form. In the absence of fracture processes, the only link that exists between the two quantities is the geometry and morphology of the microstructure.

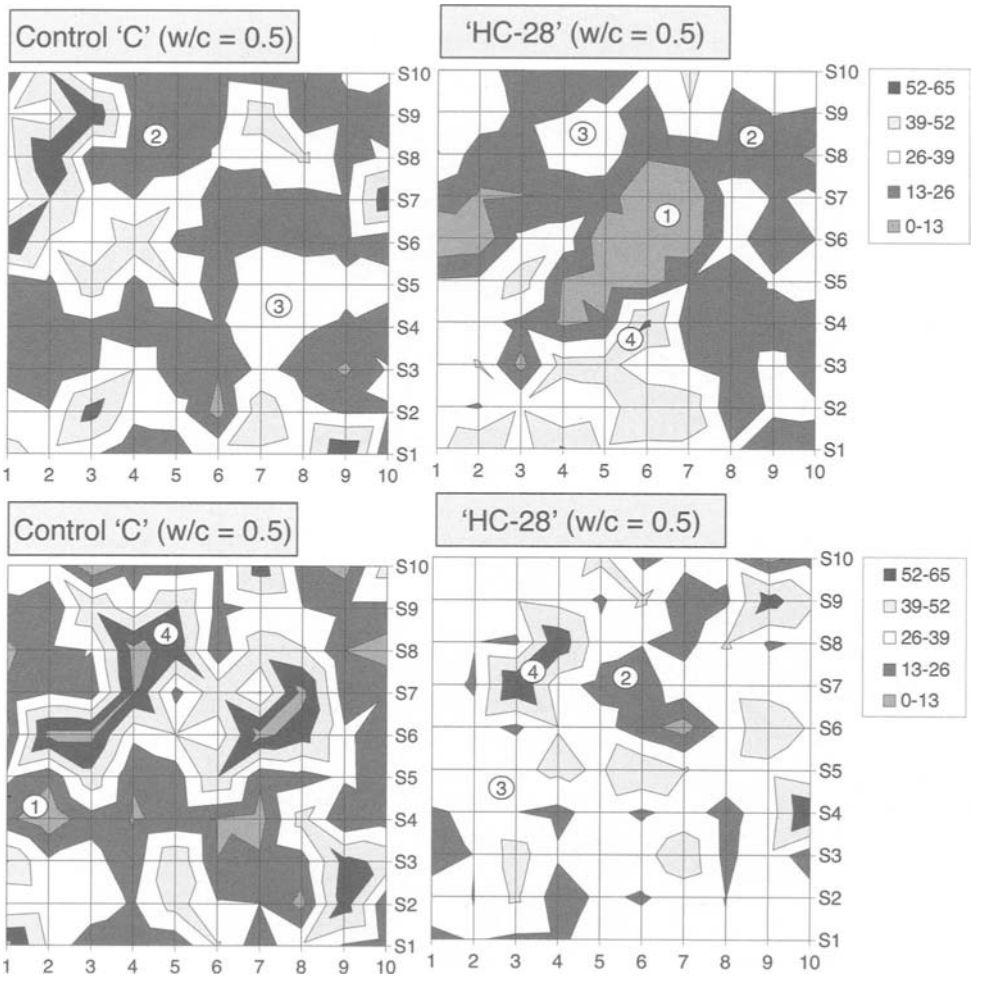

Figure 11. Contour plots of the spatial distribution of stiffness (in GPa) in the microstructure obtained by grid nanoindentation (grid-size = 10^{-5} m). Each grid point corresponds to a single nanoindentation test (unloading from a maximum indentation depth of 3×10^{-7} m). The numbers in the figure are attributed to 1 = porosity, 2 = LD-C-S-H, 3 = HD-C-S-H, 4 = CH and clinker phases.

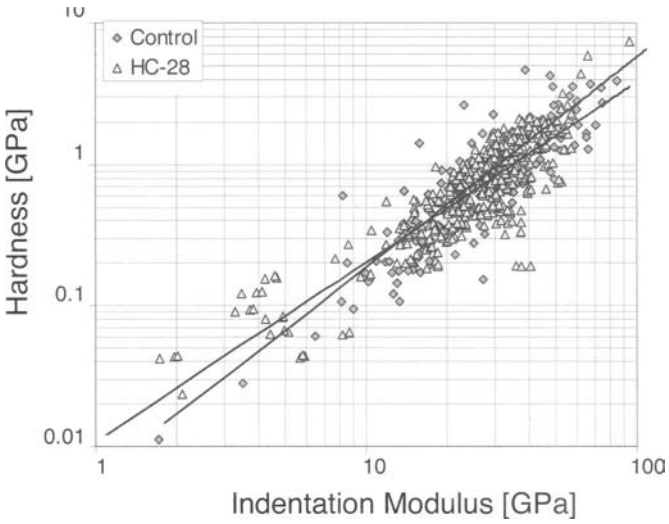

Figure 12. Hardness vs. indentation stiffness determined by nanoindentation.

phase. There is a trend that heat curing reduces the intrinsic hardness of the two C-S-H phases, as the hardness of the heat cured specimen is roughly 10% smaller than the one of the control specimen, and a hardness reduction by roughly 20% is found for the HD-C-S-H phase. On the other hand, this decrease is somewhat smaller than the standard deviation, so that it is difficult to conclude on the statistical significance of the heat-curing induced hardness drop. Two observations deserve particular attention: (1) The mean hardness values of the HD–C-S-H is roughly twice the value of the LD–C-S-H; and (2) the standard deviation, which can be seen as a measure of the microstructural disorder, reduces as a consequence of heat curing. Both observations are consistent with the disordered vs. ordered packing densities of the two types of C-S-H, or more precisely with the number of contacts that characterize the two types of packing densities. Indeed, it has been recently shown that the random packing of spheres which appears to characterize the LD–C-S-H, is characterized by on-average 6 points of contacts (Donev et al., 2004), while a high-density packing of spheres has a maximum of 12 points of contacts (Sloane, 1998), that is twice as much as the one in the random close-packed limit (RCP), which almost perfectly correlates with the measured nanohardness ratio $H_{HD}/H_{LD} \sim 2$. It is then not surprising that the overall scatter of the hardness values decreases as the amount of ordered HD–C-S-H increases in the material system. Rather than a coincidence, we see here a second evidence (in addition to the packing density) of the characteristic packing patterns of the LD–C-S-H and the HD–C-S-H. It suggests that the hardness (and thus the strength properties) of the two types of C-S-H is a mere consequence of the packing density, and more precisely of the number of contacts stabilizing

each solid sphere in the system. The higher the packing density and thus the number of contact points, the greater the number of degrees of freedom along which the system can dissipate energy at the limit state associated with strength, and which translates into the measured nanohardness values.

Microindentation Analysis To complete the analysis, we performed a series of *micro*indentation tests on the control specimen ('C') and the heat cured specimen ('HC-28'), with a maximum penetration depth of roughly 10^{-5} m. Table 3 summarizes the indentation results (level II), which are average values and standard deviation of respectively 10 indentation tests for the control specimen 'C', and 30 indentation tests for the 28-days heat cured specimen 'HC-28' (see Table 2). The higher number of indentation tests for the HC-28 sample was necessary because of a higher standard deviation of the elasticity, which is due to the large macropores that interfere at the micro-indentation scale of 10^{-5} m. While the mean values obtained for the control specimen allow an interpretation as characteristic properties of the homogenized material, *ie.* cement paste, given the size of the macropores generated in heat-cured specimen, a continuous interpretation should be handled with care. Nevertheless some interesting trends become apparent.

The elastic stiffness remains practically unaffected by heat curing, as the slight increase in mean value from 19.1 GPa for the control specimen 'C' to 19.5 GPa for 'HC-28' is smaller than the standard deviation. It appears that the two competing mechanisms that characterize the mechanical effect of heat curing at a scale below, that is the densification of the C-S-H matrix and the generation of a macroporosity, cancel each other out. In return, the higher standard deviation for heat cured specimens is indicative for a higher degree of disorder at level II, induced at a scale below by the creation of the macroporosity.

The hardness which is a measure of strength properties, decreases by roughly 20% as a consequence of heat curing. This decrease in strength performance of heat cured specimen seems to be a consequence of the macroporosity generation which is not compensated by the densification of the C-S-H matrix. This 'coarsening of the macroporosity', as it is often referred to in the literature (Bentur, 1980), leads to high stress concentrations in the C-S-H matrix, leading to a lower overall material strength, particular in high w/c ratio cement-based materials. Moreover, the microhardness is roughly on the same order of magnitude of nanohardness of the LD–C-S-H phase at a scale below. This may not be a coincidence. In fact, regarding the control specimen, with almost non-detectable macroporosity, the closeness of nano- and micro-hardness values would hint towards relevance of the weakest link theory, according to which the strength behavior is governed by the weakest phase in the material system, which is the LD–C-S-H phase, and which appears to dominate the strength behavior of the cement paste. A similar argument can be made for the 28-day heat-cured material ('HC-28'): the generation of the macroporosity leads to higher stress concentrations in the C-S-H matrix; and in particular in the LD-C-S-H surrounding the macropores (see Fig. 11), which therefore becomes dominant in the strength behavior of the cement paste. Finally, it is also worth mentioning that the scatter of the microhardness values, expressed by the standard deviation, reduces significantly compared to the nanoindentation results. The smaller scatter is a clear indication of the homogenized nature of the properties obtained by indentation at the

scale of the cement paste, but as well an indication that one detrimental phenomenon is at work governing the strength properties of the cement paste: the coarsening of the macroporosity.

3.3 Microporoelastic Analysis of Cement-Based Materials

Microporomechanics is a powerful framework to analyze and model indentation data, and ultimately to predict macroscopic material properties from the mere knowledge of some material independent phase properties, phase morphologies and volume fractions, determined either experimentally (e.g. nanoindentation and/or chemical analysis (Constantinides and Ulm, 2004)) or by modeling the physical chemistry processes that lead to the formation of the phases (see e.g. Bernard et al., 2003). Microporomechanics can start at the smallest scale, at which the composite material manifests itself composed of a continuous solid phase and a pore space that is large enough for water to be present as a bulk phase, characterized by a hydrostatic stress field, $\boldsymbol{\sigma} = -p\boldsymbol{\delta}$, where p is the fluid pressure. In the case of cement-based materials, this is the scale of the two-types of C-S-H (Ulm et al., 2004).

Level '0': Invariant Material Properties of C-S-H The information that is available about the two types of C-S-H are the porosities (3.1) determined by mass density measurements (see Table 1), and composite stiffness values determined independently by nanoindentation (see Table 3). The overall picture that emerges from a combination of these independent measurements is that the difference in mechanical performance of the two types of C-S-H is a consequence of their packing density, while the solid phase is the same, having the same mass density and as a consequence same mechanical properties. The poroelastic behavior of the two types of C-S-H is defined by the classical poroelastic state equations (Biot, 1941; Coussy, 1995; Coussy, 2004):

$$\Sigma_m = KE_v - bp;\ S_{ij} = 2GE^d_{ij} \tag{3.5a}$$

$$\phi - \phi_0 = bE_v + \frac{p}{N} \tag{3.5b}$$

where $\Sigma_m = \frac{1}{3}\Sigma_{ii}$ is the mean stress, $S_{ij} = \Sigma_{ii} - \Sigma_m\delta_{ij}$ is the stress deviator, $E_v = E_{ii}$ is the volume strain, and $E^d_{ij} = E_{ii} - \frac{1}{3}E_v\delta_{ij}$ is the strain deviator. Using standard relations of microporoelasticity (Chateau and Dormieux, 2002; Dormieux et al., 2002; Dormieux and Bourgeois, 2003; and the contribution of Dormieux in this book), the poroelastic

properties, K, G, b, N, are estimated from:[7]

$$K = g_s \frac{4(1-\phi_0)}{3\phi_0 + 4(g_s/k_s)} \tag{3.6a}$$

$$G = g_s \frac{(1-\phi_0)(8g_s+9k_s)}{6\phi_0(2g_s+k_s)+8g_s+9k_s} \tag{3.6b}$$

$$b = \phi_0 \frac{4g_s+3k_s}{3\phi_0 k_s + 4g_s} \tag{3.6c}$$

$$\frac{1}{N} = \frac{3\phi_0(1-\phi_0)}{3\phi_0 k_s + 4g_s} \tag{3.6d}$$

where k_s and g_s are the solid bulk modulus and the solid shear modulus. These nanomechanical properties are currently still out of reach to direct mechanical measurements; and that what is measured are the homogenized properties of the two types of C-S-H. The determination of the nanomechanical properties, therefore, can only be achieved by an inverse application of the homogenization relations. As input we have values for the indentation modulus, M_{HD} and M_{LD}, and for the porosity, ϕ_0^{LD} and ϕ_0^{HD}. The unknowns are the stiffness properties of the C-S-H solid phase, k_s and g_s, and one 'homogenized property' per type of C-S-H; e.g. the Poisson's ratio, ν_{HD} and ν_{LD}. This approach (Ulm et al., 2004) leads to identifying a solid bulk and shear modulus of $k_s = 32$ GPa, $g_s = 19$ GPa, which corresponds to a Young's modulus of $E_s \simeq 48$ GPa, a Poisson's ratio of $\nu_s = 0.25$, and a Biot coefficient of the C-S-H phases situated in between:

$$b_{HD}^0 = 0.61 \leq b \leq 0.71 = b_{LD}^0 \tag{3.7}$$

Level 'I': Poroelastic Properties of C-S-H Matrix – Double Porosity Model The C-S-H matrix is composed of two porous materials, the LD–C-S-H phase and the HD–C-S-H phase, each of which is described by poroelastic constitutive equations of the form (3.5). To derive the poroelastic constitutive equations of the C-S-H matrix, we adopt a continuous description of the stress field in the heterogeneous r.e.v.:

$$\text{in } V: \sigma_m(\underline{z}) = k(\underline{z})\,\epsilon(\underline{z}) + \sigma^p(\underline{z});\ s_{ij}(\underline{z}) = 2g(\underline{z})\,e_{ij}(\underline{z}) \tag{3.8}$$

together with the distributions of the elastic properties $(k(\underline{z}), g(\underline{z}))$ and the eigenstress $\sigma^p(\underline{z})$:

$$(k(\underline{z}), g(\underline{z})) = \begin{cases} (k_{LD}, g_{LD}) \text{ in } V_{LD} \\ (k_{HD}, g_{HD}) \text{ in } V_{HD} \end{cases} \quad \sigma^p(\underline{z}) = \begin{cases} -b_{LD}^0 p_1 \text{ in } V_{LD} \\ -b_{HD}^0 p_2 \text{ in } V_{HD} \end{cases} \tag{3.9}$$

where $\epsilon = \varepsilon_{ii}$ is the microscopic volume strain; and $e_{ij} = \varepsilon_{ij} - \frac{1}{3}\epsilon\delta_{ij}$ is the microscopic deviator strain. $(k_j, g_j), (j = LD, HD)$ are the elastic properties of the LD– and HD–C-S-H phases that occupy domains V_{LD} and V_{HD} in the r.e.v. For purpose of argument, we will assume that the fluids present within the two types of C-S-H are not at the same pressure.

[7] Relations (3.6) are the poroelastic constants that can be derived from the Hollow Sphere Model, or by application of a Mori-Tanaka scheme to an isotropic solid-porosity composite.

Following the linear microporomechanics approach (Dormieux and Bourgeois, 2003), we decompose the problem in two sub-problems:

1. The first sub-problem corresponds to overall drained conditions, for which $p_1 = p_2 = 0$. We assume that the r.e.v. is subjected to a uniform displacement boundary condition, so that the solid boundary conditions to which the solid phase is subjected read:

$$\text{on } \partial V \quad : \quad \underline{\xi}'(\underline{z}) = \mathbf{E} \cdot \underline{z} \tag{3.10a}$$

$$\text{on } \mathcal{I}_{sf} \quad : \quad \boldsymbol{\sigma} \cdot \underline{n} = 0 \tag{3.10b}$$

Here, ∂V stands for the boundary of the r.e.v., and $\mathcal{I}_{sf}$ represents the solid-fluid interfaces. $\underline{\xi}'(\underline{z})$ stands for the microscopic displacement field, and $\mathbf{E}$ is the macroscopic strain tensor, which is related to the microscopic strain by an isotropic strain localization condition:

$$\boldsymbol{\varepsilon}'(\underline{z}) = \mathbf{e}'(\underline{z}) + \frac{1}{3}\epsilon'(\underline{z})\,\boldsymbol{\delta} = a^d(\underline{z})\,\mathbf{E}_d + \frac{1}{3}a^v(\underline{z})\,E_v\boldsymbol{\delta} \tag{3.11}$$

where $a^d(\underline{z})$ and $a^v(\underline{z})$ are the deviator strain and the volumetric strain localization factors. Use in (3.8) together with the elastic distribution (3.9) yields after volume averaging the macroscopic stress:

$$\Sigma'_m = \overline{\sigma_m} = K^I E_v; \quad K^I = f_{LD}k_{LD}A^v_{LD} + f_{HD}k_{HD}A^v_{HD} \tag{3.12a}$$

$$\mathbf{S} = \bar{\mathbf{s}} = 2G^I\mathbf{E}_d; \quad G^I = f_{LD}g_M A^d_M + f_{HD}g_{HD}A^d_{HD} \tag{3.12b}$$

where $A^v_J = \langle a^v(\underline{z})\rangle_{V_J}$ and $A^d_J = \langle a^d(\underline{z})\rangle_{V_J}$ stand for volume averages of the localization factors over the C-S-H subdomains, and $f_J = V_J/V$ represent the volume fractions satisfying $f_{LD} + f_{HD} = 1$. On the other hand, the change of the gelporosity in the subproblem reads ($J = LD, HD$):

$$\left[(\phi - \phi_0)^I_J\right]' = f_J\left[(\phi - \phi_0)^0_J\right]' = b^I_J E_v \tag{3.13a}$$

$$b^I_J = f_J b^0_J A^v_J \tag{3.13b}$$

where superscript $0, I$ indicates the scale ('level') at which the quantity is defined. For instance, b^0_J stands for the Biot coefficients given by (3.7).

2. The second sub-problem we consider is the zero-displacement boundary problem, while the gelporosity is pressurized. From linear microporoelasticity, it is known that the problem is conveniently solved using Levine's theorem, delivering a relation between the macroscopic and the microscopic eigenstresses (Chateau and Dormieux, 2002; Dormieux et al., 2002; Dormieux and Bourgeois, 2003):

$$\boldsymbol{\Sigma}'' = \overline{\boldsymbol{\sigma}^p(\underline{z}) : \mathbb{A}(\underline{z})} \tag{3.14}$$

where $\mathbb{A}(\underline{z})$ is the forth-order strain localization tensor. Application of the eigenstress distribution (3.9) in (3.14) yields the macroscopic mean stress in this subproblem:

$$\Sigma''_m = -b^I_{LD}p_1 - b^I_{HD}p_2 \tag{3.15}$$

where we verify that $b^I_{LD} = f_{LD} b^0_{LD} A^v_{LD}$ and $b^I_{HD} = f_{HD} b^0_{HD} A^v_{HD}$ obtained in the first sub-problem (3.13) are the Biot coefficients associated with the pressures in gelporosity of the two type of C-S-H. Because the constitutive equation for the change of the porosity in each subdomain is given by (3.5b), the change of porosity reads:

$$\left[(\phi - \phi_0)^I_J\right]'' = f_J \left(b^0_J \langle \epsilon'' \rangle_{V_J} + \frac{p_J}{N^0_J} \right) \tag{3.16}$$

We need to eliminate $\langle \epsilon'' \rangle_{V_J}$ in (3.16). To this end, we determine the stress average in this sub-problem on account of (3.8) and (3.9):

$$\begin{aligned} \Sigma''_m &= f_{LD} \langle \sigma''_m \rangle_{V_{LD}} + f_{HD} \langle \sigma''_m \rangle_{V_{HD}} \\ &= f_{LD} k_{LD} \langle \epsilon'' \rangle_{V_{LD}} + f_{HD} k_{HD} \langle \epsilon'' \rangle_{V_{HD}} - f_{LD} b^0_{LD} p_1 - f_{HD} b^0_{HD} p_2 \end{aligned} \tag{3.17}$$

Then, we use (3.15) in (3.17) to express the average strain in the porous matrix $\langle \epsilon'' \rangle_{V_J}$ as a function of p_J:

$$\left(f_{LD} b^0_{LD} - b^I_{LD}\right) p_1 + \left(f_{HD} b^0_{HD} - b^I_{HD}\right) p_2 = f_{LD} k_{LD} \langle \epsilon'' \rangle_{V_{LD}} + f_{HD} k_{HD} \langle \epsilon'' \rangle_{V_{HD}} \tag{3.18}$$

which suggests, using (3.13) or (3.15):

$$\langle \epsilon'' \rangle_{V_J} = \frac{b^0_J}{k_J} \left(1 - A^v_J\right) p_J \tag{3.19}$$

with no summation on repeated subscripts. Finally, use of (3.19) in (3.16) yields:

$$\left[(\phi - \phi_0)^I_J\right]'' = \frac{p_J}{N^I_J}; \; \frac{1}{N^I_J} = \frac{f_J}{N^0_J} + f_J \frac{\left(b^0_J\right)^2}{k_J} \left(1 - A^v_J\right) \tag{3.20}$$

Last, a superposition of the two subproblems yields the macroscopic state equations of the C-S-H matrix:

$$\Sigma_m = \Sigma'_m + \Sigma_m{}'' = K^I E_v - b^I_{LD} p_1 - b^I_{HD} p_2 \tag{3.21a}$$

$$(\phi - \phi_0)^I_J = b^I_J E_v + \frac{p_J}{N^I_J}; \; J = LD, HD \tag{3.21b}$$

The resulting state equations are recognized as the state equations of a double-porosity material without interaction of the fluid pressures on the deformation of the solid part of the porous subdomains (*ie.* relation (3.19)). Given the similar size of the porosity in the LD- and HD-C-S-H, as defined by the packing densities, it can be suggested that there should be little difference in pressure in between the two types of C-S-H. In this case, the poroelastic state equations of the C-S-H matrix reduce to:

$$\Sigma_m = K^I E_v - b^I p \tag{3.22a}$$

$$(\phi - \phi_0)^I = b^I E_v + \frac{p}{N^I} \tag{3.22b}$$

and the poroelastic constants are given by:

$$K^I = f_{LD}k_{LD}A^v_{LD} + f_{HD}k_{HD}A^v_{HD} \tag{3.23a}$$

$$b^I = b^I_{LD} + b^I_{HD} = f_{LD}b^0_{LD}A^v_{LD} + f_{HD}b^0_{HD}A^v_{HD} \tag{3.23b}$$

$$\frac{1}{N^I} = \frac{1}{N^I_{LD}} + \frac{1}{N^I_{HD}} \tag{3.23c}$$

Level 'II': Poroelastic Properties of Cement Paste – Two-Scale Double Porosity Model Let us turn now to cement paste: a composite of a porous C-S-H matrix and macroporosity, in addition to some inclusion phases (residual clinker, Portlandite). In contrast to the C-S-H matrix (level I), the main feature here at level II is that the porosity manifests itself at two different scales, a microporosity situated within the porous matrix and the macroporosity. We want to derive the poroelastic state equations of the cement paste. For purpose of clarity, we set any additional inclusion phases aside (see Ulm et al. (2004) for an account of multiple solid phases), and restrict ourselves, for a microporoelastic analysis, to a porous matrix and a macroporosity. The constitutive equations of the porous matrix are assumed to be defined by (3.22). Given the difference in size of the porosities involved, we assume a different pressure in the micro- and macroporosity.

Proceeding as before, we adopt a continuous description of the stress field in the heterogeneous r.e.v., of the form (3.8), together with the following distributions of the elastic properties $(k(\underline{z}), g(\underline{z}))$ and the eigenstress $\sigma^p(\underline{z})$:

$$(k(\underline{z}), g(\underline{z})) = \begin{cases} (K^I, G^I) \text{ in } V_M \\ (0,0) \text{ in } V_{\phi 2} \end{cases} \quad \sigma^p(\underline{z}) = \begin{cases} -b^I p_1 \text{ in } V_M \\ -p_2 \text{ in } V_{\phi 2} \end{cases} \tag{3.24}$$

where V_M stands for the volume occupied by the porous matrix in the r.e.v., and $V_{\phi 2}$ for the macroscopic pore space. We decompose the problem in (the meanwhile classical) two sub-problems:

1. The first sub-problem corresponds to overall drained conditions, for which $p_1 = p_2 = 0$. The boundary conditions are still defined by (3.10), and an isotropic strain localization condition of the form (3.11) is applied. This yields after volume averaging the macroscopic stress in the form:

$$\Sigma'_m = K^{II}E_v; \quad K^{II} = (1-\phi_{02})\,K^I A^v_M \tag{3.25a}$$

$$\mathbf{S} = 2G^{II}\mathbf{E}_d; \quad G^{II} = (1-\phi_{02})\,G^I A^d_M \tag{3.25b}$$

where $A^v_M = \langle a^v(\underline{z})\rangle_{V_M}$ and $A^d_M = \langle a^d(\underline{z})\rangle_{V_M}$; $1-\phi_{02} = V_M/V$ is the volume fraction of the porous matrix in the r.e.v. K^{II} and G^{II} are recognized as the macroscopic drained elastic stiffness properties of the cement paste. On the other hand, there are two associated changes of porosity; the microporosity and the macroporosity. The microporosity is defined per unit of (undeformed) matrix volume V_M so that the change of porosity at the macroscale in the considered subproblem

is:

$$\left[(\phi_1 - \phi_{01})^{II}\right]' = (1-\phi_{02})\left[(\phi_1 - \phi_{01})^{I}\right]' = b_1^{II} E_v \tag{3.26a}$$

$$b_1^{II} = (1-\phi_{02})\, b^I A_M^v \tag{3.26b}$$

In return, the change in macroporosity reads:

$$\left[(\phi_2 - \phi_{02})^{II}\right]' = b_2^{II} E_v \tag{3.27a}$$

$$b_2^{II} = \phi_{02} A_{\phi 2}^v \tag{3.27b}$$

where $A_{\phi 2}^v = \langle a^v(\underline{z})\rangle_{V_{\phi 2}}$. Herein, b_1^{II} and b_2^{II} are the Biot coefficients associated with the micro- and the macroporosity, respectively.

2. The second sub-problem we consider is the zero-displacement boundary problem, for which Levine's theorem (3.14) applies. Application of the eigenstress distribution (3.24) in (3.14) yields the macroscopic stress in this subproblem:

$$\Sigma_m'' = -(1-\phi_{02})\, b^I A_M^v\, p_1 - \phi_{02} A_{\phi 2}^v p_2 = -b_1^{II} p_1 - b_2^{II} p_2 \tag{3.28}$$

There are two changes of porosity to be considered; the change in microporosity,

$$\left[(\phi_1 - \phi_{01})^{II}\right]'' = (1-\phi_{02})\left(b_M \langle \epsilon'' \rangle_{V_M} + \frac{p_1}{N^I}\right) \tag{3.29}$$

and the change in macroporosity:

$$\left[(\phi_2 - \phi_{02})^{II}\right]'' = \phi_{02} \langle \epsilon'' \rangle_{V_{\phi 2}} = -(1-\phi_{02}) \langle \epsilon'' \rangle_{V_M} \tag{3.30}$$

We need to eliminate $\langle \epsilon'' \rangle_{V_M}$ in (3.29) and (3.30). To this end, we determine the stress average in this sub-problem on account of (3.24):

$$\begin{aligned} \Sigma_m'' &= (1-\phi_{02}) \langle \sigma_m'' \rangle_{V_M} + \phi_{02} \langle \sigma_m'' \rangle_{V_{p2}} \\ &= (1-\phi_{02}) K^I \langle \epsilon'' \rangle_{V_M} - (1-\phi_{02})\, b^I p_1 - \phi_{02} p_2 \end{aligned} \tag{3.31}$$

Then, we use (3.28) in (3.31) to express the average strain in the porous matrix $\langle \epsilon'' \rangle_{V_M}$ as a function of p_1 and p_2:

$$\begin{aligned} (1-\phi_{02}) \langle \epsilon'' \rangle_{V_M} &= \frac{1}{K^I}\left[\Sigma_m'' + (1-\phi_{02})\, b^I p_1 + \phi_{02} p_2\right] \\ &= \frac{1}{K^I}\left[\left((1-\phi_{02})\, b^I - b_1^{II}\right) p_1 + \left(\phi_{02} - b_2^{II}\right) p_2\right] \end{aligned} \tag{3.32}$$

Finally, substitution in (3.29) and (3.30) yields the change of the microporosity:

$$(\phi_1 - \phi_{01})'' = \frac{p_1}{N_{11}} + \frac{p_2}{N_{12}} \tag{3.33a}$$

$$\frac{1}{N_{11}} = (1-\phi_{02})\left(\frac{b^I}{K^I}\left(b^I - b_1^{II}\right) + \frac{1}{N^I}\right) \tag{3.33b}$$

$$\frac{1}{N_{12}} = \frac{b^I}{K^I}\left(\phi_{02} - b_1^{II}\right) \tag{3.33c}$$

and the change of the macroporosity:

$$(\phi_2 - \phi_{02})'' = \frac{p_1}{N_{21}} + \frac{p_2}{N_{22}} \tag{3.34a}$$

$$\frac{1}{N_{21}} = \frac{1}{K^I}\left(b_1^{II} - (1-\phi_{02})\, b^I\right) \tag{3.34b}$$

$$\frac{1}{N_{22}} = \frac{1}{K^I}\left(b_2^{II} - \phi_{02}\right) \tag{3.34c}$$

The symmetry of the skeleton Biot moduli $N_{12} = N_{21}$ is readily shown, by substituting (3.27b) in (3.33c) and (3.26b) in (3.33b):

$$\frac{1}{N_{12}} = \phi_{02}\frac{b^I}{K^I}\left(1 - A^v_{\phi 2}\right) \tag{3.35a}$$

$$\frac{1}{N_{21}} = (1-\phi_{02})\frac{b^I}{K^I}\left(A^v_M - 1\right) \tag{3.35b}$$

Then, use of the strain localization compatibility condition in one of the two relations yields the other one. For instance, replacing $\phi_{02}A^v_{\phi 2} = 1 - (1-\phi_{02})\, A^v_M$ in (3.35a) gives:

$$\frac{1}{N_{12}} = (1-\phi_{02})\frac{b^I}{K^I}\left(A^v_M - 1\right) = \frac{1}{N_{21}} \tag{3.36}$$

Last, a superposition of the two subproblems yields the macroscopic state equations of the isotropic double-porosity system:

$$\Sigma_m = \Sigma_m' + \Sigma_m'' = K^{II}E_v - b_1^{II}p_1 - b_2^{II}p_2 \tag{3.37a}$$

$$\phi_1 - \phi_{01} = b_1^{II}E_v + \frac{p_1}{N_{11}} + \frac{p_2}{N_{12}} \tag{3.37b}$$

$$\phi_2 - \phi_{02} = b_2^{II}E_v + \frac{p_1}{N_{21}} + \frac{p_2}{N_{22}} \tag{3.37c}$$

where all seven poroelastic constants are known here as functions of the poroelastic properties of the porous matrix, and of two strain localization factors, $A^v_{\phi 2}$ (or A^v_M) and A^d_M. An estimate of these factors provided e.g. by a Mori-Tanaka scheme reads:

$$A^v_{\phi 2} = \frac{4G^I + 3K^I}{3\phi_{02}K^I + 4G^I};\quad A^v_M = \frac{1 - \phi_{02}A^v_{\phi 2}}{1-\phi_{02}} \tag{3.38a}$$

$$A^d_M = \frac{1 - \phi_{02}A^d_{\phi 2}}{1-\phi_{02}} = \frac{8G^I + 9K^I}{6\phi_0\left(2G^I + K^I\right) + 8G^I + 9K^I} \tag{3.38b}$$

For purpose of comparison of the poroelastic properties, it is useful to evaluate the poroelastic constants for the same pressure in both meso- and macroporosity, for which the state equations are given by (3.5), with:

$$b^{II} = b_1^{II} + b_2^{II} = b^I + \left(1 - b^I\right)\phi_{02}A^v_{\phi 2} \tag{3.39a}$$

$$\frac{1}{N^{II}} = \frac{1}{N_{11}} + \frac{2}{N_{12}} + \frac{1}{N_{22}} \tag{3.39b}$$

Summary of Microporoelastic Analysis The poroelastic analysis of cement-based materials at different scales illustrates the important role of microporoelasticity theory in the understanding and assessment of material properties at different scales of cement-based materials. Table 4 summarizes the poroelastic properties of the $w/c = 0.5$ control specimen and thermally cured specimen, determined from the presented theory. The error of the prediction of the Young's modulus is smaller than the standard deviation of the microindentation results. The input to the analysis are the indentation stiffness and the volume fractions determined by nanoindentation:

- Level '0': On very small scales of cement-based materials, a combination of nanoindentation results and microporomechanics provides a means to determine material invariant mechanical properties, that are readily employed as a starting point for the application of microporomechanics theory. From a materials science point of view, cement-based materials, at this scale, are organized in two characteristic packing features, leaving a pore space behind that is at the origin of the pronounced porous material behavior of cement-based materials at larger scales.

- Level I: The C-S-H matrix manifests itself, from a poromechanics point of view, as a double porosity material system, one representing the LD–C-S-H phase, the other the HD–C-S-H phase. At this scale, the poroelastic properties depend on the relative proportion of the LD– and HD–C-S-H phase present, which depends on the mix proportions, curing conditions, and so on. It is not surprising that thermal curing which increases the amount of HD-C-S-H on the expenses of LD–C-S-H yields a higher stiffness of the C-S-H matrix, and a (slightly) lower Biot coefficient.

- Level II: Cement paste is a double porosity material system as a consequence of the porosity at (at least) two different scales; the mesoporosity in the C-S-H matrix, and the macroporosity. Despite an increase of the stiffness of the C-S-H matrix due to heat curing, it is found that stiffness of the cement paste is almost the same for both control specimen and thermally cured specimen. Microporoelastic theory thus confirms that the stiffening of the C-S-H phase is compensated by the macroporosity generation in its overall effect on the (drained) elasticity of heat cured materials. As a result of the macroporosity generation, the Biot coefficient increases.

		Control ('C')		HC-28	
		E_{hom} [GPa]	b_{hom} [1]	E_{hom} [GPa]	b_{hom} [1]
Level 0	LD–C-S-H	18.8	0.71	18.8	0.71
	HD–C-S-H	27.3	0.61	29.2	0.61
Level I	C-S-H Matrix	21.5	0.68	24.2	0.66
Level II	Cement Paste	20.5	0.70	20.2	0.72
Error	$1 - E_{\text{hom}}/E_{\text{exp}}^{II}$	−7%	–	−3.5%	–

Table 4. Summary of microporoelastic analysis. The input are experimentally determined nanoindentation stiffness and volume fractions from Table 3. The assumed Poisson's ratio for the LD– and HD–C-S-H is 0.24.

4 Experimental Microporomechanics of Shales

Is shale anisotropy a consequence of the intrinsic anisotropy of the clay minerals or rather an effect of texture, or both?[8] –

Shales are probably one of the most complicated and intriguing natural materials present on earth. Shales make up about 75% of sedimentary basins (Jones and Wang, 1981) and cover many hydrocarbon-bearing reservoirs. Knowing and predicting the anisotropy plays a critical role in many fields of exploitation, ranging from seismic exploration (log-data interpretation), to well drilling (well bore stability) and production (Thomsen, 2001). But the properties of shales are still an enigma that has deceived many decoding attempts from experimental or theoretical sides. Two schools of thought exist:

- The shale geomechanics school of thought, which is based on observational techniques, such as Scanning Electron Microscopy (SEM), Environmental Scanning Electron Microscopy (ESEM), Transmission Electron Microscopy (TEM), etc., considers the elastic anisotropy as a result of the microfabric signature of clay that originates from physicochemical, electrochemical, thermomechanical, interface dynamics, bioorganic and, most importantly, burial diagenesis processes (Bennett et al., 1991; Mitchell, 1993).
- The basis of a second school of thought is the existence of the 'perfect' shale, a concept introduced in a 1994 paper by Hornby et al. (1994), and which has found strong support particularly in the shale acoustics community (Jacobsen et al., 2003). The origin of anisotropy, in this concept, is attributed to a perfect alignment of shale particles at very small scales, that is eventually disturbed at larger scales

[8] The investigation of the sources of anisotropy of shale materials was suggested to us by Prof. Younane Abousleiman (Oklahoma Uinversity) and was carried out in a collaborative research effort between MIT, the Poromechanics Institute at Oklahoma University at Norman, and the Chevron Texaco team led by Dr. Russ Ewy. The financial support of the study by Chevron Texaco is gratefully acknowledged. The investigated shale specimens, mineralogy, porosity and UPV measurements were provided by the Chevron Texaco team, Drs. Russ Ewy, Luca Duranti, Douglas K. McCarty, whose collaboration, comments and suggestions were critical in this multidisciplinary project.

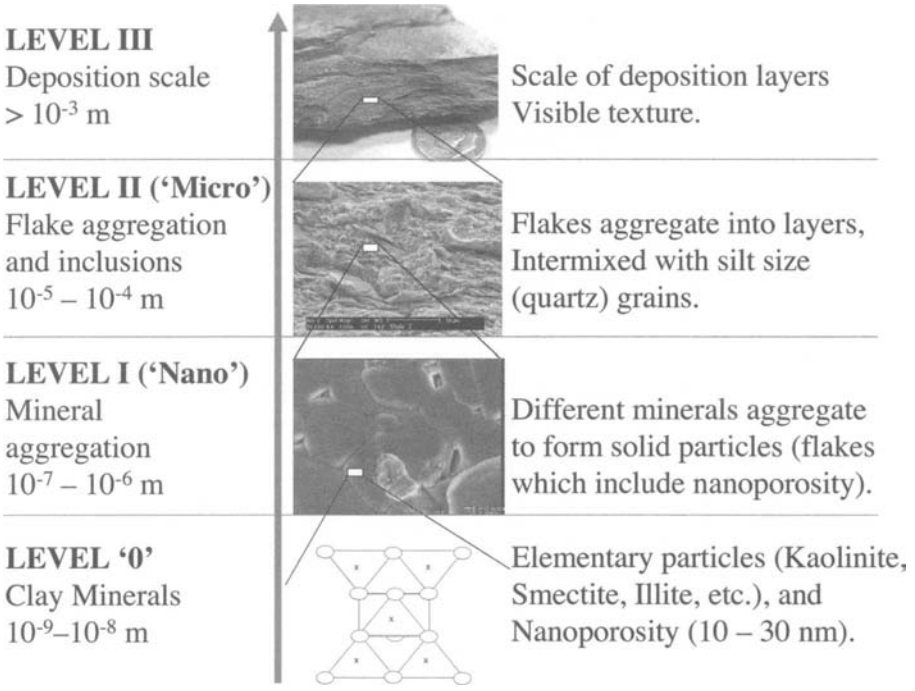

Figure 13. Four-level microstructural think-model of shale materials.

through a partially oriented distribution of clay minerals (Sayers, 1994; Johansen et al., 2004), and by the presence of (almost spherical) silt inclusions that reduce the intrinsic anisotropy of shale materials.

Shale anisotropy is a formidable play ground for an experimental microporomechanics approach, combining nanoindentation with advanced microporoelasticity theory (Delafargue and Ulm, 2004b).

4.1 Multiscale Indentation Analysis of Shale Materials

Inarguably, shale materials are highly heterogeneous multiphase natural composite materials. Figure 13 displays the four-level think model of the multiscale structure of shale materials, which forms much of the backbone of our experimental and theoretical microporomechanics approach.

Level '0': Scale of Elementary Particles The lowest level we consider is the scale of the elementary clay particles at a length scale of some nanometer. This scale has been focus of much research in clay mineralogy; and it is now well known (Velde, 1993), from both XRD-analysis and high resolution TEM-images, that the clay crystals (kaolonite,

illite, smectite, etc.) form platelets with typical aspect ratios of 1/20.

However, unlike many other minerals, clay stiffness values are extremely rare in handbooks (Mavko et al., 1998). To our knowledge, the only direct measurements of the anisotropic elasticity of clay minerals were reported for large muscovite crystals, possessing transversely isotropy: $C_{11} = 178$ GPa, $C_{33} = 55$ GPa, $C_{44} = 12$ GPa, $C_{12} = 42$ GPa, $C_{13} = 15$ GPa, or equivalently expressed in terms of indentation stiffness (2.44) and (2.52),

$$M^0_{1,\text{exp}} = 118 \text{ GPa}; \; M^0_{3,\text{exp}} = 46 \text{ GPa}; \; \frac{M^0_{1,\text{exp}}}{M^0_{3,\text{exp}}} = 2.6 \tag{4.40}$$

The main difficulty of measuring the mineral elasticity stems from the fact that clay particles are too small to be tested in pure solid form. Several attempts to overcome this difficulty have been reported (Table 5):

- The stiffness of compacted clay samples has been measured and extrapolated to a zero porosity assuming that this extrapolation technique yields a 'pure clay' stiffness value (Marion et al., 1992; Hornby et al., 1994; Vanorio et al., 2003). There is quite some difference in stiffness values obtained with this technique, which makes it difficult to state with certainty whether such extrapolation techniques give access to intrinsic stiffness values or not. In particular, depending on the degree of saturation of the sample and other parameters influencing surface forces, the interactions between clay particles might exhibit different compliances which may in turn modify the extrapolated stiffness value. In order to have relevant experimental measures of clay minerals stiffness, Prasad et al. (2002) have recently made some dynamic measurement of clays using Atomic Force Acoustic Microscopy (AFAM). They reported a very low Young's modulus for dickite of 6.2 GPa.
- Ultrasonic velocities of composite mixture of individual clay particles (powder) diluted, at various concentrations, in an epoxy matrix have been measured (Wang et al., 2001). Using a backward homogenization derivation, the Young's modulus for randomly distributed clay particles was found to be on the order of $50 - 60$ GPa for Kaolonite, $65 - 80$ GPa for illite, $40 - 50$ GPa for montmorillonite, and greater than 100 GPa for Chlorite. These results appear to be very consistent with theoretical estimates of single crystal elastic properties by Katahara (1996) for kaolonite, illite and chlorite, based on data of Alexandrov and Ryzhova (1961; cited from Wang et al. (2001)).
- Very recently, Steered Molecular Dynamics simulations of pyrophyllite clay provided an order of magnitude of the interlayer stiffness of 130 GPa, while the clay layers are almost rigid (Katti et al., 2003), with a stiffness value of 547 GPa in the direction perpendicular to crystal planes for a simple structure of two crystal layers with an interlayer space.

The scarcity of experimental values for solid clay stiffness and the large range of reported values highlight the difficulty to assess the intrinsic elasticity of single clay crystals. This has been recognized as one current major weakness of existing micromechanical models of shales (Jacobsen et al., 2003). We performed some nanoindentation tests on

a kaolin powder composed of 97% kaolonite (EPK Kaolin[9], Feldspar Corporation, Atlanta Georgia) having an average particle size of 1.36×10^{-6} m, a specific surface area of $24.25\,\mathrm{m}^2/\mathrm{g}$, and a loose (dense) mass density of $519 - 740\,\mathrm{kg}/\mathrm{m}^3$. Using indentation depths of $70 - 90$ nm, that is an order of length magnitude smaller than the grain size, we obtain indentation stiffness values of

$$\text{EPK Kaolin: } M^0_{\text{exp}} = 40.3 \pm 8.8 \text{ GPa} \tag{4.41}$$

Figure 14 displays an Atomic Force Microscopy image of a kaolin powder grain on which we indented, together with five force–indentation depth curves, from which we determine, from the unloading branch, the indentation stiffness. The order of magnitude of the indentation stiffness of kaolin powder is found to be situated in between the values reported by Marion et al. (1992) and Wang et al. (2001), respectively; and on the order of the weak axis indentation stiffness of Muscovite (see Table 5).

Level 'I': Porous Clay Composite Clay particles with nanoporosity form a porous clay composite at a characteristic length scale in the hundreds of nanometer range. ESEM images (Fig. 15) of the porous clay composite reveal that the porous clay composite in shale materials comes in a large variety of forms and shapes, ranging from highly ordered sheet bundles to wavy flake structures and highly pressed and crushed structure of clay sheets. The characteristic dimension of the clay sheets visible in these pictures is on the order of $500 - 1000$ nm, and $20 - 50$ nm thick, which confirms the aspect ratio of roughly $1/25 - 1/20$, as generally admitted in the clay literature. However, the microphotographs in figures 15 also display a high degree of disorder of the clay sheet orientation, and this both normal to the bedding direction (labeled '$x3$') and in bedding direction (labeled '$x1$' or '$x2$'). At the considered scale of the porous clay composite, it is quite frequent that clay packages are found to strongly divert from the deposition orientation.

Furthermore, the space in between the clay sheets forms almost the totality of the porosity of shales, as poromercury intrusion studies show, displaying a very low characteristic pore access radius[10] of some nanometers; thus situating the porosity of shales at a scale below the porous clay composite. This justifies considering shales at a length scale of $500 - 5,000$ nm as porous composites. This is level 'I' of shale materials, *ie.* the lowest scale currently accessible to mechanical testing. Prasad et al. (2002) used atomic force acoustic microscopy (AFAM) to determine the Young's modulus of a thin layer of dickite to be on the order of 6.2 GPa. The authors concluded from this and a subsequent study (Vanorio et al., 2003), in which $P-$ and $S-$ wave velocity measurements on cold-pressed clay aggregates of different porosity/grain density were extrapolated to zero porosity values, that the actual stiffness of clay crystals was on the order of $10 - 15$ GPa, which is

[9] For detailed chemical and mineralogy information on EPK Kaolin, see http://www.feldspar.com/minerals/epk.html.

[10] The poromercury intrusion model is based on a pore cylinder model, and it is generally admitted that MPI allows invasion of (cylindrical) pores of pore radius 3.6×10^{-9} m to 60×10^{-6} m. Given the sheet shape of the clay particles, it is most unlikely that the pores in shales are cylindrical, as the porosity is the space in between the sheets, so that the pore geometry should be similar to the sheet geometry.

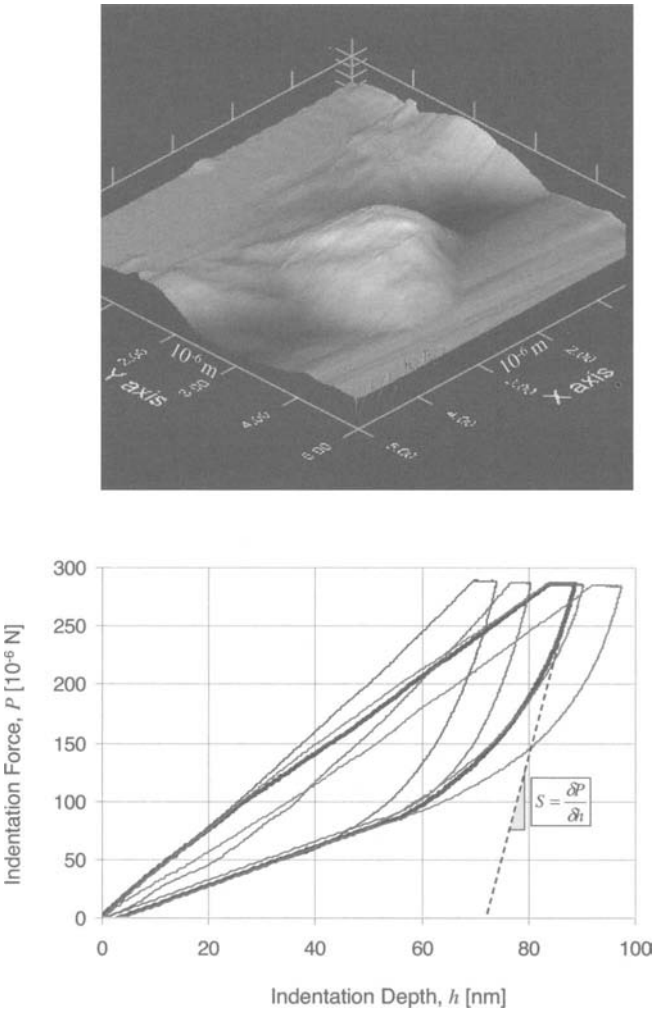

Figure 14. Nanoindentation on kaolin powder: (top) AFM image; (bottom) load-displacement curves.

Clay Mineral	Sample	Experim. Techn.	Stiffness [GPa] $M^0_{1,\text{exp}}$	$M^0_{3,\text{exp}}$	Source
Muscovite	nat. crystal		118.1	46.2	Mavko et al., 1998
Kaolinite	clay mixture	acoustic (MicroMech)	30.3		Marion et al., 1992 Hornby et al., 1994
Dicktite	clay mixture	AFAM	$E = 6.2$		Prasad et al., 2002
Kaolinite Smectite Montmorillonite	clay-mixture suspensions	acoustic (Extrapol.)	10.4 – 16.8		Vanorio et al, 2003
Kaolinite	powder	acoustic	57.9 – 85.9		Wang et al., 2001
Illite	in epoxy	(MicroMech)	73.9 – 84.3		Wang et al., 2001
Smectite/Illite			51.5		Wang et al., 2001
Montmorillonite			44.7 – 54.5		Wang et al., 2001
Chlorite			82.2 – 214.0		Wang et al., 2001
Pyrophyllite	–	Mol. Dyn.	weak axis	547	Katti et al., 2003
		$\Sigma/(\Delta L/L)$	interlayer	130	Katti et al., 2003

Table 5. Reported elastic stiffness values of clay minerals. For purpose of comparison, values are expressed, if possible, as indentation stiffness.

much smaller than typical values reported previously. Given the inarguably small size of the porosity of clay materials, which is a consequence of the packing density, and our confirmation of the clay crystal stiffness by nanoindentation (*ie.* Eq. (4.41) and Fig. 14), it appears to us very likely that the reported values by Prasad et al. (2002) are those of the porous clay composite rather than the ones of the clay crystals themselves! Clear evidence is provided by nanoindentation on shale materials:

Table 6 reports the indentation results on three types of shale materials of different mineralogy and porosities. The shale materials are labeled 1,2 and 3, 'N' respectively 'M' stands for respectively nanoindentation and microindentation test, and 'xi (i=1,2,3)' stands for the indentation axis. Each series of tests consist of a hundred force driven indentation tests performed on a grid of 50 μm grid size. The maximum indentation depth in the nanoindentation tests is on the order of 150 – 400 nm, and the derived properties, therefore, should be representative of a bulk material size on the order of 1,000 nm. This is the scale of the porous clay composite at level I, that includes the inter-grain clay porosity. We remark that the order of magnitude of the average nanoindentation stiffness is in deed on the same order of magnitude as the values reported by Vanorio et al. (2003):

$$M^I_{\text{exp}} = 8 - 14 \text{ GPa} \tag{4.42}$$

Moreover, depending on the specific shale material, there are some anisotropy effects present. Quantified in terms of the indentation stiffness ratio, we find that the anisotropy ratio of the three materials at level I is roughly half the value of the clay minerals:

$$\frac{M^I_{1,\text{exp}}}{M^I_{3,\text{exp}}} = 1.06 - 1.46 - 1.16 \tag{4.43}$$

Three particular experimental observation deserve attention:

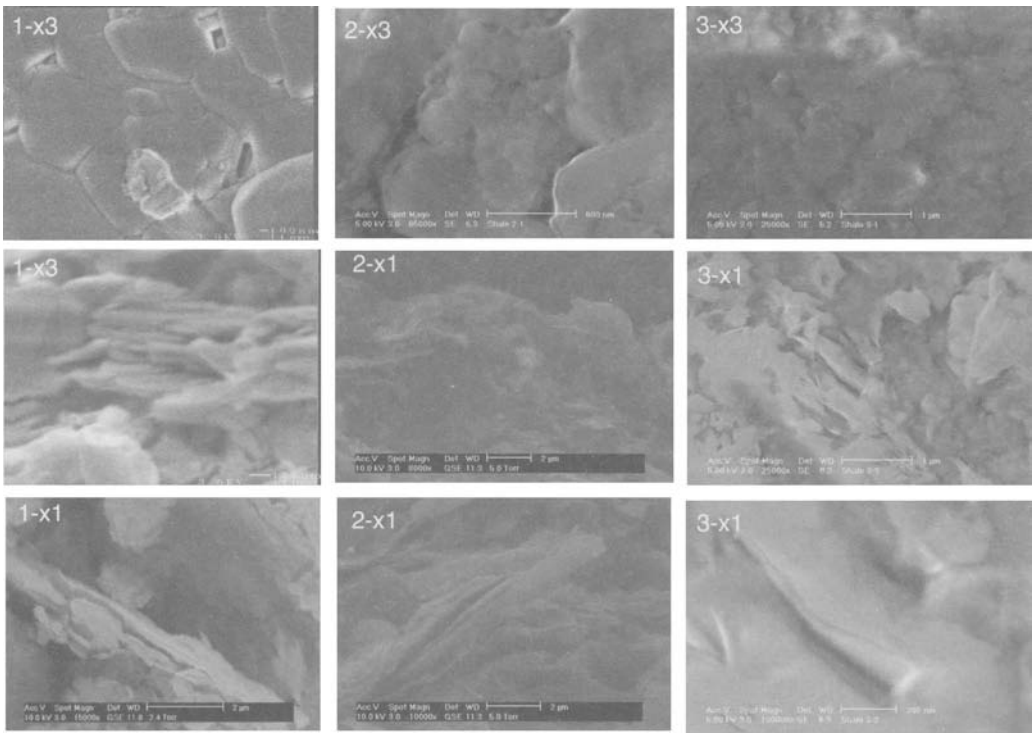

Figure 15. SEM and ESEM images of three shale materials, viewed normal to the deposition direction (x3) and in the deposition plane (x1 and x2).

1. What is sensed in a force driven indentation test on natural composites, is the highly heterogeneous nature of such materials, which translates into a stiffness scaling relation as a result of the BASh equation (2.11), as shown in Figure 16 for the three shale materials. While the mean value of the indentation stiffness shows some anisotropy feature, the continuity of the scaling relation for different indentation directions is an indication that the same material is present –on-average– in different indentation directions.
2. The maps of the nanoindentation stiffness values for different indentation directions (Figure 17) display a highly heterogeneous spatial distribution. There is no visible morphology at the grid size scale of 50 μm that could explain the (small but existing) anisotropy of the average stiffness values obtained at level I.
3. There is some difference in frequency distribution of the stiffness values obtained by grid indentation on different material planes, as shown in Figure 18. Recalling that the same distribution in different indentation directions is a condition for isotropy, we recognize that it is the frequency distribution which is at the origin of the observed anisotropy of shale materials at a nanoscale.

Shale #	Scale (Level)	Name #–N/M–dir	$P_{\max}$ [μN]		$h_{\max}$ [nm]		M [GPa]	
			σ	μ	σ	μ	σ	μ
1	Nano (I)	1-N-x3	262	21	230	61	9.5	3.1
	$\phi^I = 0.31$	1-N-x1	256	18	275	109	10.1	5.4
	Micro (II)	1-M-x3	12,348	111	2,183	618	6.9	2.5
	$\phi^{II} = 0.31$	1-M-x1	12,363	98	2,252	533	9.5	2.7
		1-M-x2	12,332	96	2,310	593	9.4	3.0
	Macro (III)	1-UPV-x3	–	–	–	–	10.9	NaN
	$\phi^{III} = 0.26$	1-UPV-x1	–	–	–	–	14.7	NaN
2	Nano (I)	2-N-x3(1)	257	17	270	100	9.7	4.3
	$\phi^I = 0.18$	2-N-x3(2)	251	18	302	107	8.0	4.3
		2-N-x1	265	12	219	70	14.2	5.5
	Micro (II)	2-M-x3	12,305	70	1,947	396	8.0	1.9
	$\phi^{II} = 0.18$	2-M-x1	12,206	31	1,414	194	15.0	2.8
	Macro (III)	2-UPV-x3	–	–	–	–	13.8	NaN
	$\phi^{III} = 0.13$	2-UPV-x1	–	–	–	–	22.9	NaN
3	Nano (I)	3-N-x3	251	18	306	107	10.2	5.1
	$\phi^I = 0.10$	3-N-x1	260	12	254	73	11.8	3.9
	Micro (II)	3-M-x3	12,255	80	1,634	452	10.1	2.5
	$\phi^{II} = 0.10$	3-M-x1	12,268	107	1,735	607	14.9	4.0
	Macro (III)	3-UPV-x3	–	–	–	–	21.0	NaN
	$\phi^{III} = 0.075$	3-UPV-x1	–	–	–	–	31.7	NaN

Table 6. Overview of experimental results.

Bringing these three observations together provides evidence for the origin of the anisotropy at level I: Given the continuity of the stiffness scaling relation and the absence of any specific morphology in the stiffness maps, the origin of this anisotropy cannot be attributed neither to the anisotropy of different clay minerals, nor to the difference of porosity (see Table 6); but rather to some privileged orientation of clay minerals at level I, as a consequence of the deposition history of each shale material. Indeed, while almost absence in shale 1 ($\phi^I = 0.31$), and rather weak in shale 3 ($\phi^I = 0.10$), the nanoscale shale anisotropy is quite strong for shale 2 ($\phi^I = 0.18$).

Level 'II': Textured Clay Layer Composite The porous clay composite from level I forms a layered textured matrix at level II that is representative of shales at a scale of tens of micrometers. This microfabric signature of shale materials, which is most likely a consequence of the deposition history is clearly visible in SEM images of 100 to 1000 times magnification, as shown in Figure 19 for the three shale materials. Some trendlines have been superimposed on the microphotographs to highlight the layered texture at the considered scale, as well as the perturbation of the layered structure through the presence of silt inclusions of micrometer size. The smaller the magnification the more regular and homogeneous the visible layered structure, which suggests that the shale fabric becomes

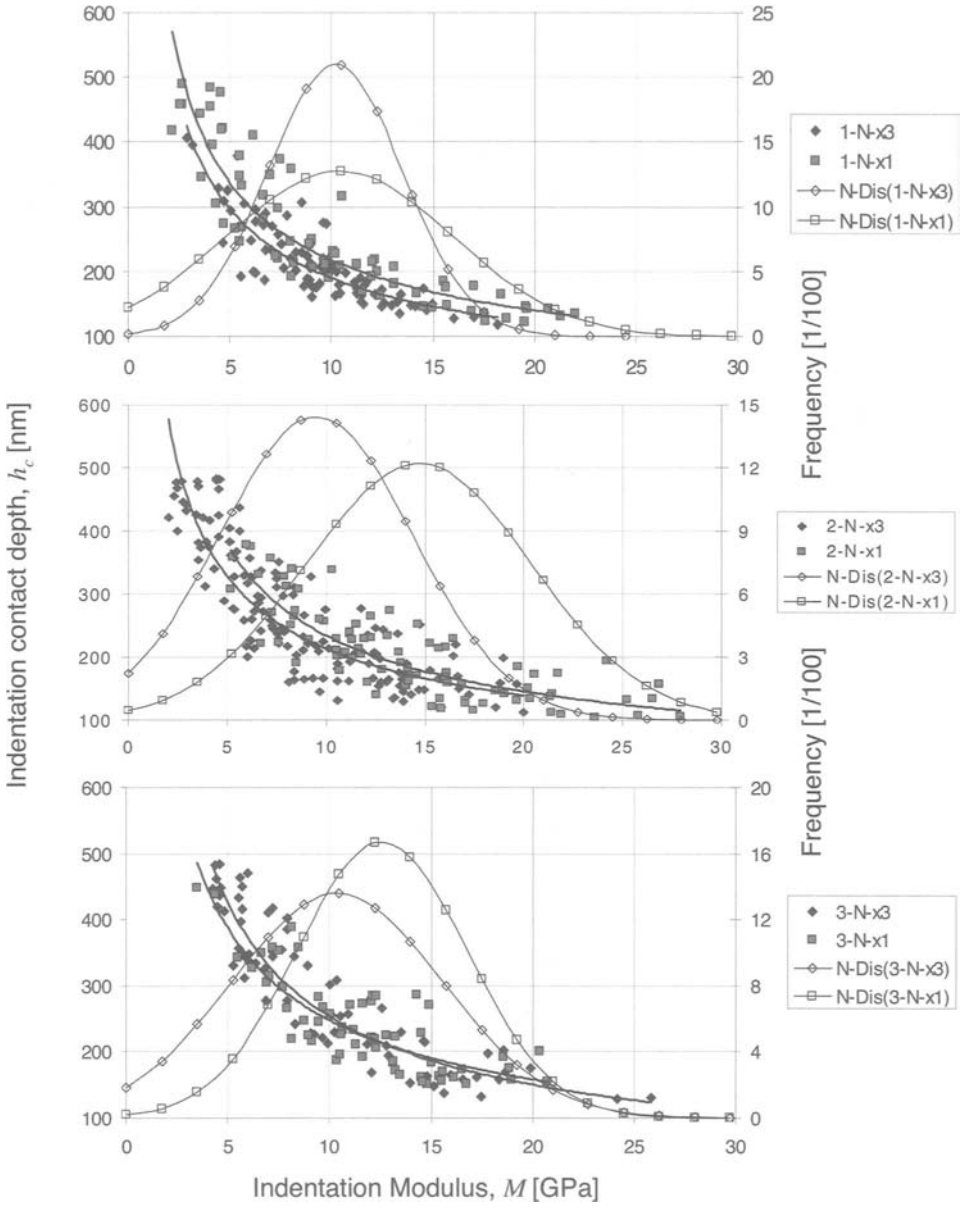

Figure 16. Nanoindentation stiffness scaling relation.

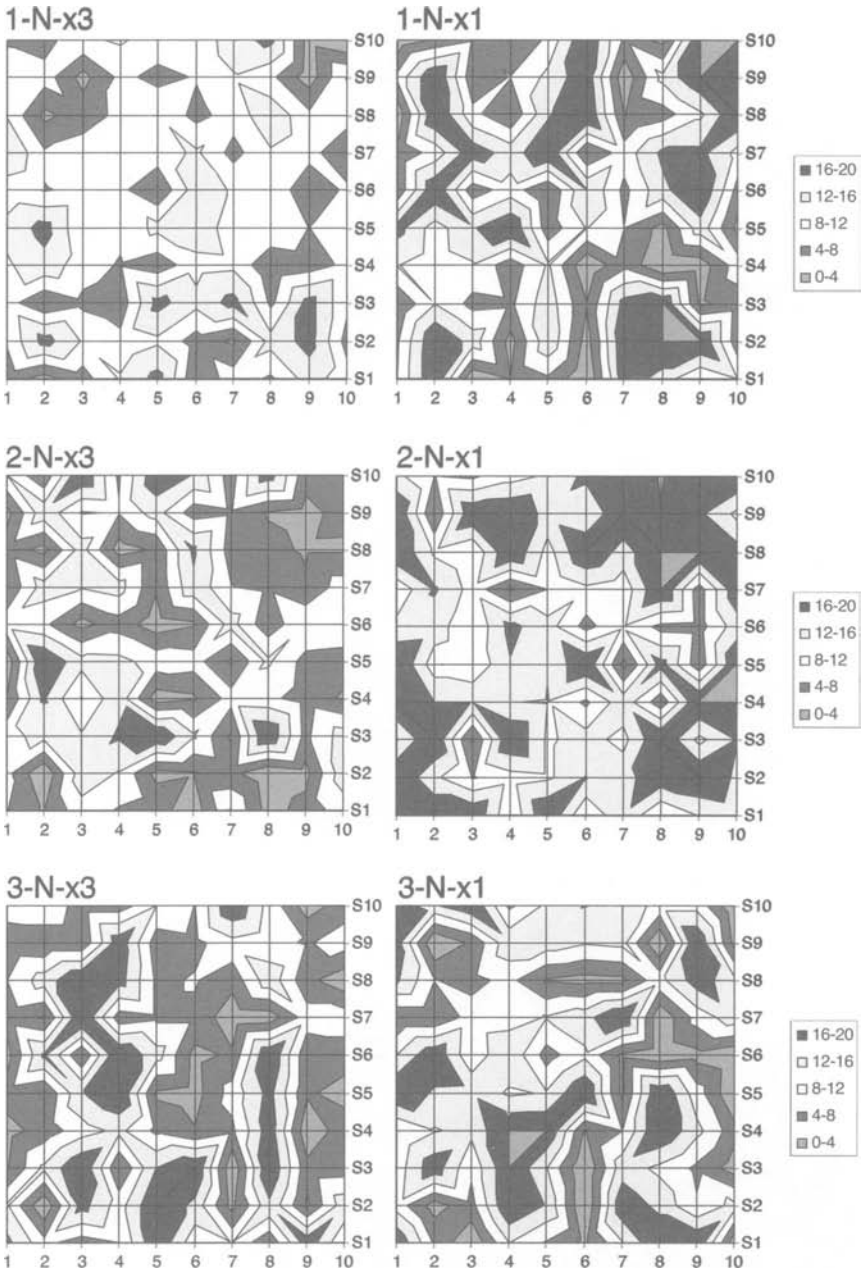

Figure 17. Nanoindentation stiffness maps.

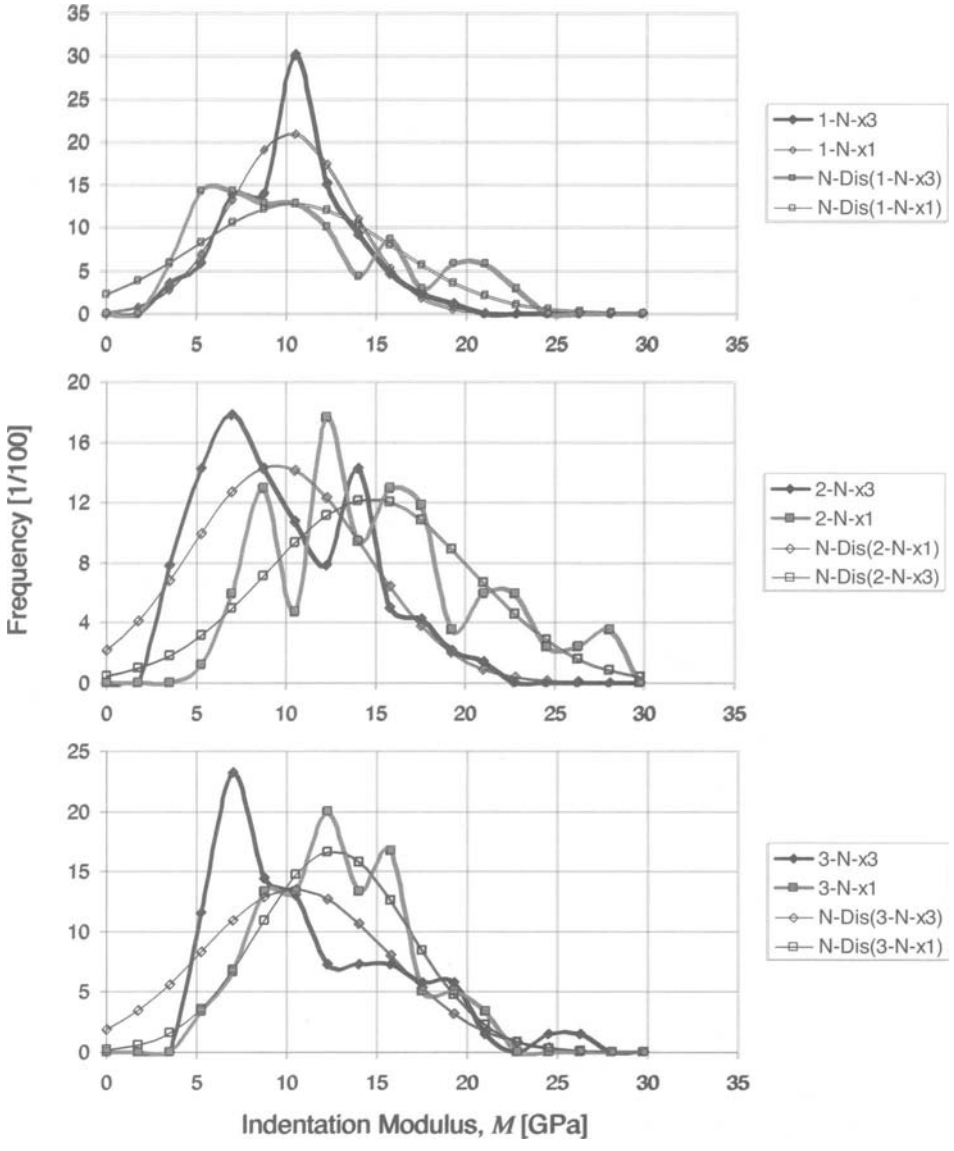

Figure 18. Nanoindentation stiffness frequency distribution.

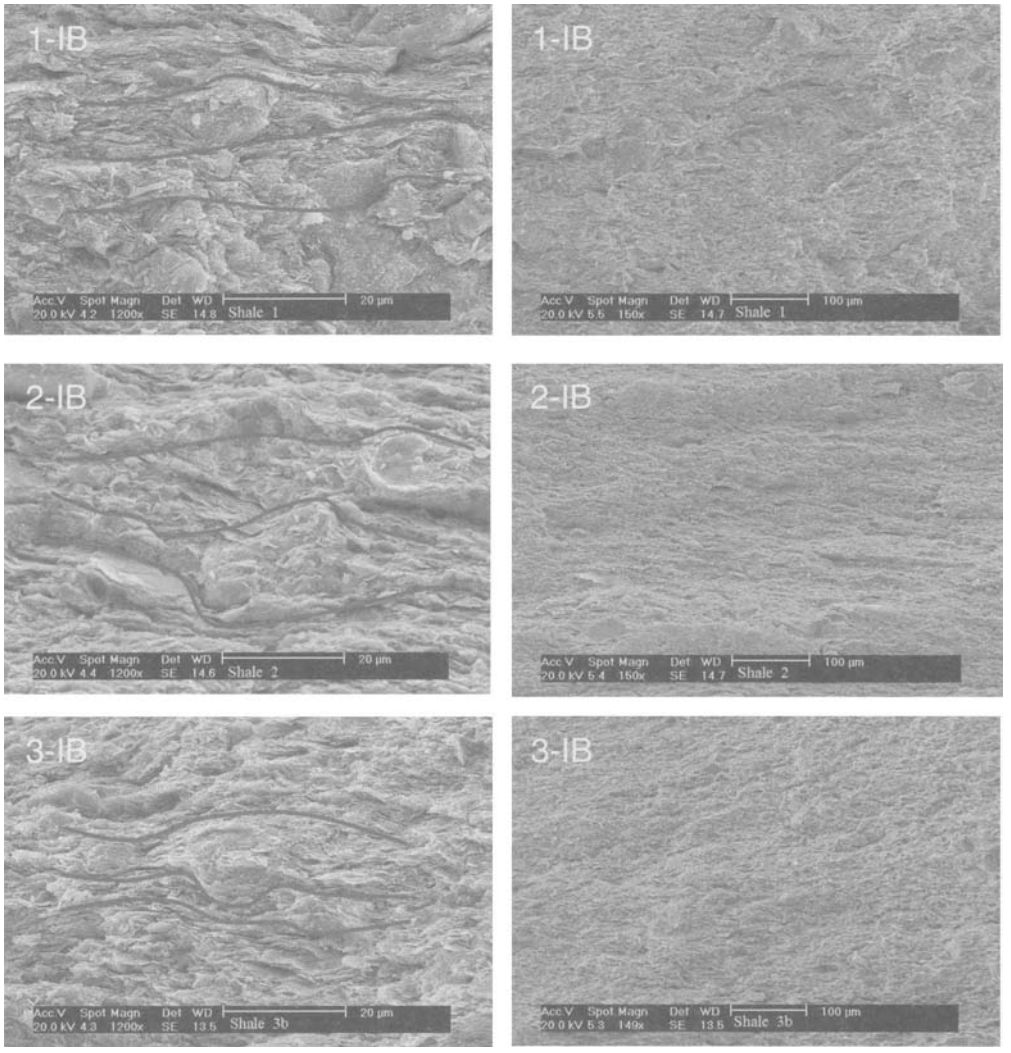

Figure 19. SEM Images of shales at level II (from Chevron Texaco).

more and more dominant at larger than at smaller scales. That what changes from Level I to Level II is the texture.

A clear indication of the effect of texture are *micro*indentation results obtained with a maximum force that is roughly 50 times greater than the one employed in the series of *nano*indentation tests (see Table 6). The resulting maximum indentation depth in the nanoindentation tests is on the order of $1,000 - 5,000\,\text{nm}$, *ie.* roughly 10 times greater than nanoindentation depths. The derived properties, therefore, should be representative

of shale materials on the order of tens of micrometer. The results which are summarized in Table 6, show a clear trend that the stiffness increases as a function of the porosity, and this both normal to bedding and in bedding direction:

$$M^{II}_{3,\text{exp}} = 6.9\,(6.4) - 8.0\,(8.0) - 10.1\,(9.9)\ \text{GPa} \tag{4.44a}$$

$$M^{II}_{1,\text{exp}} = 9.5\,(9.6) - 14.2\,(15.3) - 14.9\,(16.2)\ \text{GPa} \tag{4.44b}$$

In contrast to the nanoindentation results, there is a clear separation of the microindentation stiffness scaling relation (Figure 20), and a clear one-peak distribution of the stiffness values (Figure 21), that are both indicative of the (micro)mechanical anisotropic nature of shale materials at level II. The peak values (which are given in parenthesis in (4.44)) are used to calculate the anisotropy ratio:

$$\frac{M^{II}_{1,\text{exp}}}{M^{II}_{3,\text{exp}}} = 1.5 - 1.9 - 1.6 \tag{4.45}$$

A comparison of (4.43) and (4.45) shows the added anisotropy due to the layered structure, exceeding the anisotropy present at smaller scales.

Level 'III': Macroscopic Clay–Quartz Inclusion Composite The textured clay composite of level II together with quartz inclusions forms a macroscopic composite material, that becomes visible at the sub-millimeter to millimeter scale. The material at this scale is composed of a textured clay matrix with an in-general abundant population of poorly sorted detrital grains (quartz inclusions), that are either concentrated into laminations located between thinner, clay-rich (or quartz starved), lens shaped lams, or homogeneously distributed throughout. This scale has been extensively researched, in the shale acoustics and exploration geophysics community, by means of compressional and shear-wave velocity measurements (Thomsen, 1986; Brittan et al., 1995; Tsvankin, 1996; Hornby, 1998; Sayers, 1999; Wang, 2002; Pratson et al., 2003), and it is now generally agreed that shales behave elastically as transverse isotropic media. The typical wave length employed in such studies operated at frequencies in the MHz range, is in the millimeter range, which captures well the composite stiffness of the macroscopic clay-quartz inclusion composite.

Table 6 provides the values of the equivalent indentation moduli derived from UPV measurements of the three shale materials. It should be noted that UPV-measurements carried out on saturated shale materials are undrained stiffness values, which may explain some hydraulic stiffening effects, in addition to stiffening induced by the presence of quartz inclusions. For pure purpose of comparison, we calculate the anisotropy ratio:

$$\frac{M^{III}_{1,\text{exp}}}{M^{III}_{3,\text{exp}}} = 1.4 - 1.7 - 1.5 \tag{4.46}$$

The fact that the anisotropy of the macroscopic composite is slightly smaller than the one of the textured clay composite (level II; (4.45)) is not surprising: mixing a (more-or-less) isotropic inclusions into an anisotropic material system reduces the anisotropy.

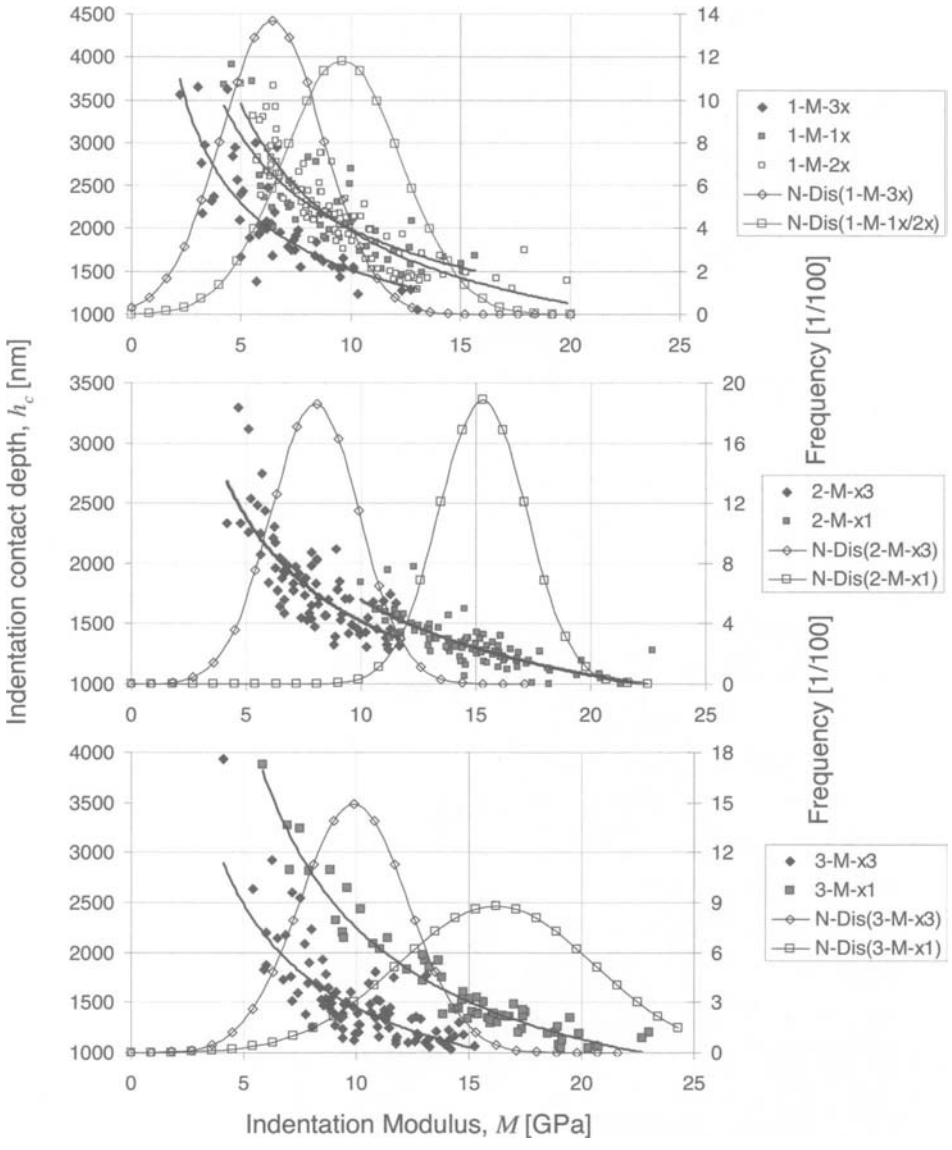

Figure 20. Microindentation scaling relation.

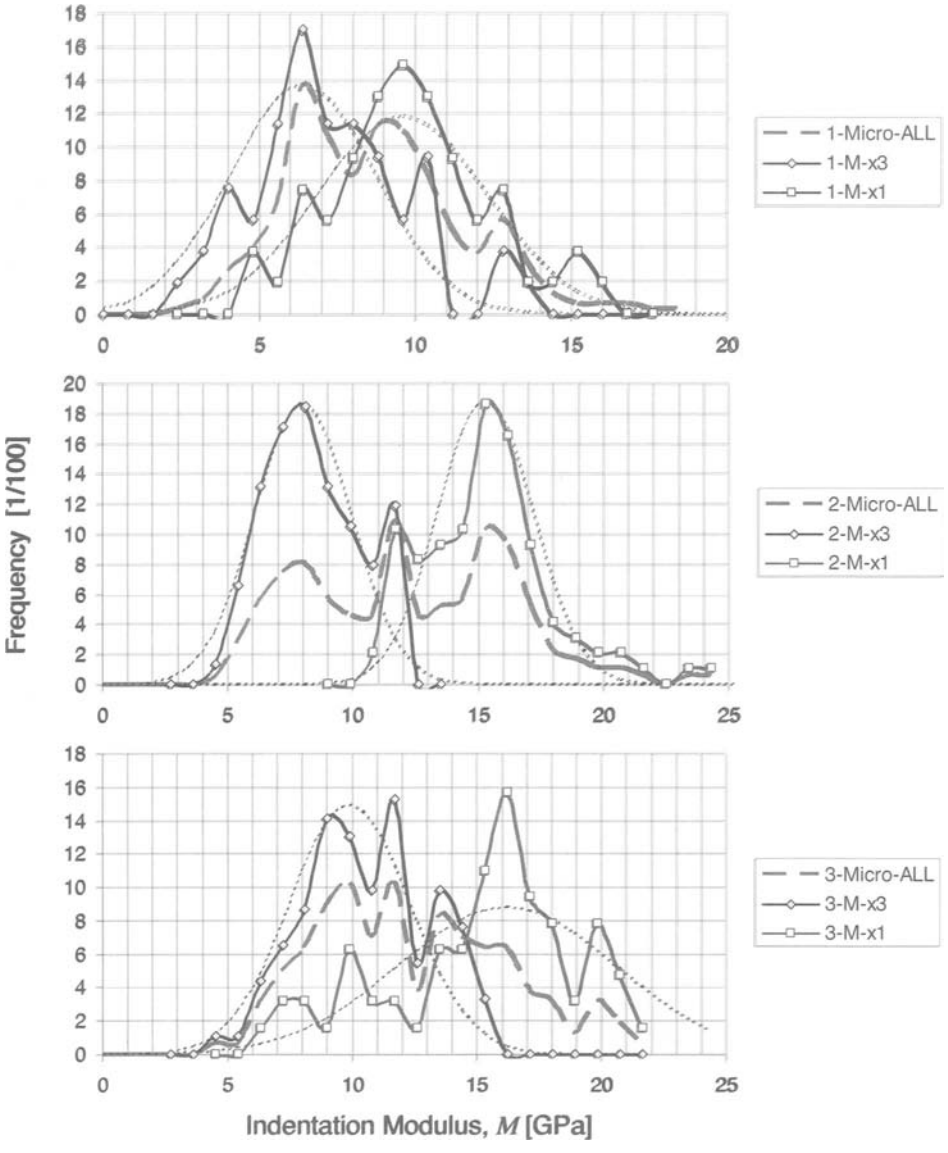

Figure 21. Microindentation frequency plot.

4.2 Anisotropic Microporoelasticity of Shale Materials

The overall trend that emerges from the multiscale indentation analysis is that the anisotropy of shale materials increases from smaller to larger scales.

Sources of Anisotropy Representation Our first objective is to analyze indentation results by means of a microporomechanics modeling approach. As an experimental base, we have six experimental indentation stiffness values for each shale material: $M^I_{1,\text{exp}}, M^I_{3,\text{exp}}, M^{II}_{1,\text{exp}}, M^{II}_{3,\text{exp}}, M^{III}_{1,\text{exp}}, M^{III}_{3,\text{exp}}$ (see Table 6). Using (2.44) and (2.52), each of these indentation stiffness values provides a snapshot of the elasticity of the stiffness values $C^J_{1111}, C^J_{3333}, C^J_{1122}, C^J_{1133}, C^J_{2323}$ (or $C^J_{11}, C^J_{33}, C^J_{12}, C^J_{13}, C^J_{44}$) at each considered scale $J = I, II, III$. Since there is *a priori* no reason that the five elasticity constants at different scales should coincide, there is a total of 6 knowns for a total of 15 unknowns. This imbalance highlights the necessity for a micromechanics approach, requiring at each scale three further information to complete the stiffness characterization, that cannot rely on an empirical choice only. The micromechanics model aims at answering the following questions:

1. Level '0': *In the light of the decreasing anisotropy at smaller scales, is it possible that the elementary building block of shale materials were isotropic?* – Given the anisotropy of the clay minerals it is unlikely that shales at the nanoscale are mechanical isotropic materials. However, the stiffness values of clay minerals (Table 5) are (at least) one order of magnitude greater than the nanoindentation stiffness values (Table 6). This observation suggests that it is not the mineral elasticity itself, but rather the contact regions in between minerals, *ie.* the inter-mineral porosity, that governs the elasticity (See Figure 22, top right). In fact, deformation in the crystalline structure vis-à-vis deformation at the interface between clay particles involve much higher forces, energies and stiffness. The simplest continuous representation of such a discrete material system comes to replace a discrete assembly of grains by a continuous solid phase intermixed with some porosity (Fig. 22, top left). This assumption (and it is one!) provides a convenient way to localize the total elastic deformation in a conceptual continuous pure clay phase, whereas it physically occurs both in very stiff clay flakes and in the contact regions between them. The two possible sources of anisotropy are then the anisotropy of the solid phase and the pore morphology. Given the trend that clay minerals appear in packages, forming the surrounding solid of the porosity, it is convenient to attribute the entire anisotropy at the scale of the elementary building block of shale materials, to the pore morphology by assuming the pure clay phase isotropic. This reduces the number of unknowns to three: two elastic constants and the pore aspect ratio. More specifically, since the shape of clay particles can be approached by the one of flat ellipsoids, we will assume that the pores have the same morphology: an oblate spheroid with a varying aspect ratio $\rho = h/D$, where h is the thickness and D the diameter of the pore (Figure 22, bottom left). Hornby et al. (1994) choose a unique value for the pore aspect ratio in his model, 1/20, equivalent to the one of clay particles. The pore aspect ratio depends more generally on other parameters as well, like pore pressure and depth (Jacobsen et al., 2003). Moreover, if we con-

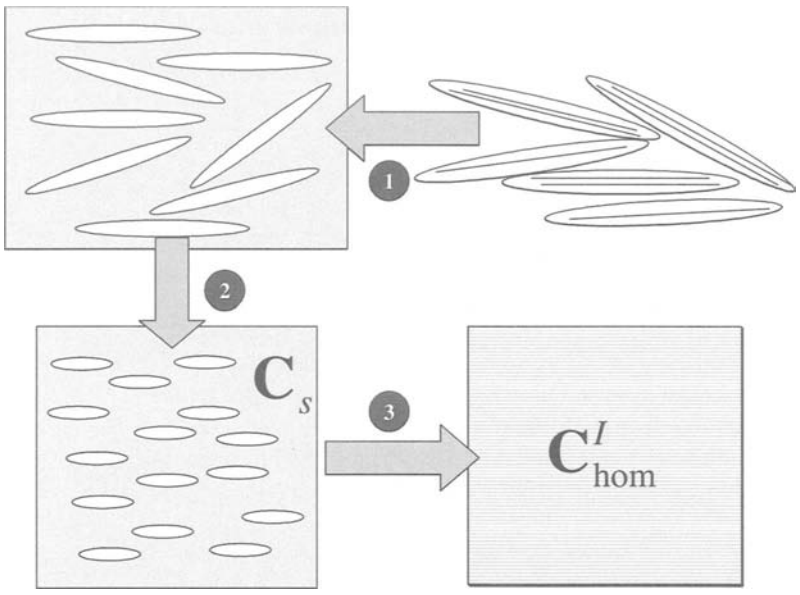

Figure 22. Three steps to model the shale elementary building block from level 0 (top right) to level 1 (bottom right): The first and second ones show the continuous and isotropic representation of clay particles (1) and simplified manifestation of porosity (2); the third one regards it as a (micro)homogeneous phase.

sider that the pores are the sole source of the shale anisotropy at level '0' defined by a unique value of ρ, one should expect a significant decrease in macroscopic anisotropy with decreasing porosity, other parameters being equal.

2. Level 'I': *If the shale building block is clearly anisotropic, why did nanoindentation operated to nanoindentation depths of 100 and 400 nm which activate approximately a bulk comparable to the shale building block, give very close average values when performed in bedding or normal to bedding planes?* – The nanoindentation results show a fair amount of randomness of the distribution of the stiffness in the microstructure. However, since the stiffness distributions in different indentation directions do not coincide (see Figure 16), the randomness of the extracted properties should not be attributed to randomness in a mechanical sense, *ie.* isotropy. Instead, it appears as a consequence of the randomness of the indentation locus defined by the grid size that is much larger than both the indentation depth and the distance in between clay particles. In other words, the elementary building blocks –and the associated anisotropy– manifest themselves at a scale that is much smaller than the indentation grid size. As a consequence the statistical averages of nanoindentation stiffness values are not averages in the sense of a mechanical homogenization; but reflect the orientations of shale building blocks encountered in both in-bedding and normal-to-bedding tests as shown on Figure 23. For instance, if the

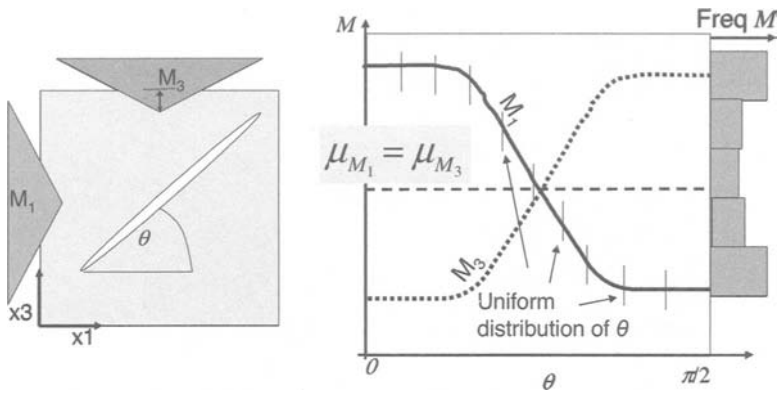

Figure 23. Nanoindentation on a shale elementary building block, level I (left). The indentation stiffness depends on the orientation of the pores, ie of the building block. In the remarkable case where all orientations are uniformly distributed in the shale (right), the average indentation modulus of a grid of tests does not depend on the indented surface orientation. The stiffness frequency exhibits an interesting two-peak distribution.

pore orientation of building blocks has a uniform orientation distribution, then the statistical average of individual stiffness values would be the same for in-bedding and the normal-to-bedding indentations, although the stiffness distribution in each indentation direction contains a large range of values (Fig. 23). The highest (resp. lowest) expected stiffness is obtained when the pore normal direction is perpendicular (resp. parallel) to the axis of indentation. Any difference in between the two averages can be explained by a non-uniform orientation distribution function (ODF) of pores, flakes or shale building blocks. This non-uniform orientation distribution is a third model parameter capturing the disorder of shale materials at level I.

3. Level 'II': *How does the pore morphology from the building block translates into the pronounced anisotropy of the layered shale structure?* – The microindentation results display a (more-or-less) clear one-peak distribution, so that values obtained at this scale can be associated with averages in a mechanical homogenization sense, averaging stiffness values of shale building blocks over a large volume. At this scale, the anisotropy increases for all shales which suggests that an additional morphological feature appears. Porosity, pore shape and orientation distribution functions are already determining the anisotropy in the statistical analysis of nanoindentation. The only possible reason that remains is a particular spatial distribution of shale building blocks. From SEM pictures at that scale, the orientation of the flakes is locally variable, but some wavy separation lines in the bedding directions indicate a clear privileged direction (Figure 19). This can be translated in a schematic laminate of shale building blocks oriented in the bedding directions, where each layer corresponds to one particular orientation of building blocks, as Figure

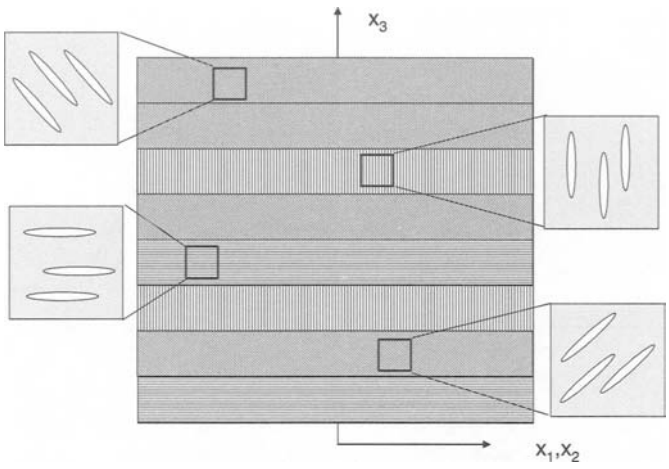

Figure 24. The schematic layered model for the shale microfabric. Each layer is defined by a unique orientation of pores, ie shale building blocks. The resulting laminate is aligned along the shale bedding planes.

24 shows. Similar to a brick wall composed of bricks and joints, such a representation suggests that horizontal pores (joints) are connected whereas vertical ones are interrupted, so that the pronounced anisotropy of shales at larger scales appears as a consequence of the connectivity of pores, with lower stiffness values in the direction normal to bedding (axis $x3$) than in-bedding (axis $x1$ and $x2$).

The suggested microporomechanics representation of shale materials is no-doubt reductionist, reducing the complexity of shales to an isotropic pure clay phase, an oriented pore space and an orientation distribution function. The model has a total of four model parameters, if we exclude the two volume fractions, porosity and inclusion, which are generally known from independent measurements. The porosity at level I and II is the same, while the porosity at level III is related to the former by:

$$\phi_0^{III} = (1 - f_I)\,\phi_0^{II} \tag{4.47}$$

Given this reduced number of model input parameters, we use the four indentation stiffness values $M^I_{1,\text{exp}}, M^I_{3,\text{exp}}, M^{II}_{1,\text{exp}}, M^{II}_{3,\text{exp}}$ as a first data set for a calibration of the model. Using the calibrated model parameters, we then predict the macroscopic stiffness, and compare these predictions with the stiffness values from a second independent data set obtained by UPV-measurements.

Level '0': Shale Building Block We assume that the shale building bock is composed of a solid phase and a porosity, for which the classical relations of anisotropic

poroelasticity apply (Coussy, 2004):

$$\boldsymbol{\Sigma} = \mathbb{C}^{\text{hom}} : \mathbf{E} - \mathbf{b}p \tag{4.48a}$$

$$\phi - \phi_0 = \mathbf{b} : \mathbf{E} + \frac{p}{N} \tag{4.48b}$$

where $\mathbb{C}_{\text{hom}}$ is the stiffness tensor, $\mathbf{b}$ the 2nd order tensor of Biot coefficients, and N the solid Biot modulus. The homogenization rules for this classical poroelastic material system are well established by now (Chateau and Dormieux, 2002; Dormieux and Bourgeois, 2003):

$$\mathbb{C}^I_{\text{hom}} = (1-\phi_0)\,\mathbb{C}_s : \langle \mathbb{A}(\underline{z}) \rangle_{V_s} \tag{4.49a}$$

$$\mathbf{b}^I = \boldsymbol{\delta} : \phi_0 \langle \mathbb{A}(\underline{z}) \rangle_{V_\phi} = \boldsymbol{\delta} : \left(\mathbb{I} - \mathbb{C}_s^{-1} : \mathbb{C}^I_{\text{hom}}\right) \tag{4.49b}$$

$$\frac{1}{N^I} = \boldsymbol{\delta} : \mathbb{C}_s^{-1} : (\mathbf{b} - \phi_0 \boldsymbol{\delta}) \tag{4.49c}$$

where $\mathbb{C}_s$ is the stiffness tensor of the (assumed) isotropic clay solid (bulk modulus k_s, shear modulus g_s):

$$\mathbb{C}_s = 3k_s\mathbb{J} + 2g_s\mathbb{K} \tag{4.50}$$

where we recall that $J_{ijkl}=1/3\ (\delta_{ij}\delta_{kl})$ and $\mathbb{K} = \mathbb{I} - \mathbb{J}$; $\mathbb{I}$ is the fourth order identity tensor $I_{ijkl} = \frac{1}{2}(\delta_{ik}\delta_{jl} + \delta_{il}\delta_{jk})$, and δ_{ij} is the Kronecker delta. Furthermore, $\mathbb{A}(\underline{z})$ is a forth-order strain localization tensor, which concentrates the macroscopic strain tensor prescribed at the boundary into the microscopic solid phase. For the solid-pore morphology, a good estimate of the volume averages $\langle \mathbb{A}(\underline{z}) \rangle_{V_s}$ and $\langle \mathbb{A}(\underline{z}) \rangle_{V_\phi}$ is provided by the Mori-Tanaka scheme (see e.g. Zaoui (2002)):

$$\langle \mathbb{A}(\underline{z}) \rangle_{V_s} \simeq \mathbb{A}_s^{est} = \left[(1-\phi_0)\mathbb{I} + \phi_0 \left(\mathbb{I} - \mathbb{S}^s_\rho\right)^{-1}\right]^{-1} \tag{4.51}$$

$$\langle \mathbb{A}(\underline{z}) \rangle_{V_\phi} \simeq \mathbb{A}_\phi^{est} = \left(\mathbb{I} - \mathbb{S}^s_\rho\right)^{-1} : \left[(1-\phi_0)\mathbb{I} + \phi_0 \left(\mathbb{I} - \mathbb{S}^s_\rho\right)^{-1}\right]^{-1} \tag{4.52}$$

where $\mathbb{S}^s_\rho$ is the Eshelby tensor (Eshelby, 1957) that depends on the aspect ratio $\rho = h/D$ of the pores and the Poisson's ratio of the matrix (see Appendix). Using the estimate (4.51) in (4.49a) yields the homogenized stiffness of a transversely isotropic material in the principle material axis, defined by the pore plane that extends in the $x1' \times x2'$ plane, and whose normal is oriented in direction $x3'$. In this base, the components of the stiffness tensor are of the form (2.40), and the tensor of Biot coefficients is a diagonal tensor having as components:

$$b_{ij} = \begin{bmatrix} b_{11} & 0 & 0 \\ & b_{11} & 0 \\ & & b_{33} \end{bmatrix} \tag{4.53}$$

where b_{11} and b_{33} represent the Biot coefficients in the horizontal and vertical direction in the shale building block:

$$b_{11} = \phi_0^I \left[A^{est}_{\phi,1111} + A^{est}_{\phi,1122} + A^{est}_{\phi,1133}\right] \tag{4.54a}$$

$$b_{33} = \phi_0^I \left[2A^{est}_{\phi,1133} + A^{est}_{\phi,3333}\right] \tag{4.54b}$$

It is convenient to express the homogenized stiffness of the shale building block in a coordinate system $(x1, x2, x3)$, in which the pore plane's normal orientation is defined by the Euler angles θ and φ (See Figure 25):

$$\underline{n} = \sin\theta\cos\varphi\,\underline{e}_1 + \sin\theta\sin\varphi\,\underline{e}_2 + \cos\theta\,\underline{e}_3 \tag{4.55}$$

$\theta = \varphi = 0$ corresponds to a pore plane oriented by the normal pointing in direction $x3$; and $\theta = \pi/2, \varphi = 0$ and $\theta = 0, \varphi = 0$ corresponds to pore planes oriented by a unit normal in direction $x1$ and $x2$, respectively. The relations between the second order strain and stress tensors in the reference and rotated configurations are given by:

$$\mathbf{E}_{\theta,\varphi} = \mathbf{R}(\theta,\varphi)\cdot\mathbf{E}_0\cdot\mathbf{R}(\theta,\varphi)^T \tag{4.56a}$$

$$\mathbf{\Sigma}_{\theta,\varphi} = \mathbf{R}(\theta,\varphi)\cdot\mathbf{\Sigma}_0\cdot\mathbf{R}(\theta,\varphi)^T \tag{4.56b}$$

where $\mathbf{R}(\theta,\varphi)$ is the rotation matrix:

$$R_{ij}(\theta,\varphi) = \begin{bmatrix} 1 & 0 & 0 \\ 0 & \cos(\theta) & -\sin(\theta) \\ 0 & \sin(\theta) & \cos(\theta) \end{bmatrix} \begin{bmatrix} \cos(\varphi) & -\sin(\varphi) & 0 \\ \sin(\varphi) & \cos(\varphi) & 0 \\ 0 & 0 & 1 \end{bmatrix} \tag{4.57}$$

Using (4.56) in (4.48), the poroelastic constants read in the rotated configuration:

$$\mathbb{C}^I_{\text{hom}}(\theta,\varphi) = \mathbf{R}(\theta,\varphi)\cdot\mathbb{C}^I_{\text{hom}}(0,0)\cdot\mathbf{R}(\theta,\varphi)^T \tag{4.58a}$$

$$\mathbf{b}^I(\theta,\varphi) = \mathbf{R}(\theta,\varphi)\cdot\mathbf{b}^I(0,0)\cdot\mathbf{R}(\theta,\varphi)^T \tag{4.58b}$$

Level 'I': Statistical Averages We consider that the mean nanoindentation results represent statistical averages of a representative sample of indentation tests on elementary building blocks present on a specific surface (Fig. 17). The statistical average of the indentation tests on this surface oriented in the $xJ-$direction is:

$$\mu_{M_J} = \frac{1}{2\pi}\int_{\theta=0}^{\pi}\int_{\varphi=0}^{2\pi} M_J(\theta,\varphi)\sin\theta\,d\varphi\,d\theta \tag{4.59}$$

where $M_J(\theta,\varphi)$ is the indentation modulus of a single indentation test on an elementary building block rotated by Euler angles θ and φ w.r.t. the indentation axis xJ. Assuming the function to be continuous, the indentation modulus has two extrema: a minimum for indentation normal to the pore plane, *ie.* $\underline{n}\cdot\underline{e}_J = 1$, and a maximum for indentation in the pore plane, *ie.* $\underline{n}\cdot\underline{e}_J = 0$:

$$\forall \underline{n}\cdot\underline{e}_J = 1 \Rightarrow M_J(\theta,\varphi) = \min M \tag{4.60a}$$

$$\forall \underline{n}\cdot\underline{e}_J = 0 \Rightarrow M_J(\theta,\varphi) = \max M \tag{4.60b}$$

Combining (4.55) with (4.60), we recognize for indentation in bedding directions (axis $x1$ and $x2$) and normal to it (axis $x3$):

$$\begin{array}{lll} \min M & = M_1(\pi/2,0) & = M_2(\pi/2,\pi/2) \quad = M_3(0,\varphi) \\ \max M & = M_1(0,\varphi) & = M_2(0,\varphi) \quad\;\; = M_3(\pi/2,\varphi) \\ & = M_1(\theta,\pi/2) & = M_2(\theta,0) \end{array} \tag{4.61}$$

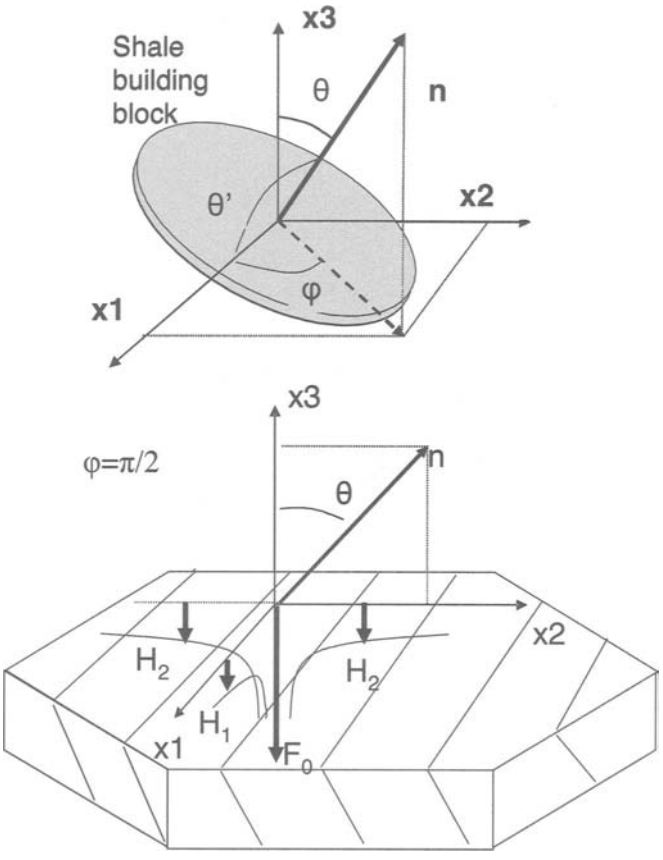

Figure 25. (top) The orientation of a transverse isotropic shale elementary building block is defined by the direction of its axis of symmetry, with the two Euler angles θ and φ in the cartesian system $Ox_1x_2x_3$; (bottom) Schematic representation of the surface Green function extreme profiles, when the axes of material symmetry and indentation (x_3) form any angle θ. Without loss of generality we consider here $\varphi = \pi/2$, and the extremal values of $\mathcal{H}$, H_1 and H_2, are obtained in the $x_1$and x_2 directions.

The minimum value $\min M$ is strictly the indentation modulus for indentation in the symmetry axis of a transversely isotropic material, which is related to the elastic constants $\mathbb{C}_{\text{hom}}(0,0)$ through (2.44). Similarly, the maximum value $\max M$ is the indentation modulus for indentation in the plane of symmetry of a transversely isotropic material, which is related to $\mathbb{C}_{\text{hom}}(0,0)$ through (2.52). For any other orientation of the pore plane defined by $\cos\theta'(\theta,\varphi) = \underline{n}\cdot\underline{e}_J$, the link between the indentation modulus $M_J(\theta')$ and the elasticity of the building block $\mathbb{C}_{\text{hom}}(0,0)$ is estimated from a generalization of (2.52):

$$M_J(\theta') \simeq \frac{1}{\pi\sqrt{\mathcal{H}_K\mathcal{H}_L}} \tag{4.62}$$

satisfying:

$$M_J(\theta'=0) = \min M \tag{4.63a}$$

$$M_J(\theta'=\pi/2) = \max M \tag{4.63b}$$

where $\mathcal{H}_K = \mathcal{H}(\theta'=0)$ and $\mathcal{H}_L = (\theta'=\pi/2)$ are the extreme values of the Green's function angular part $\eta(\theta')$ given by (2.35)[11] and are represented schematically on Figure 25. However, in contrast to the closed form expressions (2.44) and (2.52), these extreme values cannot be expressed in closed form for $\theta' =]0,\pi/2[$, and need to be numerically evaluated.

Relation (4.62) contains not only the elastic stiffness information of the elementary building block, but as well the distribution of indentation moduli as a function of the pore plane orientation $\cos\theta' = \underline{n}\cdot\underline{e}_J$ situated in between the two extrema, $\min M$ and $\max M$. This distribution corresponds to a uniform orientation distribution of building blocks (*ie.* pore orientations) on a specific surface. It implies that shale building blocks have their axis of symmetry pointing in all directions with uniform probability density. A refinement of this theory can be achieved by considering an orientation distribution function $W(\theta,\varphi)$ in the evaluation of the statistical average (4.59):

$$\mu_{M_J} = \frac{1}{2\pi}\int_{\theta=0}^{\pi}\int_{\varphi=0}^{2\pi} M_J(\theta,\varphi)\,W(\theta,\varphi)\sin\theta\,d\varphi\,d\theta \tag{4.64}$$

This orientation distribution function needs to satisfy:

$$\frac{1}{2\pi}\int_{\theta=0}^{\pi}\int_{\varphi=0}^{2\pi} W(\theta,\varphi)\sin\theta\,d\varphi d\theta = 1 \tag{4.65}$$

For shale materials, orientation distribution functions were first introduced by Sayers (1994), and have gained some popularity as an important tool to account for a non-uniform distribution of the orientation of clay particles, that can be determined experimentally (see e.g. Johansen et al. (2004)). We employ this concept here to account for a

[11] This interpolation of the extreme values of the Green's function angular part $\eta(\theta')$ is justified by the fact that the half-space Green function, π-periodic by definition, conserves its eveness, because of a material plane symmetry.

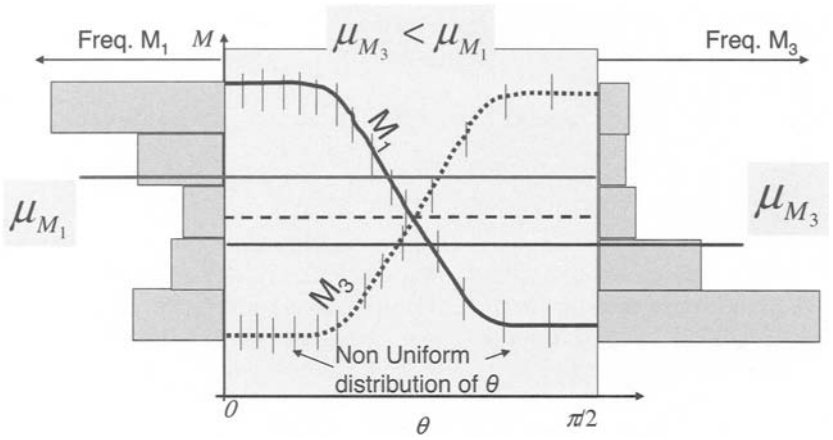

Figure 26. Average and distribution of indentation moduli in the two indented direction at the nano-scale. The anisotropy depends on the anisotropy of the shale building blocks, and on the orientation distribution function and the k factor.

non-uniform orientation distribution of building blocks; and chose a π-periodic Gaussian like function:

$$W(\theta, k) = w_k \cosh(k \cos\theta) \tag{4.66}$$

where $w_k = 2/k \cosh k$ is a normalization constant, and k a parameter referring to the degree of preferred alignment: $k = 0$ means an absence of any preferred alignment, and $k > 0$ induces a second source of anisotropy in the shale micromechanics model.

The resulting statistical average (4.64) illustrated on Figure 26 depends on the elastic constants of the isotropic solid clay phase –bulk modulus k_s, shear modulus g_s (see (4.50))–, the pore aspect ratio $\rho = h/D$ and the $k-$ factor; in addition to the clay porosity ϕ^I; and provides a direct link between the $4 + 1$ model parameters and the experimental mean nanoindentation stiffness values $M^I_{1,\text{exp}} \equiv \mu_{M_1}$ and $M^I_{3,\text{exp}} \equiv \mu_{M_3}$, respectively the anisotropy ratio $M^I_{1,\text{exp}}/M^I_{3,\text{exp}}$.

Level 'II': Microporoelasticity of Porous Laminates We consider that the textured clay layer composite has an infinite number of layers, each being characterized by the orientation of the pores (θ, φ) (Fig. 24). The microindentation results are averages in the sense of micromechanics theory of a layered composite. The inherent assumption in layered composites mechanics is that the strain parameters ε_{11}, ε_{22}, ε_{12} are uniform, as well as the stress components σ_{13}, σ_{23}, σ_{33}. This is true for laminates with vanishing layer thicknesses, which is a special case of the scale separability condition (2.53). There are many different formulations for stress-strain averages of laminates. The one we retain here is the method proposed by El Omri et al. (2000), which provides an explicit formulation of the laminate stiffness tensor as a function of each layer stiffness, using stress-strain hybrid averages. We extend this method to the porous laminate, for which

the layer behavior is defined by the poroelastic state equation:

$$\sigma_{ij} = C_{ijkl}\,\varepsilon_{kl} - b_{ij}\,p \tag{4.67}$$

The idea is to rewrite the poroelastic state equation in a plane-antiplane basis:

$$\begin{pmatrix} \sigma_P \\ \sigma_A \end{pmatrix} = \begin{bmatrix} c_{PP} & c_{PA} \\ c_{AP} & c_{AA} \end{bmatrix} \begin{pmatrix} \varepsilon_P \\ \varepsilon_A \end{pmatrix} - \begin{pmatrix} b_P \\ b_A \end{pmatrix} p \tag{4.68}$$

where subscript P refers to the plane components $11, 22, 12$, whereas subscript A refers to the anti-plane components $31, 23, 33$, and the subscript A, P to the permuted configuration. Adopting the matrix representation of second and forth order tensors proposed by Helnwein (2001), which is different from the classical Voigt representation, the plane-aniplane components of any symmetric second order tensor a_{ij} are obtained from:

$$\mathbf{a} = \mathbb{P} : \begin{pmatrix} a_P & a_A \end{pmatrix}^T = \begin{pmatrix} a_{11} & a_{22} & a_{33} & \sqrt{2}\,a_{23} & \sqrt{2}\,a_{31} & \sqrt{2}\,a_{12} \end{pmatrix}^T \tag{4.69}$$

yielding:

$$\begin{pmatrix} a_P & a_A \end{pmatrix}^T = \mathbb{P}^T : \mathbf{a} = \begin{pmatrix} a_{11} & a_{22} & \sqrt{2}\,a_{12} & \sqrt{2}\,a_{31} & \sqrt{2}\,a_{23} & a_{33} \end{pmatrix}^T \tag{4.70}$$

where the matrix operator $\mathbb{P}$ reads:

$$\mathbb{P} = \begin{bmatrix} 1 & 0 & 0 & 0 & 0 & 0 \\ 0 & 1 & 0 & 0 & 0 & 0 \\ 0 & 0 & 0 & 1 & 0 & 0 \\ 0 & 0 & 0 & 0 & 0 & 1 \\ 0 & 0 & 0 & 0 & 1 & 0 \\ 0 & 0 & 1 & 0 & 0 & 0 \end{bmatrix}; \mathbb{P}^{-1} = \mathbb{P}^T = \begin{bmatrix} 1 & 0 & 0 & 0 & 0 & 0 \\ 0 & 1 & 0 & 0 & 0 & 0 \\ 0 & 0 & 0 & 0 & 0 & 1 \\ 0 & 0 & 1 & 0 & 0 & 0 \\ 0 & 0 & 0 & 0 & 1 & 0 \\ 0 & 0 & 0 & 1 & 0 & 0 \end{bmatrix} \tag{4.71}$$

The plane-antiplane components in (4.68) thus read:

$$\begin{pmatrix} \sigma_P & \sigma_A \end{pmatrix}^T = \mathbb{P}^T : \boldsymbol{\sigma} \tag{4.72a}$$

$$\begin{pmatrix} \varepsilon_P & \varepsilon_A \end{pmatrix}^T = \mathbb{P}^T : \boldsymbol{\varepsilon} \tag{4.72b}$$

$$\begin{pmatrix} b_P & b_A \end{pmatrix}^T = \mathbb{P}^T : \mathbf{b} \tag{4.72c}$$

Similarly, the stiffness components are obtained from:

$$\mathbb{C}_{A,P} = \begin{bmatrix} c_{PP} & c_{PA} \\ c_{AP} & c_{AA} \end{bmatrix} = \mathbb{P}^T : \mathbb{C} : \mathbb{P} \tag{4.73}$$

where $\mathbb{C} = \mathbb{C}^I_{\text{hom}}(\theta, \varphi)$ is the stiffness tensor of each layer, given by (4.58a) in function of the elastic constants of the building block and the orientation of the pore plane (θ, φ). Implemented in matrix form, its components read (Helnwein, 2001):

$$C_{ijkl} = \begin{bmatrix} C_{1111} & C_{1122} & C_{1133} & \sqrt{2}C_{1123} & \sqrt{2}C_{1131} & \sqrt{2}C_{1112} \\ & C_{2222} & C_{2233} & \sqrt{2}C_{2223} & \sqrt{2}C_{2231} & \sqrt{2}C_{2212} \\ & & C_{3333} & \sqrt{2}C_{3323} & \sqrt{2}C_{3331} & \sqrt{2}C_{3312} \\ & & & 2C_{2323} & 2C_{2331} & 2C_{2312} \\ & & & & 2C_{3131} & 2C_{3112} \\ sym & & & & & 2C_{1212} \end{bmatrix} \tag{4.74}$$

The plane-antiplane representation allows for the following remarkable averaging relations:

$$\varepsilon_P \equiv \overline{\varepsilon_P} = E_P = \left(\begin{array}{ccc} E_{11} & E_{22} & \sqrt{2}\,E_{12} \end{array} \right)^T \tag{4.75a}$$

$$\sigma_A \equiv \overline{\sigma_A} = \Sigma_A = \left(\begin{array}{ccc} \sqrt{2}\,\Sigma_{31} & \sqrt{2}\,\Sigma_{23} & \Sigma_{33} \end{array} \right)^T \tag{4.75b}$$

The remaining stress and strain components, not included in laminate averaging relations (4.75) are obtained from a partial inversion of (4.68):

$$\left(\begin{array}{c} \sigma_P \\ \varepsilon_A \end{array} \right) = \left[\begin{array}{cc} k_{PP} & k_{PA} \\ k_{AP} & k_{AA} \end{array} \right] \left(\begin{array}{c} E_P \\ \Sigma_A \end{array} \right) - p \left(\begin{array}{c} l_P \\ l_A \end{array} \right) \tag{4.76}$$

where

$$\begin{array}{ll} k_{PP} = c_{PP} - c_{PA}\, c_{AA}^{-1}\, c_{AP} & l_P = b_P + c_{PA}\, c_{AA}^{-1}\, b_A \\ k_{AA} = c_{AA}^{-1} & \\ k_{PA} = -k_{AP}^T = c_{PA}\, c_{AA}^{-1} & l_A = -c_{AA}^{-1}\, b_A \end{array} \tag{4.77}$$

Averaging (4.76) yields:

$$\left(\begin{array}{c} \Sigma_P \\ E_A \end{array} \right) = \left(\begin{array}{c} \overline{\sigma_P} \\ \overline{\varepsilon_A} \end{array} \right) = \left[\begin{array}{cc} \overline{k_{PP}} & \overline{k_{PA}} \\ \overline{k_{AP}} & \overline{k_{AA}} \end{array} \right] \left(\begin{array}{c} E_P \\ \Sigma_A \end{array} \right) - p \left(\begin{array}{c} \overline{l_P} \\ \overline{l_A} \end{array} \right) \tag{4.78}$$

Finally, after partial inversion, we obtain:

$$\left(\begin{array}{c} \Sigma_P \\ \Sigma_A \end{array} \right) = \left[\begin{array}{cc} C_{PP}^{\hom} & C_{PA}^{\hom} \\ C_{AP}^{\hom} & C_{AA}^{\hom} \end{array} \right] \left(\begin{array}{c} E_P \\ E_A \end{array} \right) - p \left(\begin{array}{c} b_P^{\hom} \\ b_A^{\hom} \end{array} \right) \tag{4.79}$$

where

$$\begin{array}{ll} C_{PP}^{\hom} = \overline{k_{PP}} - \overline{k_{PA}} \left(\overline{k_{AA}}\right)^{-1} \overline{k_{AP}} & b_P^{\hom} = \overline{l_P} + \overline{k_{PA}} \left(\overline{k_{AA}}\right)^{-1} \overline{l_A} \\ C_{AA}^{\hom} = \left(\overline{k_{AA}}\right)^{-1} & \\ C_{PA}^{\hom} = \left(C_{AP}^{\hom}\right)^T = \overline{k_{PA}} \cdot \left(\overline{k_{AA}}\right)^{-1} & b_A^{\hom} = -\left(\overline{k_{AA}}\right)^{-1} \overline{l_A} \end{array} \tag{4.80}$$

The homogenized stiffness of the porous laminate in the original configuration is obtained by inverse application of (4.73):

$$\mathbb{C}_{\hom}^{II} = \mathbb{P} : \mathbb{C}_{A,P}^{\hom} : \mathbb{P}^T \tag{4.81}$$

Similarly, application of (4.72c) yields the tensor of Biot coefficients in the original basis:

$$\mathbf{b}^{II} = \mathbb{P} : \mathbf{b}_{A,P}^{\hom} \tag{4.82}$$

The last poroelastic constant, the Biot modulus N, is a scalar which is not affected by the rotation of the porosity. As a consequence, the Biot modulus is uniform throughout the layered system, and coincides with the solid Biot modulus of the layered composite, $N^{II} = N^I$, given by (4.49c).

Last, the volume average operation in (4.78) of the stiffness matrices $\overline{k_{IJ}}$ reads for a uniform orientation distribution of the pore planes in the laminate:

$$\overline{k_{IJ}} = \frac{1}{2\pi} \int_{\theta=0}^{\pi} \int_{\varphi=0}^{2\pi} k_{IJ}(\theta, \varphi) \sin(\theta) d\varphi d\theta \tag{4.83}$$

Similarly to (4.64) it is appropriate to introduce a non-uniform orientation distribution to account for some degree of preferred alignment:

$$\overline{k_{IJ}} = \frac{1}{2\pi} \int_{\theta=0}^{\pi} \int_{\varphi=0}^{2\pi} k_{IJ}(\theta, \varphi) W(\theta, k) \sin(\theta) d\varphi d\theta \tag{4.84}$$

where $W(\theta, k)$ is the orientation distribution function (4.66). The same non-uniform orientation average operation is applied to all averages in (4.80); including the one involved in the determination of the Biot coefficients.

The resulting homogenized stiffness (4.81) of the porous clay laminate, therefore, depends on the elastic constants of the isotropic solid clay phase –bulk modulus k_s, shear modulus g_s (see (4.50))–, the pore aspect ratio $\rho = h/D$ and the $k-$ factor; in addition to the clay porosity $\phi^I = \phi^{II}$. Using $\mathbb{C}^{II}_{\text{hom}}$ from (4.81) in (2.44) and (2.52) provides the link between these $4+1$ model parameters, and the microindentation stiffness values $M^{II}_{1,\text{exp}}$ and $M^{II}_{3,\text{exp}}$, respectively the anisotropy ratio $M^{II}_{1,\text{exp}}/M^{II}_{3,\text{exp}}$.

Level III: Addition of Inclusions Into an Anisotropic Porous Matrix We consider shale materials at the macroscopic scale to be composed of a textured porous matrix and (mainly) quartz inclusions of approximately spherical shape that are randomly distributed throughout the anisotropic porous matrix V_M (Fig. 27). Except for the anisotropy of the matrix, the microporomechanics problem is very similar to the one we encountered for cement-based materials. Proceeding as before, we adopt a continuous description of the stress field in the heterogeneous r.e.v.:

$$\text{in } V_{III} : \boldsymbol{\sigma}(\underline{z}) = \mathbb{C}(\underline{z}) : \boldsymbol{\varepsilon}(\underline{z}) + \boldsymbol{\sigma}^p(\underline{z}) \tag{4.85}$$

together with the following distributions of the elastic properties $\mathbb{C}(\underline{z})$ and the eigenstress $\boldsymbol{\sigma}^p(\underline{z})$:

$$\mathbb{C}(\underline{z}) = \begin{cases} \mathbb{C}_M \text{ in } V_M \\ \mathbb{C}_i \text{ in } V_i \end{cases} \quad \boldsymbol{\sigma}^p(\underline{z}) = \begin{cases} -\mathbf{b}_M p \text{ in } V_M \\ 0 \text{ in } V_\phi \end{cases} \tag{4.86}$$

where $\mathbb{C}_M = \mathbb{C}^{II}_{\text{hom}}$ is the stiffness tensor of the porous clay laminate (4.81), $\mathbb{C}_i = 3k_i\mathbb{J} + 2g_i\mathbb{K}$ is the stiffness tensor of the (assumed isotropic) quartz inclusion phase; and $\mathbf{b}_M = \mathbf{b}^{II}$ is the second order Biot coefficient tensor of the porous clay laminate (4.82). Following the linear microporomechanics approach, we decompose the problem in (the meanwhile classical) two sub-problems:

1. The first sub-problem corresponds to drained conditions, for which $p = 0$. We assume that the r.e.v. is subjected to a uniform displacement boundary condition, so that the solid boundary conditions to which the solid phase is subjected read

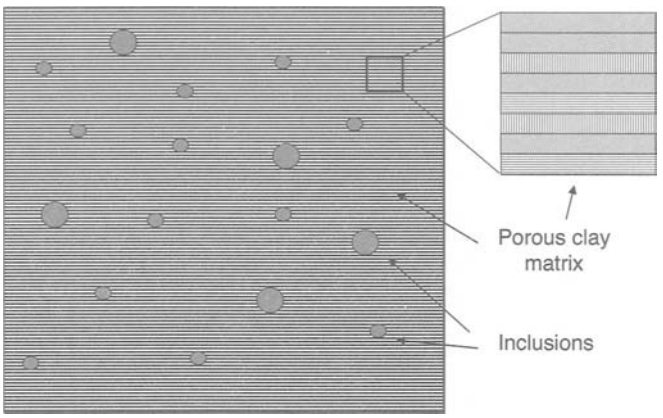

Figure 27. Macroscopic shale model: an anisotropic porous matrix of clay containing randomly distributed spherical inclusions.

(see relation (3.10)):

$$\text{on } \partial V_{III} \quad : \quad \underline{\xi}'(\underline{z}) = \mathbf{E} \cdot \underline{z} \tag{4.87a}$$

$$\text{on } \mathcal{I}_{sf} \quad : \quad \boldsymbol{\sigma} \cdot \underline{n} = 0 \tag{4.87b}$$

The macroscopic strain tensor $\mathbf{E}$ is related to the microscopic strain by the strain localization condition:

$$\boldsymbol{\varepsilon}'(\underline{z}) = \mathbb{A}(\underline{z}) : \mathbf{E} \tag{4.88}$$

$\mathbb{A}(\underline{z})$ satisfies the compatibility condition:

$$\mathbf{E} = \overline{\boldsymbol{\varepsilon}'(\underline{z})} \Leftrightarrow \mathbb{I} = (1 - f_i) \langle \mathbb{A} \rangle_{V_M} + f_i \langle \mathbb{A} \rangle_{V_i} \tag{4.89}$$

where $f_i = V_i / V_{III} = 1 - f_M$ is the inclusion volume fraction. Use of (4.88) in (4.85) together with the elastic distribution (4.86) yields after volume averaging, the macroscopic stress, and the homogenized stiffness of the composite:

$$\boldsymbol{\Sigma}' = \overline{\boldsymbol{\sigma}'(\underline{z})} = \mathbb{C}_{\text{hom}}^{III} : \mathbf{E}; \; \mathbb{C}_{\text{hom}}^{III} = \mathbb{C}_M + f_I (\mathbb{C}_i - \mathbb{C}_M) : \langle \mathbb{A} \rangle_{V_i} \tag{4.90}$$

The change of the porosity in the subproblem reads:

$$\left[(\phi - \phi_0)^{III} \right]' = \mathbf{b}^{III} : \mathbf{E} \tag{4.91}$$

where $\mathbf{b}^{III}$ is the second order tensor of homogenized Biot coefficients.

2. The second sub-problem we consider is the zero-displacement boundary problem, whereas the porosity is pressurized. Using Levine's theorem (3.14) for the eigenstress distribution (4.86), we obtain the macroscopic stress and the homogenized Biot coefficients:

$$\boldsymbol{\Sigma}'' = \overline{\boldsymbol{\sigma}^p(\underline{z}) : \mathbb{A}(\underline{z})} = -\mathbf{b}^{III} p; \; \mathbf{b}^{III} = \mathbf{b}_M : \left(\mathbb{I} - f_i \langle \mathbb{A} \rangle_{V_i} \right) \tag{4.92}$$

The change of the porosity in the subproblem reads:

$$\left[(\phi-\phi_0)^{III}\right]'' = (1-f_i)\left(\mathbf{b}_M : \langle\boldsymbol{\varepsilon}''\rangle_{V_M} + \frac{p}{N_M}\right) \tag{4.93}$$

where $N_M = N^{II}$. We eliminate $\langle\boldsymbol{\varepsilon}''\rangle_{V_M}$ in (4.93) to the benefit of pressure p, by considering the stress average in this sub-problem, in which $\mathbf{E}'' = \overline{\boldsymbol{\varepsilon}''(\underline{z})} = 0$:

$$\begin{aligned}\boldsymbol{\Sigma}'' &= (1-f_i)\langle\boldsymbol{\sigma}''\rangle_{V_M} + f_i\langle\boldsymbol{\sigma}''\rangle_{V_I} \\ &= (\mathbb{C}_M - \mathbb{C}_i) : (1-f_i)\langle\boldsymbol{\varepsilon}''\rangle_{V_M} - (1-f_i)\,\mathbf{b}_M p\end{aligned} \tag{4.94}$$

Thus, from the equality of (4.92) and (4.94):

$$(1-f_i)\langle\boldsymbol{\varepsilon}''\rangle_{V_M} = -(\mathbb{C}_M - \mathbb{C}_i)^{-1} : \left(\mathbf{b}^{III} - (1-f_i)\,\mathbf{b}_M\right) p \tag{4.95}$$

Finally, use of (4.95) in (4.93) yields:

$$\begin{aligned}\left[(\phi-\phi_0)^{III}\right]'' &= \frac{p}{N^{III}}; \\ \frac{1}{N^{III}} &= \frac{1-f_i}{N_M} - f_i\mathbf{b}_M : (\mathbb{C}_M - \mathbb{C}_i)^{-1} : \mathbf{b}_M : \left(\mathbb{I} - \langle\mathbb{A}\rangle_{V_i}\right)\end{aligned} \tag{4.96}$$

In summary, a superposition of the two subproblems yields the macroscopic state equations of the shale composite material:

$$\boldsymbol{\Sigma} = \mathbb{C}^{III}_{\text{hom}} : \mathbf{E} - \mathbf{b}^{III} p \tag{4.97a}$$

$$(\phi-\phi_0)^{III} = \mathbf{b}^{III} : \mathbf{E} + \frac{p}{N^{III}} \tag{4.97b}$$

together with the poroelastic properties:

$$\mathbb{C}^{III}_{\text{hom}} = \mathbb{C}_M + f_I\,(\mathbb{C}_i - \mathbb{C}_M) : \langle\mathbb{A}\rangle_{V_i} \tag{4.98a}$$

$$\mathbf{b}^{III} = \mathbf{b}_M : \left(\mathbb{I} - f_i\,\langle\mathbb{A}\rangle_{V_i}\right) \tag{4.98b}$$

$$\frac{1}{N^{III}} = \frac{1-f_i}{N_M} + f_i\mathbf{b}_M : (\mathbb{C}_i - \mathbb{C}_M)^{-1} : \mathbf{b}_M : \left(\mathbb{I} - \langle\mathbb{A}\rangle_{V_i}\right) \tag{4.98c}$$

The input to this homogenization step are the poroelastic properties of the porous clay laminate, $\mathbb{C}_M = \mathbb{C}^{\text{hom},II}$, $\mathbf{b}_M = \mathbf{b}^{II}$, $N_M = N^{II}$, the (quartz) inclusion volume fraction f_i, and an estimate of the volume average of the inclusion strain concentration tensor $\langle\mathbb{A}\rangle_{V_i}$. Given the matrix-inclusion morphology, such an estimate is suitably provided by the Mori-Tanaka scheme:

$$\langle\mathbb{A}\rangle_{V_M} \simeq \mathbb{A}^{est}_M = \left[(1-f_i)\mathbb{I} + f_i\left(\mathbb{I} + \mathbb{P}^M : (\mathbb{C}_i - \mathbb{C}_M)\right)^{-1}\right]^{-1} \tag{4.99}$$

where $\mathbb{P}^M$ is the so-called P-tensor that can be obtained from the matrix Green's function $G^0_{ik}(\underline{x} - \underline{x}')$ which expresses the displacement at point $\underline{x}$ in direction i in a linear

elastic solid of stiffness $\mathbb{C}^0$ ($= \mathbb{C}_M$ for the Mori-Tanaka scheme (Zaoui, 2002)) subjected to a unit force $\delta(\underline{x} - \underline{x}')$ applied in direction k at the point $\underline{x}'$:

$$\mathbb{P}^0_{ijkl} = -\left(\partial^2 \left(\int_V G^0_{ik}(\underline{x} - \underline{x}')dV\right)/\partial x_j \partial x_l\right)_{(ij)(kl)} \tag{4.100}$$

where $(ij)(kl)$ stands for the symmetrization with respect to (ij) and (kl). The expression of the P-tensor for spherical inclusions in a transversely isotropic matrix can be found in Laws (1985), and is given in the Appendix.

4.3 Calibration–Validation

The load bearing phase in shales is essentially a colloidal system of clay particles in which repulsive contact forces are in equilibrium with cohesive bonds. Like other natural composites, it behaves macroscopically as an elastic solid but with a particular microstructure. One could (and it has been!) argue(d) that continuum-based micromechanics is not the best theory suited for shales multiscale mechanical modeling. However, it may be the best currently available as far as (poro)elastic properties are concerned. Elastic homogenization theories for particulate systems are still very limited, and could not be used anyway with the continuum analysis of indentation tests.

The present model relies on two main assumptions: (1) The porous clay phase of shale is a continuous solid with pores; and (2) the pure clay stiffness is isotropic. By means of these two assumptions, we arrive at reducing the total numbers of model degrees of freedom to four: the elastic constants of the isotropic solid clay phase –bulk modulus k_s, shear modulus g_s (see (4.50)) or plane stress modulus M_s and Poisson's ratio ν_s–, the pore aspect ratio $\rho = h/D$ and the $k-$ factor. To complete the model we need to calibrate and validate the model. This will be achieved in two steps:

- For the calibration, we will only use the four results of the nano- and microindentation analysis from level I and II, and search for each shale material (porosity and inclusion volume fraction given) for the optimum set of model parameters (M_s, ν_s, ρ, k) that best fit the experimental constraints:

$$\begin{vmatrix} M^I_{1,\text{exp}} - \mu_{M_1}(M_s, \nu_s, \rho, k) \\ M^I_{3,\text{exp}} - \mu_{M_3}(M_s, \nu_s, \rho, k) \\ M^{II}_{1,\text{exp}} - M^{II}_1(M_s, \nu_s, \rho, k) \\ M^{II}_{3,\text{exp}} - M^{II}_3(M_s, \nu_s, \rho, k) \end{vmatrix} \leq \begin{matrix} \epsilon^I_1 \\ \epsilon^I_3 \\ \epsilon^{II}_1 \\ \epsilon^{II}_3 \end{matrix} \tag{4.101}$$

  where μ_{M_J} is the statistical model average (4.64), $M^{II}_J\,(J = 1, 3)$ is the model indentation modulus given by an application of the model stiffness $\mathbb{C}^{II}_{\text{hom}}$ from (4.81) in (2.44) and (2.52), and ϵ^J_j are some prescribed (absolute) error values. Ideally, $\epsilon^J_j = 0$.
- For validation purposes, we use a second experimental data set for each shale material: the dynamic elastic stiffness values determined by UPV measurements, $\mathbb{C}^{III,dyn}_{\text{exp}}$. We compare these dynamic values to the undrained model stiffness values, which are obtained from the poroelastic model properties $\mathbb{C}^{III}_{\text{hom}}, \mathbf{b}^{III}, N^{III}$ (relation

Shale #		1		2		3	
ν_s	[1]	0.4	0.48	0.4	0.48	0.315	0.415
M_s	[GPa]	32.0 – 36.7	34.2 – 38.9	36.4 – 38.0	38.5 – 41.0	36.3	38.7
ρ	[1]	0.054	0.0515	0.036	0.034	0.0155	0.0148
k	[1]	0.9		3.4		1.4	

Table 7. Summary of model calibration procedure.

(4.98)), through (see e.g. Coussy (1995)):

$$\mathbb{C}_{\text{hom}}^{III,un} = \mathbb{C}_{\text{hom}}^{III} + \mathcal{M}^{III}\mathbf{b}^{III} \otimes \mathbf{b}^{III} \tag{4.102}$$

where $\mathcal{M}^{III}$ is the overall Biot modulus:

$$\frac{1}{\mathcal{M}^{III}} = \frac{1}{N^{III}} + \frac{\phi^{III}}{K^{fl}} \tag{4.103}$$

with K^{fl} the fluid bulk modulus. The validation then reads:

$$\left|\left|\mathbb{C}_{\text{exp}}^{III,dyn} - \mathbb{C}_{\text{hom}}^{III,un}\right|\right| \leq \epsilon^{III} \tag{4.104}$$

Calibration: A Unique Clay Solid Stiffness? Table 7 provides a summary of the calibration procedure. An interesting observation is that the plane-stress modulus of the pure clay phase, $M_s = E_s/\left(1-\nu_s^2\right)$, is almost the same for all three shale materials (and even more so for the Young's modulus E_s!), which are quite different in mineralogy, burial depth, porosity, etc. It is somewhat smaller than the indentation modulus of pure mineral crystals (compare with Table 5), and clearly greater than average indentation stiffness values obtained by nanoindentation at larger scales. The main difference in between the different shale materials is the pore aspect ratio ρ and the alignment factor k. The first scales almost linearly with the clay porosity, $\rho = c\phi^I$ (where $c = 0.1745$), whereas the second appears to be unrelated to the porosity and the pore aspect ratio, as one should expect for an independent (random) model variable.

Validation: Drained and Undrained Poroelastic Properties Table 8 provides a summary of the predicted (drained) poroelastic properties at different scales for the three shale materials considered in this study. The input parameters are the values from Table 7. It is worth noting that the difference in between the Biot coefficients strongly reflects the anisotropy induced by the pore aspect ratio. Use of the level III values in (4.102) yields the undrained stiffness values to be compared with the experimental dynamic stiffness values. The comparison of experimental vs. predicted undrained stiffness properties is displayed in Figure 28. Since this data set has not been used in the calibration of the model parameters, the good agreement is a good indication of the model's capability to capture the essential poroelastic behavior of shale materials, by means of four model parameters. Two of the model parameters, the elastic constants of the pure clay phase, seem to be (almost) independent of the specific shale material, and in particular of the

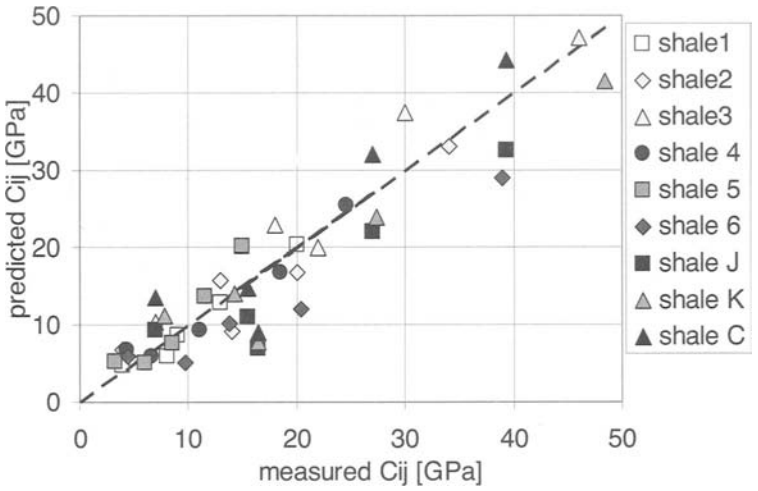

Figure 28. Predicted vs. measured C_{ij}, for the three indented shales using the calibrated input parameters, and for six other shales (J = Jurassic shale; K = Kimmeridge shale; C = Cretaceous shale).

mineralogy. A third model parameter, the pore aspect ratio, appears to be related to the porosity; most probably as a result of the burial diagenesis: the greater the burial depth, the higher the packing density of the clay particles. Such high packing densities are indicative of a more ordered structure of the shale building blocks (clay particle packages) at level 0. For the same porosity, this increases the likelihood of pore connectivity at the nanoscale, which we capture through the pore aspect ratio. The anisotropy induced by the pore aspect ratio can be considered as the base source of anisotropy of shales. A second source of anisotropy of shales stems from some preferential orientation of building blocks at larger scales (level I and II), which is captured in our model through the $k-$factor. The $k-$factor which is the only remaining (true) degree of freedom of the model, increases the base anisotropy. Motivated from nanoindentation results and SEM and ESEM images of shale materials, it is very likely that a preferred alignment of building blocks relates to silt-size inclusions that may disturb the deposition alignment of clay particles in the course of the deposition history. It should therefore be related to size and distribution of inclusions within the porous clay laminate. However, based on the multiscale investigation of three shale materials only, it is still to early to be conclusive.

Finally, Figure 28 also displays a comparison of predicted vs. experimental values for some other shale materials found in the literature. What is given for these shale materials is the porosity, the inclusion volume fraction and the clay mineralogy. The input for the predictions are the elastic constants of the pure clay phase ($M_s = 35$ GPa,

	Shale #		1		2		3	
Level 0	ν_s	[1]	0.4	0.48	0.4	0.48	0.315	0.415
	M_s	[GPa]	32.0	34.2	38.0	41.0	36.3	38.7
Level I	C_{11}	[GPa]	26.2	25.3	32.9	34.9	35.8	39.3
$\theta = 0$	C_{12}	[GPa]	11.3	13.3	14.4	18.7	11.3	17
$\varphi = 0$	C_{13}	[GPa]	2.3	2.8	3.1	4.2	1.9	3.0
	C_{33}	[GPa]	3.3	3.0	4.5	4.5	4.2	4.4
	C_{44}	[GPa]	2	1.7	2.7	2.5	3.0	2.8
	b_{11}	[1]	0.74	0.94	0.68	0.92	0.39	0.56
	b_{33}	[1]	0.95	0.99	0.93	0.98	0.78	0.78
	N	[GPa]	5.13	4.46	5.99	5.63	15.8	25.7
Level II	C_{11}	[GPa]	13.2	11.9	19.2	19.1	19.0	19.7
	C_{12}	[GPa]	4.4	4.6	6.6	7.7	5.1	6.4
	C_{13}	[GPa]	2.4	2.7	2.8	3.4	2.1	3.1
	C_{33}	[GPa]	6.8	6.2	6.6	6.5	8.4	8.7
	C_{44}	[GPa]	3.3	2.8	4.2	3.8	5.0	4.8
	b_{11}	[1]	0.87	0.94	0.82	0.96	0.58	0.67
	b_{33}	[1]	0.92	0.99	0.92	0.98	0.70	0.73
	N	[GPa]	5.13	4.46	5.99	5.63	15.8	25.7
Level III	C_{11}	[GPa]	18.1	16.5	30.2	29.8	36.6	42.8
	C_{12}	[GPa]	6.4	6.5	11.2	12.5	11.5	18.5
	C_{13}	[GPa]	3.5	3.7	4.8	5.5	8.1	15.4
	C_{33}	[GPa]	10.3	9.3	13.1	12.8	25.1	32.8
	C_{44}	[GPa]	4.8	4.8	7.3	6.8	10.5	10.4
	b_{11}	[1]	0.82	0.92	0.73	0.85	0.50	0.56
	b_{22}	[1]	0.89	0.95	0.87	0.92	0.62	0.58
	N	[GPa]	6.1	5.3	7.7	7.2	20.3	32.3

Table 8. Predicted poroelastic properties at different scales.

$\nu_s = 0.4$), and the pore aspect ratio determined from the clay matrix porosity. The $k-$factor was interpolated from the values of our three shale materials. The comparison of predicted vs. experimental dynamic measurements shows generally a good agreement for all shale materials, in which the clay phase is the load bearing phase. Some limitations of the predictive capabilities of our model relate to either high silt inclusion materials or extremely low or high porosity shale materials. Both limitations are probably due to limitations of the homogenization scheme we employ. Indeed, the schemes employed assume that the load bearing phase is the clay phase (and not the inclusion phase), so that predictions will certainly be inaccurate for high quartz inclusion shale materials. Furthermore, it is quite unlikely that the schemes can capture extremely high packing density beyond 90% (*ie.* ultra-low porosity materials) or extremely low packing density, *ie.* much below the random close-packed limit (RCP). From packing theory, it is known that such high packing densities can only be achieved by different sized solid building blocks, and would probably require considering several pore families.

5 Conclusions

We raised the question whether it were possible to break down natural porous material systems down to a scale where materials no longer change from one material to another, and to upscale ('nanoengineer') the behavior from the nanoscale to the macroscale of engineering applications. Based on a combination of indentation analysis and microporomechanics analysis of cement-based materials and shale materials, the tentatively answer is yes!

1. Level '0': At a nanoscale, most geomaterials are colloidal material systems, in which repulsive contact forces are in equilibrium with cohesive bonds. The material response at very fine scales is dominated by these surface properties, rather than by mineral properties. It is most likely that the scale of material invariant properties of natural composites is related to the predominant effect of such surface properties, which no-doubt depend on the type of mineral bonding. We come to this conclusion from the backanalysis of measured nanoindentation results of cement-based materials and shales, that seem to converge towards a single set of material properties for each class of materials: the C-S-H solid stiffness and the pure clay solid phase properties.
2. Level 'I': At a scale of tens of nanometers, most geomaterials possess characteristic packing densities, as a consequence of the material genesis, *ie.* hydration in the case of cement-based materials; deposition and burial diagenesis in the scale of shales. This packing density defines a particular solid-pore space microstructure, unique for each class of materials. In the case of cement-based materials, these are the LD– and HD–C-S-H packing; and in the case of shales, it is the shale building block, *ie.* the packages of clay particles. The material invariant properties (from level '0') and the packing mode (from level 'I') translate into a base mechanics behavior. The porosity ('one minus packing density') which manifests itself at this scale, defines much of the poromechanics behavior of natural composites at larger scales.
3. Level 'II': At a micrometer scale, the behavior of natural composites is a consequence of texture; *ie.* the LD–/HD–C-S-H volume proportions of cement-based materials, and the porous clay laminate structure of shales. Texture can explain much of the large variety of geomaterials. For instance, the lower strength of heat cured cement-based materials appears as a consequence of the conversion of LD–C-S-H into HD–C-S-H, creating a net macroporosity. In the case of shales, it is the preferred alignment of building blocks increasing the elastic anisotropy.
4. Level 'III': All things come together at the macroscale, where the textured load bearing porous material and inclusions (sand and aggregates in the case of mortar and concrete; quartz, feldspar, pyrite, etc. in the case of shales) determine the mechanical behavior of natural composites.

Our experimental microporomechanics analysis focussed primarily on the poroelastic behavior of natural composites, for which a combination of advanced experimental indentation techniques and linear microporoelasticity theory provides a unique opportunity to understand and assess nanoproperties and microstructure, as a new basis for the engin-

eering prediction of macroscopic poroelastic properties of natural composite materials. Things will still take some time regarding strength properties, requiring advances in the interpretation of strength properties from indentation tests and in non-linear microporomechanics, to ultimately arrive at identifying material invariant nanostrength properties. This is a formidable challenge!

Bibliography

P. Acker. Micromechanical analysis of creep and shrinkage mechanisms, In F.-J. Ulm, Z.P. Bažant, and F.H.Wittmann, editors, *Creep, Shrinkage and Durability Mechanics of Concrete and other quasi-brittle Materials.* Elsevier, Oxford UK, 15–25, 2001.

D.M. Barnett and J. Lothe. Line force loadings on anisotropic half-spaces and wedges. *J. Appl. Phys.*, 23:470–474, 1975.

Z.P. Bažant. Thermodynamics of interacting continua with surfaces and creep analysis of concrete structures. *Nuclear Engrg. and Design*, 20:477–505, 1972.

R.H. Bennett, N.R. O'Brien, and M.H. Hulbert. Determinants of clay and shale microfabric signatures: Processes and mechanisms. In R. Bennett, W. Bryant, M. Hulbert, editors, *Microstructure of fine grained sediments: from mud to shale*, Springer-Verlag, New York, Chapter 2, 5–32, 1991.

A. Bentur. Effect of curing temperature on the pore structure of tricalcium silicate pastes. *Journal of Colloid and Interface Science*, 74(2):549–560, 1980.

O. Bernard, F.-J. Ulm, and E. Lemarchand. A multiscale micromechanics–hydration model for the early-age elastic properties of cement-based materials. *Cem. Concr. Res.*, 33(8):1155–1173, 2003.

M.A. Biot. General theory of three dimensional consolidation. *Journal of Applied Physics*, 12:155–164, 1941.

F.M. Borodich, L.M. Keer, and C.S. Korach. Analytical study of fundamental nanoindentation test relations for indenters of non-ideal Shapes. *Nanotechnology*, 14:803–808, 2003.

F.M. Borodich and L.M. Keer. Contact problems and depth-sensing nanoindentation for frictionless and frictional boundary conditions. *Int. J. Solids Struct.*, 41: 2479–2499, 2004.

J. Brittan, M. Warner, and G. Pratt. Short Note: Anisotropic parameters of layered media in terms of composite elastic properties. *Geophysics*, 60(4):1243–1248, 1995.

X. Chateau and L. Dormieux. Micromechanics of saturated and unsaturated porous media. *Int. J. Numer. Anal. Meth, Geomech.*, 26:830–844, 2002.

Y.-T. Cheng and C.-M. Cheng. Scaling relationships in conical indentation of elastic-perfectly plastic solids. *Int. J. Solids Struct.*, 36:1231–1243, 1999.

Y.-T. Cheng and C.-M. Cheng. Scaling, dimensional analysis, and indentation measurements. *Materials Science and Engineering*, R44:91–149, 2004.

G. Constantinides, F.-J. Ulm, and K.J. van Vliet. On the use of nanoindentation for cementitious materials. *Materials and Structures* (Special issue of Concrete Science and Engineering) RILEM, 205:191–196, 2003.

G. Constantinides and F.-J. Ulm. The effect of two types of C–S–H on the elasticity of cement-based materials: Results from nanoindentation and micromechanical modeling. *Cem. Concr. Res.*, 34(1):67–80, 2004.

G. Constantinides and F.-J. Ulm. *Material invariant properties of cement-based materials: an experimental microporomechanics approach.* MIT-CEE Res. Rep. R04-03 (Ph.D.-Dissertation), Cambridge, MA, In Preparation.

O. Coussy. *Mechanics of porous continua.* J. Wiley & Sons, Chichester, UK, 1995.

O. Coussy. *Poromechanics.* J. Wiley & Sons, Chichester, UK, 2004.

A. Delafargue and F.-J. Ulm. Explicit approximations of the indentation modulus of elastically orthotropic solids for conical indenters. Int. J. Solids Struct., 41: 7351–7360, 2004.

A. Delafargue and F.-J. Ulm. *Material invariant properties of shales: nanoindentation and microporoelastic analysis.* MIT-CEE Res. Rep. R04-02 (SM-Dissertation), Cambridge, MA, 2004.

M.F. Doerner and W.D. Nix. A method for interpreting the data from depth-sensing indentation instruments. *J. Mater. Res.*, 1:601–609, 1986.

H.A. Elliot. Axial symmetric stress distributions in aelotropic hexagonal crystals: The problem of the plane and related problems. *Proc. Camb. Phil. Soc.*, 45:621–630, 1949.

A. Donev, I. Cisse, D. Sachs, E.A. Variano, F.H. Stillinger, R. Connely, S. Torquato, P.M. Chaikin. Improving the density of jammed disordered packings using ellipsoids. *Science*, 303:990–993, 2004.

L. Dormieux, A. Molinari, and D. Kondo. Micromechanical approach to the behaviour of poroelastic materials, *J. Mech. Phys. Solids*, 50:2203–2231, 2002.

L. Dormieux and E. Bourgeois. *Introduction à la micromécanique des milieux poreux.* Presses de l'Ecole nationale des ponts et chaussées, Paris, France, 2003.

A. El Omri, A. Fennan, F. Sidoroff, and A. Hihi A. Elastic-Plastic homogenization for layered composites. *European Journal of Mechanics*, A/Solids 19:585–601, 2000.

J. Eshelby. The determination of the elastic field of an ellipsoidal inclusion, and related problems. *Proceedings of the Royal Society London*, Series A, 241:376–396, 1957.

R.F. Feldman and P.J. Sereda. A new model of hydrated cement and its practical implications. *Eng. J. Can.*, 53:53–59, 1970.

F.P. Ganneau and F.-J. Ulm. *From nanohardness to strength properties of cohesive-frictional Materials — Application to shale materials.* MIT-CEE Res. Rep. R04-01 (SM-Dissertation), Cambridge, MA, 2004.

F.P. Ganneau, G. Constantinides, and F.-J. Ulm. Dual indentation technique for the assessment of strength properties of cohesive-frictional materials. *Int. J. Solids Struct.*, (in review), 2004.

E.J. Garboczi. Computational materials science of cement-based materials. *Materials and Structures*, RILEM, 26(2):191–195, 1993.

M.T. Hanson. The elastic field for conical indentation including sliding friction for transverse isotropy. *J. Appl. Mech.*, 59:S123–S130, 1992.

Z. Hashin and P.J.M. Monteiro. An inverse method to determine the elastic properties of the interphase between the aggregate and the cement paste. *Cem. Concr. Res.*, 32(8):1291–1300, 2002.

P. Helnwein. Some remarks on the compressed matrix representation of symmetric second-order and fourth-order tensors. *Comput. Methods Appl. Mech. Engrg.*, 190:2753–2770, 2001.

F.H. Heukamp and F.-J. Ulm. *Chemomechanics of calcium leaching of cement-based materials at different scales: The role of CH-dissolution and C-S-H degradation on strength and durability performance of materials and structures.* MIT-CEE Report R02-03 (D.Sc.-Dissertation), Cambridge, MA, 2002.

H.G. Hopkins, A.D. Cox, and G. Eason. Axially symmetric plastic deformation in soils. *Philosophical Transactions, Royal Society*, A264:1–45, 1961.

B. Hornby, L. Schwartz, and J. Hudson. Anisotropic effective medium modeling of the elastic properties of shales. *Geophysics*, 59(10):1570–1583, 1994.

B. Hornby. Experimental laboratory determination of the dynamic elastic properties of wet, drained shales. *Journal of Geophysical Research*, 103(B12), 29,945–29,964, 1998.

S. Igarashi, A. Bentur, and S. Mindess. Characterization of the microstructure and strength of cement paste by microhardness testing. *Advances in Cement Research*, 8(30):877–890, 1996.

H.M. Jaeger and S.R. Nagel. 'Physics of granular state. *Science*, 255(5051):1523–1531, 1992.

M. Jakobsen, J.A. Hudson, and T.A. Johansen. T-matrix approach to shale acoustics. *Geophys. J. Int.*, 154:533–558, 2003.

H.M. Jennings. A model for the microstructure of calcium silicate hydrate in cement paste. *Cem. Concr. Res.*, 30(1):101–116, 2000.

H.M. Jennings. Colloid model of C-S-H and implications to the problem of creep and shrinkage. *Materials and Structures* (Special issue of Concrete Science and Engineering) RILEM, 265:59–70, 2004.

T.A. Johansen, B.O. Ruud, and M. Jakobsen. Effect of grain scale alignment on seismic anisotropy and reflectivity of shales. *Geophysical Prospecting*, 52:133–149, 2004.

L.E.A. Jones and H.F. Wang. Ultrasonic velocities in Cretaceous shales from the Williston basin. *Geophysics*, 46:288–297, 1994.

D. Katti, S. Schmidt, D. Gosh, and K. Katti. Modeling response of pyrophyllite clay interlayer to applied stress using steered moelcular dynamics. *personal communication*, 2003.

N. Laws. A note on penny-shaped cracks in transversely isotropic materials. *Mechanics of Materials*, 4:209–212, 1985.

G.Q. Li, Y. Zhao, S.S. Pang, and Y.Q. Li. Effective Young's modulus estimation of concrete. *Cem. Concr. Res.*, 29(9):1455–1462, 1999.

D. Marion, A. Nur, H. Yin, and D. Han. Compressional velocity and porosity in sand-clay mixtures. *Geophysics*, 57(4):554–563, 1992.

M. Matar and J. Salençon. Capacité portante des fondations superficielles circulaires. *Journal de Mechanique Théorique et Appliquée*, 1(2):237—267, 1982. Available in English In *Foundation Engineering, Volume 1, Soil properties-Foundation design and construction*, Presse de l'Ecole Nationale des Ponts et Chaussées, France.

G. Mavko, T. Mukerji, and J. Dvorkin. *The Rock Physics Handbook.* Cambridge University Press, UK, 1998.

J. Mitchell. *Fundamentals of soil behavior.* J. Wiley & Sons, New York, 1993.

W.C. Oliver and G.M. Pharr. An improved technique for determining hardness and elastic modulus using load and displacement sensing indentation experiments. *J. Mater. Res.*, 7(6):1564–1583, 1992.

G.M. Pharr. Understanding nanoindentation unloading curves. *J. Mater. Res.*, 17(10):2660–2671, 2002.

T.C. Powers and T.L. Brownyard. *Studies of the physical properties of hardened portland cement paste.* PCA Bulletin 22, 1948.

M. Prasad, M. Kopycinska, U. Rabe, and W. Arnold, W. Measurement of Young's modulus of clay minerals using atomic force acoustic microscopy. *Geophysical Research Letters*, 29(8), 1172, 13-1–13-4, 2002.

L.F. Pratson, A. Stroujkova, D. Herrick, F. Boadu, and P. Malin. Predicting seismic velocity and other rock properties from clay content only. *Geophysics*, 68(6):1847–1856, 2003.

J. Salençon. *Calcul à la rupture et analyse limite.* Presses de l'Ecole nationale des ponts et chaussées, Paris, France, 1983.

C.M. Sayers. The elastic anisotrophy of shales, *Journal of Geophysical Research*, 99(B1):767–774, 1994.

C. Sayers. Stress-dependent seismic anisotropy of shales. *Geophysics*, 64(1):93–98, 1999.

N.J.A. Sloane. Kepler's conjecture confirmed. *Nature*, 395:435–436, 1998.

I. Sneddon, editor. *Application of integral transforms in the theory of elasticity.* Springer Verlag, Wien-New York, 1977.

P. Suquet, editor. *Continuum micromechanics*, CISM Courses and Lectures no. 377, 1997. Springer Verlag, Wien-New York.

J.G. Swadener and G.M. Pharr. Indentation modulus of elastically anisotropic half-spaces by cones and parabolae of revolution. *Philos. Mag.*, A81:447–466, 2001.

P.D. Tennis and H.M. Jennings. A model for two types of calcium silicate hydrate in the microstructure of portland cement pastes. *Cem. Concr. Res.*, 30(6):855–863, 2000.

J.J. Thomas and H.M. Jennings. Effect of heat treatment on the pore structure and drying shrinkage behavior of hydrated cement paste. *Journal of the American Ceramic Society*, 85(9):2293–2298, 2002.

L. Thomsen. Weak elastic anisotropy. *Geophysics*, 52(10):1954–1966, 1986.

L. Thomsen. Seismic anisotropy. *Geophysics*, 66:40–41, 2001.

I. Tsvankin. P-wave signatures and notation for transversely isotropic media: An overview. *Geophysics*, 61(2):467–483, 1996.

F.-J. Ulm and O. Coussy. *Mechanics and durability of solids. Vol. I: Solid Mechanics.* Prentice Hall, Upper Saddle River, New Jersey, 2003.

F.-J. Ulm, G. Constantinides, and F.H. Heukamp. Is concrete a poromechanics material? – A multiscale investigation of poroelastic properties, *Materials and Structures* (Special issue of Concrete Science and Engineering), 265:43–58, 2004.

T. Vanorio, M. Prasad, and A. Nur. Elastic properties of dry clay mineral aggregates, suspensions and sandstones. *Geophys. J. Int.*, 155:319–326, 2003.

K. Velez, S. Maximilien, D. Damidot, G. Fantozzi, and F. Sorrentino. Determination by nanoindentation of elastic modulus and hardness of pure constituents of portland cement clinker. *Cem. Concr. Res.*, 31(4):555–561, 2001.

B. Velde. *Origin and mineralogy of clays.* Springer-Verlag, New York, 1995.

J.J. Vlassak and W.D. Nix. Indentation modulus of elastically anisotropic half spaces. *Philos. Mag.*, A67(5):1045–1056, 1993.

J.J. Vlassak and W.D. Nix. Measuring the elastic properties of anisotropic materials by means of indentation experiments. *J. Mech. Phys. Solids*, 42(8):1223–1245, 1994.

J.J. Vlassak, M. Ciavarella, J.R. Barber, and X. Wang. The indentation modulus of elastically anisotropic materials for indenters of arbitrary shape. *J. Mech. Phys. Solids*, 51:1701–1721, 2003.

Z. Wang, H. Wang, and M.E. Cates. Effective elastic properties of solid clays. *Geophysics*, 66(2):428–440, 2001.

Z. Wang, Z. Seismic anisotropy in sedimentary rocks. Part 1: A single plug laboratory method; Part 2: Laboratory data. *Geophysics*, 67(5):1415–1422 (part I) and 67(5):1423–1440 (part II).

J.R. Willis. Herztian contact of anisotropic bodies. *J. Mech. Phys. Solids*, 14:163–176, 1966.

F.H. Wittmann. Bestimmung physikalischer Eigenschaften des Zementsteins. *Deutscher Ausschuss fuer Stahlbeton*, Heft 232:1–63, 1974, W. Ernst & Sohn, Berlin, Germany.

F.H. Wittmann. Creep and shrinkage mechanisms in concrete. In Z.P. Bažant and F.H.Wittmann, editors, *Creep & Shrinkage of Concrete*, J. Wiley & Sons, New York, 1988.

A. Zaoui. Continuum micromechanics: Survey. *Journal of Engineering Mechanics* (ASCE), 128(8):808–816, 2002.

6 Appendix: Eshelby and P tensors

6.1 Oblate spheroidal inclusion in an isotropic matrix

The non-zero components of the Eshelby tensor $\mathbb{S}$ for oblate spheroidal inclusions of aspect ratio $\rho = h/D < 1$ in a matrix of Poisson's ratio ν read:

$$S_{ijkl} = S_{jikl} = S_{ijlk}$$

$$
\begin{aligned}
S_{1111} &= \frac{3}{8\pi(1-\nu)} I_{11} + \frac{1-2\nu}{8\pi(1-\nu)} I_1 = S_{2222} \\
S_{1122} &= \frac{1}{8\pi(1-\nu)} I_{12} + \frac{1-2\nu}{8\pi(1-\nu)} I_1 = S_{2211} \\
S_{1133} &= \frac{1}{8\pi(1-\nu)} \rho^2 I_{13} + \frac{1-2\nu}{8\pi(1-\nu)} I_1 \\
S_{3311} &= \frac{1}{8\pi(1-\nu)} I_{13} + \frac{1-2\nu}{8\pi(1-\nu)} I_3 = S_{3322} \\
S_{1212} &= \frac{1}{8\pi(1-\nu)} I_{12} + \frac{1-2\nu}{16\pi(1-\nu)} (I_1 + I_2) \\
S_{2323} &= \frac{1}{16\pi(1-\nu)} (1+\rho^2) I_{13} + \frac{1-2\nu}{16\pi(1-\nu)} (I_1 + I_3)
\end{aligned}
$$

where:

$$
\begin{aligned}
I_1 &= I_2 = \frac{2\pi\rho}{(1-\rho)^{3/2}} \left\{ \cos^{-1}\rho - \rho\left(1-\rho^2\right)^{1/2} \right\}, \; I_3 = 4\pi - 2I_1 \\
I_{13} &= I_{23} = \frac{(I_1 - I_3)}{(\rho^2 - 1)}, \; 3I_{33} = 4\pi/\rho^2 - 2I_{13} \\
I_{11} &= I_{22} = I_{12} = \pi - I_{13}/4 = \pi - \frac{(I_1 - I_3)}{4(\rho^2 - 1)}
\end{aligned}
$$

Note that the Eshelby tensor in matrix notationis is not symmetric ($S_{iijj} \neq S_{jjii}$).

6.2 Spherical Inclusion in a Transversely Isotropic Matrix

The $\mathbb{P}$ tensor has the form of the stiffness tensor of a transverse isotropic material:

$P_{2222} = P_{1111}$, $P_{2211} = P_{1122}$, $P_{3311} = P_{1133}$, $P_{2323} = P_{1313}$, $P_{1212} = 1/2(P_{1111} - P_{1122})$

where:

$$
\begin{aligned}
P_{1111} &= \frac{3}{16} I_1(C_{44}, C_{33} - 2C_{44}, C_{44} - C_{33}) + \frac{1}{16} I_2(1, -1) \\
P_{1122} &= \frac{1}{16} I_1(C_{44}, C_{33} - 2C_{44}, C_{44} - C_{33}) - \frac{1}{16} I_2(1, -1) \\
P_{1133} &= \frac{1}{4} I_1(0, -C_{13} - C_{44}, C_{13} + C_{44}) \\
P_{3333} &= \frac{1}{2} I_1(0, C_{11}, C_{44} - C_{11}) \\
P_{1313} &= \frac{1}{16} I_1(C_{11}, -2(C_{11} + C_{13}), C_{11} + C_{33} + 2C_{13}) - \frac{1}{16} I_2(0, -1)
\end{aligned}
$$

and

$$I_1(l,m,n) = \frac{1}{C_{33}C_{44}} \int_{-1}^{1} \frac{\rho}{\left\{1-(1-\rho^2)\xi^2\right\}^{3/2}} \cdot \frac{l+m\xi^2+n\xi^4}{\left\{\gamma_1^2+(1-\gamma_1^2)\xi^2\right\}\left\{\gamma_2^2+(1-\gamma_2^2)\xi^2\right\}} d\xi$$

$$I_2(l,m) = \int_{-1}^{1} \frac{\rho}{\left\{1-(1-\rho^2)\xi^2\right\}^{3/2}} \cdot \frac{l+m\xi^2}{\left\{\frac{1}{2}(C_{11}-C_{12})+(C_{44}-\frac{1}{2}(C_{11}-C_{12}))\xi^2\right\}} d\xi$$

where γ_1^2, γ_2^2 are the roots of:

$$C_{33}C_{44}x^2 - (C_{11}C_{33} - 2C_{13}C_{44} - C_{13}^2)x + C_{11}C_{44} = 0$$